

# The Cosmic Shoreline Revisited: A Metric for Atmospheric Retention Informed by Hydrodynamic Escape

XUAN JI(纪璇) <sup>1</sup>, RICHARD D CHATTERJEE <sup>2</sup>, BRANDON PARK COY <sup>1</sup> AND EDWIN KITE <sup>1</sup>

<sup>1</sup>*Department of the Geophysical Sciences, University of Chicago, Chicago, IL 60637 USA*

<sup>2</sup>*Department of Atmospheric, Oceanic and Planetary Physics, University of Oxford*

## ABSTRACT

The 500-hour Rocky Worlds DDT Program, aimed at finding atmospheres on rocky exoplanets around nearby low-mass stars, emphasizes the need to constrain the “cosmic shoreline”, an semiempirical relation that separates airless worlds from worlds with atmospheres, as proposed by K. J. Zahnle & D. C. Catling (2017). Here, we determine the critical instellation required for atmospheric retention by calculating time-integrated atmospheric mass loss coupled with stellar evolution, assuming initial volatile inventories ranging from 0.01% to 1% of planetary mass. We adopt atmospheric escape rates for CO<sub>2</sub>-dominated, steam (H<sub>2</sub>O), and Earth-like (N<sub>2</sub>/O<sub>2</sub>) atmospheres, derived from previous hydrodynamic models, and we estimate energy-limited escape rates for CH<sub>4</sub> atmospheres. H<sub>2</sub>O atmospheres are completely lost, even at Earth’s insolation, whereas N<sub>2</sub>/O<sub>2</sub> atmospheres are protected by atomic line cooling. However, the cosmic shoreline for N<sub>2</sub>/O<sub>2</sub> atmospheres depends on the chosen escape model, emphasizing the need for more detailed hydrodynamic simulations. For CO<sub>2</sub> and CH<sub>4</sub> atmospheres, the critical instellation increases with both stellar and planetary mass: more massive rocky planets orbiting more massive stars are prime targets for atmospheric detection. Using these results, we propose a new metric to prioritize targets for DDT programs and list targets ranked by this metric. We also present a proof-of-concept model to show that density measurements can statistically test the existence of the cosmic shoreline, as planets with substantial atmospheres are less dense than bare rocky planets, shaping a trend in planetary mass-instellation space.

## 1. INTRODUCTION

Using 500 hours of James Webb Space Telescope (JWST) time and 240 orbits of the Hubble Space Telescope (HST), the Rocky Worlds Director’s Discretionary Time (DDT) program (S. Redfield et al. 2024) aims to find atmospheres on rocky exoplanets. An essential first step is identifying the most promising targets.

### 1.1. Cosmic Shoreline

The Rocky Worlds DDT Targets Under Consideration (TUC) <sup>1</sup> were selected using a priority metric based on the Energy-limited “Cosmic Shoreline” proposed by K. J. Zahnle & D. C. Catling (2017), an empirical boundary that separates Solar-System worlds with atmospheres from those without, which depends on relative cumulative XUV irradiation and escape velocity. The cumulative XUV irradiation was reconstructed using a scaling law with bolometric flux, following Eq. 27 in K. J. Zahnle & D. C. Catling (2017). Stellar X-ray (< 100 Å) and EUV (100–1000 Å) photons (XUV) heat the upper atmospheres of planets, directly driving expansion out of the gravitational well to space in a hydrodynamic wind (e.g., A. J. Watson et al. 1981). Young pre-main-sequence stars emit higher XUV flux, and M

<sup>1</sup> <https://outerspace.stsci.edu/pages/viewpage.action?pageId=257035126>

dwarfs, due to their slow evolution, sustain high XUV emission over much longer timescales compared to the Solar-mass stars (T. Preibisch & E. D. Feigelson 2005). As a result, the lower the mass of the stellar host the greater atmospheric escape experienced at the same bolometric instellation (F. Tian 2015a; F. Tian & S. Ida 2015). However, apart from being the physics of escape being much richer than the energy limit suggests, the “Cosmic Shoreline” does not account for the significant variations in volatile contents or compositions. While the “Cosmic Shoreline” can also be explained by impact erosion, as discussed in K. J. Zahnle & D. C. Catling (2017), this study focuses on thermal escape processes.

With a larger initial volatile content, an atmosphere can be retained longer at the same escape rate (J. E. Owen 2019). It is not known what controls initial volatile abundance on rocky planets. The volatiles of Solar System terrestrial bodies are thought to derive from chondritic material (e.g., B. Marty & L. Zimmermann 1999; A. N. Halliday 2013; M. Fischer-Gödde & T. Kleine 2017) through planetesimal accretion (e.g., J. C. Bond et al. 2010; D. C. Rubie et al. 2015) or pebble accretion (e.g., A. Johansen et al. 2023), modified by metal-silicate differentiation and by impacts at all scales (e.g., T. Lichtenberg et al. 2019, 2021b; M. M. Hirschmann et al. 2021; B. Liu et al. 2022; U. Malamud et al. 2024). During accretion, atmospheres are temporarily puffy and may boil off (J. E. Owen & Y. Wu 2016). The volatiles available to build planetary atmospheres are further influenced by magma ocean degassing, atmospheric thermal loss, etc (e.g., P. A. Sossi 2021; H. Sakuraba et al. 2021; H. Chen & S. A. Jacobson 2022; J. T. Gu et al. 2024; V. Adibekyan et al. 2024; Y. Hasegawa & M. R. Swain 2024).

These uncertainties suggest significant spread in volatile content for exoplanets.

Theories suggest that rocky planets can form with substantial water inventories (S. N. Raymond et al. 2004; E. S. Kite & L. Schaefer 2021; R. Wordsworth & L. Kreidberg 2022). The discovery of less-dense, highly irradiated volatile-rich small planets (N. Madhusudhan et al. 2023; R. Hu et al. 2024; B. Benneke et al. 2024) has motivated studies of low-density lava worlds (A. A. A. Piette et al. 2023) and carbon-rich puffy exo-Venuses (B. Peng & D. Valencia 2024). Theory suggests worlds forming between the soot line and water ice line could be C-rich (up to 1 wt% carbon) (E. A. Bergin et al. 2015, 2023), and worlds that are water-rich should be C-rich as well (B. Reynard & C. Sotin 2023). Therefore, we vary the volatile mass from Earth/Venus-like values ( $10^{-4} \times$  planetary mass) up to  $10^{-2} \times$  planetary mass and examine its impact on the cosmic shoreline.

Realistic escape rate modeling is crucial for locating the cosmic shoreline, and constraining it requires sophisticated modeling efforts. Stellar photons and stellar wind drive atmospheric escape processes (reviewed by D. C. Catling & J. F. Kasting 2017; F. Tian 2015b; G. Gronoff et al. 2020). A commonly used approximation is the energy-limited escape formulation (e.g. A. J. Watson et al. 1981; E. D. Lopez et al. 2012): the absorbed high-energy flux balances the work done to escape the gravitational potential of the planet, with an efficiency parameter ( $\epsilon$ ) accounting for uncertainties of energy-gain and loss processes.  $\epsilon$  is not well constrained and varies significantly across different atmospheric compositions. For  $H_2$ -rich atmospheres, E. D. Lopez et al. (2012) assumes  $\epsilon = 0.1_{-0.05}^{+0.1}$ , while N. V. Erkaev et al. (2013) uses  $\epsilon = 0.15 - 0.6$  in their model. Observations of Helium outflows from Mini-Neptunes suggest typical mass loss efficiencies around  $\epsilon \sim 0.2$  (A. Caldiroli et al. 2022; M. Zhang et al. 2022b,a, 2023). For Na/K-rich atmosphere, Y. Ito & M. Ikoma (2021) show that  $\epsilon \sim 10^{-4} - 10^{-3}$  due to strong atomic line cooling. Constraining  $\epsilon$  requires comprehensive hydrodynamic modeling that incorporates a full suite of physical processes, including heating efficiency, ionization, radiative cooling, and so on.

However, only a few studies have modeled exoplanetary secondary atmospheres loss at a high XUV flux. ...Models applied to the thermal escape of high molecular weight atmospheres from rocky planets have generally been of two forms: hydrodynamic thermospheres and transonic outflow. The former allow adiabatic expansion through a subsonic radial velocity profile but are limited to a Jeans escape upper boundary condition from the exobase (F. Tian 2009; A. Nakayama et al. 2022). Hydrodynamic thermospheres are thought to correctly model the start of a transition to a transonic wind (F. Tian et al. 2008), though this is not guaranteed due to non-linearity. Transonic outflow has been modelled with 1D first-principles time-stepping solutions of the hydrodynamic equations (C. P. Johnstone 2020) and with analytic approximations (R. D. Chatterjee & R. T. Pierrehumbert 2024). ... A. Nakayama et al. (2022) suggest that  $N_2/O_2$  atmospheres are more resistant to escape due to strong atomic line cooling, whereas R. D. Chatterjee & R. T. Pierrehumbert (2024) argue that even with atomic line cooling, escape rates can be high when considering an ionized exobase.

For  $CO_2$ , the model used in F. Tian (2009) and F. Tian et al. (2009) includes both neutral and ion species, accounts for heating from collisions, chemical reactions, photoelectrons, radiative line heating, etc. For cooling, the model considers adiabatic cooling, thermal conduction, and radiative line cooling, including molecular and atomic-oxygen 63  $\mu m$  cooling. The  $H_2O$ -atmosphere model used in C. P. Johnstone (2020) adds  $\sim 500$  chemical reactions, including

56 photoreactions. However, both models consider atomic line cooling only from Lyman- $\alpha$  and a specific O ( $63\ \mu\text{m}$ ) line. A. Nakayama et al. (2022) expands upon these by including chemical reactions involving internal excitation and ionization, along with a comprehensive list of atomic line cooling processes. The significant impact of atomic line cooling highlights the need for a more realistic reassessment of  $\text{CO}_2$  and  $\text{H}_2\text{O}$  atmospheres and also for  $\text{CH}_4$  atmospheres. All three models match observations of Earth’s upper atmosphere.

R. D. Chatterjee & R. T. Pierrehumbert (2024) developed an analytical framework to describe atmospheric escape, capturing the transition from hydrostatic (Jeans) to hydrodynamic escape while considering line cooling and ion-electron interactions. They find that escape rates scale linearly with XUV flux only when the flux is relatively weak and the atmosphere is weakly ionized. In contrast to earlier studies that showed a continuous increase in escape rates with increasing XUV flux, their model predicts that, at higher flux levels with the upper atmosphere strongly ionized, a collisional-radiative thermostat dominates. This thermostat, driven by strong line cooling, limits the escape rate to a constant value, independent of further increases in XUV flux. This process could enhance atmosphere retention during the saturated X-ray phase.

In summary, studies on atmospheric hydrodynamic escape of high-mean-molecular-weight atmosphere lack consensus because key physical processes—such as atomic line cooling—are omitted, as noted in later studies. Despite these uncertainties, identifying the broad trends in atmospheric retention as a function of fundamental planetary properties—i.e., the cosmic shoreline—is increasingly urgent. Refining predictions of the cosmic shoreline today can help prioritize promising targets, optimize telescope time, and maximize the scientific return of observations, ultimately accelerating progress in planetary atmosphere and habitability research.

Solar wind-driven escape from rocky planets (C. Dong et al. 2018) also play a role. While impact erosion may also strip secondary atmospheres, it is not included in this initial investigation (C. A. Sinclair et al. 2020; V. A. Krasnopolsky et al. 2004; H. E. Schlichting & S. Mukhopadhyay 2018; T. R. Denman et al. 2020; M. C. Wyatt et al. 2020). We assume volcanic outgassing or volatile replenishment from impacts are small relative to the initial volatile inventory (Q. Kral et al. 2018; E. S. Kite & M. N. Barnett 2020). We also assume a fixed semi-major axis throughout the planet’s lifespan and do not consider the planetary migration. More detailed description of our assumptions can be found in Sec. 2.

Few studies have considered the time-integrated atmospheric loss to determine the cosmic shoreline, and they either focused on specific targets (I. Ribas et al. 2016), assumed energy-limited loss or considered only hydrostatic escape (G. V. Looveren et al. 2025). Here we calculate the atmospheric mass lost over a rocky planet’s lifespan via thermal hydrodynamic escape driven by evolving stellar XUV. By assuming an initial volatile mass available for escape and modifying this initial parameter, we determine the parameter space where a planet can retain its atmosphere and then predict the cosmic shoreline.

## 1.2. Statistical Test

We suggest that in addition to resource intensive JWST searches, the existence of the cosmic shoreline can be tested through population-level statistical analysis. The shoreline defines the distribution of bare rocky planets versus those with secondary atmospheres across parameter space. Density measurements can be used to distinguish these two populations (R. Luque & E. Pallé 2022) and then evaluate whether their distribution follows the cosmic shoreline predictions.

Similar to the radius boosting effect of  $\text{H}_2/\text{He}$ -rich atmosphere of sub-Neptunes (E. D. Lopez et al. 2012; E. D. Lopez & J. J. Fortney 2014), recent studies on Puffy Venus scenarios suggest that a sufficiently thick, high-mean-molecular-weight atmosphere on lava worlds can inflate planetary radii, lowering density (A. A. A. Piette et al. 2023; B. Peng & D. Valencia 2024). By normalizing observed planetary densities against Earth-like composition models ( $\rho/\rho_\oplus$ ), planets with extended atmospheres ( $\rho/\rho_\oplus < 1$ ) can potentially be distinguished from bare rocky planets ( $\rho/\rho_\oplus \sim 1$ ).

Atmospheric height increases with temperature and decreases with gravity, making radius boosting more pronounced for smaller, highly irradiated planets (B. Peng & D. Valencia 2024). Without volatile loss, scaled density is expected to decrease with increasing instellation and increase with planetary mass. However, stronger atmospheric escape on highly irradiated, low-mass planets leads to preferential atmospheric survival on larger, less-irradiated planets. Thus, analyzing whether scaled density increases or decreases with instellation and gravity provides a potential test for the existence of the cosmic shoreline.

## 1.3. Structure

In this study, we combine a stellar evolution model, X-ray parameterization, EUV extrapolation, stellar wind estimation, and atmospheric loss rate prescriptions (Sec. 2). In Sec. 3, we present our method for estimating the cosmic shoreline. Sec. 4 presents our revised cosmic shoreline and the re-ranking of target exoplanets. We introduce the density trend test for the cosmic shoreline in Sec. 5. Finally, we discuss limitations of this work in Sec. 6.

## 2. MODEL

### 2.1. Assumptions and Initial Condition

We adopt the mass-radius relation for Earth-like composition from Fig. 1 of L. Zeng et al. (2019) (Fig. B10) to determine the planetary radius ( $R_p$ ). Here,  $R_p$  refers to the radius at the solid surface, including any potential magma layer but excluding the atmosphere. We consider atmospheric compositions that are CO<sub>2</sub>-dominated, CH<sub>4</sub>-dominated, H<sub>2</sub>O-dominated or Earth-like N<sub>2</sub>/O<sub>2</sub>.

The volatile inventory available for escape is defined as the total volatile content in the molten silicate and atmosphere after planetary formation. Our reasoning is as follows: accretional energy melts the silicate, distributing volatiles between the magma ocean and the atmosphere. The sequestration of volatiles into the solid mantle during the solidification of the primary magma ocean is small relative to their exsolution to the atmosphere (L. Elkins-Tanton 2008) (and Appendix A). Thus almost all volatiles enter the atmosphere and are available to escape. We assume no subduction and carbon cycle, focusing on planets too hot for life.

For very close-in planets, the persistent presence of surface magma allows volatiles to be exsolved into the atmosphere as atmospheric escape occurs. As atmospheric pressure decreases, the greenhouse effect weakens, leading to surface cooling and magma ocean freezing. The amount of volatiles sequestered into the mantle during freezing is expected to be even less than the estimate provided in Appendix A, since volatile concentration in the magma decreases as the atmosphere depletes. Therefore, our assumption of small sequestration is robust.

For CO<sub>2</sub>- and CH<sub>4</sub>-dominated atmospheres, we assume an initial carbon mass and calculate the carbon loss rate. For N<sub>2</sub>/O<sub>2</sub>-dominated atmospheres, we assume an initial nitrogen mass and calculate the nitrogen loss rate.

H<sub>2</sub>O is very soluble in magma and has non-negligible solubility in solid silicate (E. S. Kite & L. Schaefer 2021). As a result, the actual initial H<sub>2</sub>O concentration in the bulk silicate portion of the planet is likely higher than the values presented here.

To quantify volatile loss, we prescribe atmospheric escape loss rate by hydrodynamical models. Starting at a stellar age ranging from 1 to 100 Myr, encompassing uncertainties in when rocky planets form, we consider stellar masses ( $M_*$ ) ranging from 0.1 to 1  $M_\odot$ . The total volatile losses integrated over the age of the planet are compared to the initial volatile content to assess if the atmosphere is retained.

### 2.2. Stellar XUV evolution

All atmospheric escape mechanisms are influenced by upper atmospheres temperature. The primary source of heating in the thermospheres of planets is XUV flux. To calculate the total atmospheric loss a planet may experience, it is essential to account for the evolution of XUV flux over time. To do this, we adopt bolometric luminosity evolution models and scale the X-ray and EUV components accordingly.

#### 2.2.1. Stellar evolution

We use the bolometric luminosity and stellar radius evolution from (I. Baraffe et al. 2015) (Fig. B1). Inter-model comparisons show differences within one order of magnitude for luminosity and less than 10% for radius (E. Tognelli et al. 2018). We neglect this uncertainty as it is significantly smaller than the uncertainties introduced by the X-ray models and EUV extrapolation. We adopt an age distribution from C. Swastik et al. (2023) of small-planet(?) hosting FG (?) stars  $4.07 \pm 3.23$  (see their Figure 8). Age determination for M-dwarfs is difficult but this median agrees roughly with cool-star gyrochronology from E. Gaidos et al. (2023).

#### 2.2.2. X-ray

Stellar X-ray luminosities decrease over time as magnetic braking slows stellar rotation. For young stars, stellar X-ray emission is “saturated” with a constant ratio X-ray luminosity to bolometric luminosity,  $L_X/L_{bol}$  (e.g., O. Vilhu 1984). After this phase,  $L_X/L_{bol}$  declines exponentially with time, following a power-law decay characterized by a decline index  $L_X/L_{bol} \propto t^{-\alpha}$ . To determine  $L_X/L_{bol}(t)$ , we use two approaches. To determine  $L_X/L_{bol}(t)$ , we use two approaches. The first method (S07) extracts data from Fig. 5 of (F. Selsis et al. 2007), which is based on

RORSAT observations, assuming a constant  $L_X/L_{bol} = 10^{-3.2}$  during saturation, followed by a power-law decline with fixed index  $\alpha$ . The duration of the saturation phase varies as a function of stellar mass for  $0.1 < M_\odot < 1$ , with lower-mass stars remaining saturated for longer periods. This method provides a simplified yet widely used prescription for estimating cumulative XUV exposure across different stellar masses. The second (J12+G16) combines parameterization from (A. P. Jackson et al. 2012) for stellar masses above  $0.5 M_\odot$ , based on RORSAT, Chandra, and XMM–Newton data, and from (E. F. Guinan et al. 2016) for stellar masses below  $0.5 M_\odot$ , derived from HST and Chandra observations. Notably, in J12+G16, the saturated X-ray-to-bolometric flux ratio and decline index ( $\alpha$ ) vary with stellar mass, while they remain relatively constant in S07. Additionally, in the J12+G16 method,  $L_X/L_{bol}$  decreases with increasing stellar mass from 0.1 to  $0.5 M_\odot$ , as bolometric luminosity rises (Fig. B2). Overall, the J12+G16 method gives lower X-ray flux than S07, particularly for M dwarfs.

### 2.2.3. EUV

High-energy solar corona observations suggest that solar EUV emission remains relatively strong even as X-ray surface flux decreases, which implies that EUV may decline more slowly over time compared to X-rays (J. M. Chadney et al. 2015; G. W. King et al. 2018).

However, EUV fluxes for most stars are difficult to measure due to strong interstellar absorption in this waveband. To estimate EUV flux based on X-ray flux, we use the scaling relation from G. W. King & P. J. Wheatley (2020) (their Eq. 3 & Fig. 2):

$$\frac{L_{EUV}}{L_{bol}} = \beta \left( \frac{L_{bol}}{A} \right)^\gamma \left( \frac{L_X}{L_{bol}} \right)^{\gamma+1} \quad (1)$$

where  $A$  is the stellar surface area, calculated using the stellar radius from I. Baraffe et al. (2015). The parameters vary for different EUV bands. G. W. King et al. (2018) provide parameters for different EUV bands, with lower bounds ranging from 51 to 124 Å and the upper bound fixed at 912 Å. G. W. King & P. J. Wheatley (2020) refines these parameters, determining that for wavelengths 100–360 Å,  $\gamma_{hard} = -0.35^{+0.07}_{-0.15}$  and  $\beta_{hard} = 116$  ( $\text{erg s}^{-1} \text{cm}^{-2}$ ) $^{\gamma_{hard}}$ , while for wavelengths 360–920 Å,  $\gamma_{soft} = -0.76^{+0.16}_{-0.04}$  and  $\beta_{soft} = 3040$  ( $\text{erg s}^{-1} \text{cm}^{-2}$ ) $^{\gamma_{soft}}$ . We adopt these values as input (Fig. B3).

The total XUV flux is calculated as the sum of  $L_X$  and  $L_{EUV}$ .

Models uncertainties include: (1) different X-ray models, (2) uncertain EUV extrapolation parameters.

## 2.3. Atmospheric Escape Rate

Several studies modeled the transition to hydrodynamic escape for high mean-molecular-weight atmospheres. We adopt atmospheric loss rates as a function of XUV flux for single-species or Earth-like atmospheres from previous studies (CO<sub>2</sub>: F. Tian et al. (2009); F. Tian (2009); N<sub>2</sub>/O<sub>2</sub>: A. Nakayama et al. (2022); R. D. Chatterjee & R. T. Pierrehumbert (2024); H<sub>2</sub>O: C. P. Johnstone (2020)).

### 2.3.1. CO<sub>2</sub> atmospheres

For a CO<sub>2</sub>-dominated atmosphere, we obtain escape rates (kg/s) from Fig. 6 of F. Tian (2009) by converting the escape flux per unit surface area (kg/s/m<sup>2</sup>) (at the solid surface with radius of  $R_p$ ) into the total atmospheric loss rate. We also extract escape rates from Fig. 4 of F. Tian et al. (2009), converting the time axis into XUV flux using their assumption that  $F_{XUV} = 29.7 \cdot t^{-1.23} \text{ erg cm}^{-2} \text{s}^{-1}$ , where  $t$  is the stellar age in billions of years. We then interpolate the data to obtain a continuous function for the escape rate as a function of XUV flux. Beyond the XUV flux limits ( $F_{XUV} \gtrsim 1000 \times \text{Earth Value}$ ), we extrapolate the loss rates linearly on a logarithmic scale. F. Tian (2009) provides output for a Mars-sized planet, while F. Tian et al. (2009) presents results for planets with  $5.9 \times$ ,  $7.5 \times$ , and  $10 \times$  Earth masses. Consequently, the atmospheric escape rate for an Earth-sized planet is highly sensitive to the interpolation approach used. We illustrate various approaches in Fig. B4 and adopt the maximum and minimum values for a given XUV flux as the uncertainty range.

### 2.3.2. H<sub>2</sub>O atmospheres

For steam (H<sub>2</sub>O) atmospheres, we use the results from C. P. Johnstone (2020)’s Kompot Code. We interpolate the escape rate as a function of  $F_X + F_{EUV}$ , using data from their Table 1. Their  $F_{EUV}/F_X$  ratio is  $10 \times$  higher than ours (Fig. B3). Sensitivity tests by A. Nakayama et al. (2022) indicate that the detailed shape of the stellar UV spectrum



is unimportant. However, [G. V. Looveren et al. \(2024\)](#) show that the temperature profile of the upper atmosphere is significantly influenced by the strength of individual emission lines at 1090 Å. While we acknowledge this uncertainty, we do not incorporate it into our subsequent calculations.

### 2.3.3. N<sub>2</sub>/O<sub>2</sub> atmospheres

For an Earth-like N<sub>2</sub>/O<sub>2</sub> atmosphere, we consider two sets of results incompatible with each other. We firstly consider the results from [A. Nakayama et al. \(2022\)](#). We convert the erosion timescale from their Fig. 8 into flux by dividing the mass of a 1-bar atmosphere by the timescale. [A. Nakayama et al. \(2022\)](#) find that an N<sub>2</sub>/O<sub>2</sub> atmosphere protected by atomic line cooling. Their model includes the process in [C. P. Johnstone et al. \(2018\)](#), and a more comprehensive treatment of atomic line cooling from nitrogen (N) and oxygen (O) (ionized and neutral). They only explore the Jeans escape as their results show the atomic line cooling is strong enough to prohibit the onset of hydrodynamic escape.

We also use results from [R. D. Chatterjee & R. T. Pierrehumbert \(2024\)](#) to determine the escape rate for an N<sub>2</sub>/O<sub>2</sub> atmosphere across various planetary radii, considering forbidden atomic line cooling from nitrogen while neglecting oxygen. As described in Sec. 1, the escape rate as a function of XUV flux is divided into three regimes: 1. Weak XUV flux: escape is negligible; 2. Intermediate XUV flux: The escape rate is energy-limited and increases proportionally with XUV flux; 3. High XUV flux: The escape rate reaches a constant value due to strong atomic line cooling, becoming independent of further XUV increase.

The output from their model for four different planets with varying XUV flux is summarized in Table 1. The bottom row shows the range of XUV flux within the energy-limited regime. In this regime, the loss rate follows the scaling relation  $\dot{C}/\dot{C}_\star = F_{\text{XUV}}/F_{\text{XUV},\star}$ . For XUV flux higher than the energy-limited regime, the loss rate remains constant at its highest value within this regime. For flux below the energy-limited regime, we arbitrarily set the loss rate per surface area to a very low value of  $10^{-17}$  kg/s/m<sup>2</sup>.

To generalize the loss rate for any planetary mass, we perform a 2D interpolation for the energy-limited escape rate per surface area. Additionally, we interpolate the lower and upper XUV flux limits of the energy-limited regime separately as functions of planetary mass and apply them as bounds to the interpolated energy-limited escape rates. The final results are shown in Fig. B6.

The plateau in the loss rate at high XUV flux proposed by [R. D. Chatterjee & R. T. Pierrehumbert \(2024\)](#), predicts that if a planet starts with a volatile inventory above a certain threshold, it can retain its atmosphere regardless of its semi-major axis or the host star's XUV activity. This threshold can be estimated by multiplying the saturated loss rate by the stellar age, providing a sufficient minimum initial volatile content for atmospheric retention.

	Mars	Earth	LHS 1140c	LHS 1140b
$M_{p,\star} (M_\oplus)$	0.11	1.00	1.76	5.90
$F_{xuv,\star} (F_{xuv,\oplus})$	50	400	1000	2000
Loss Rate, $\dot{C}_\star$ (kg/s)	$3 \times 10^5$	$10^6$	$2.2 \times 10^5$	$3.4 \times 10^5$
Loss Rate per Surface Area (kg/m <sup>2</sup> /s)	$2.3 \times 10^{-9}$	$2.0 \times 10^{-9}$	$3.1 \times 10^{-10}$	$2.6 \times 10^{-10}$
Energy Limited Range of $F_{xuv} (F_{xuv,\oplus})$	5 – 500	126.5 – 1264.9	501.2 – 1995.2	1954.5 – 2046.6
	5 – 5000	126.5 – 12649.1	501.2 – 19952.6	1954.5 – 20465.8

**Table 1:** Output from [R. D. Chatterjee & R. T. Pierrehumbert \(2024\)](#) for an Earth-like N<sub>2</sub>/O<sub>2</sub> atmosphere. Note that  $F_{xuv,\star}(F_{xuv,\oplus})$  and  $\dot{C}_\star$  are baseline results. For  $F_{xuv}$  within the Energy Limited Regime, the escape rate can be calculated by  $\dot{C} = \dot{C}_\star \cdot (F_{xuv}/F_{xuv,\star})$ . The last two columns indicate the upper and lower limits of where the energy-limited regime transitions to the saturation regime, which varies by a factor of 10.

### 2.3.4. CH<sub>4</sub> atmospheres

We also consider a pure CH<sub>4</sub> atmosphere, using energy-limited loss rate estimation (e.g. [A. J. Watson et al. 1981](#); [E. D. Lopez et al. 2012](#))

$$\dot{C}_{CH_4} = \epsilon \frac{\pi F_{XUV} R_p^2 R_{xuv}}{GM_p K_{tide}} \quad (2a)$$

**Table 2:** Model input parameters used for the Monte Carlo simulations.

Parameter	Distribution / Choices	Description
$S/S_0$	$10^{U(-2,5)}$	Bolometric instellation scaled to Earth's value.
$\tau_*$	Histogram from Fig.8 in C. Swastik et al. (2023)	Stellar age distribution.
$\tau_0$	$U(1, 100) \times 10^6$ yr	Planet formation time <sup>a</sup> .
<code>xray_model</code>	{"Selsis", "Jackson"}	Choice of X-ray flux evolution model.
$\gamma_{hard}$	$U(-0.5, -0.28)$	Power-law index for EUV extrapolation (Eq. 1).
$\gamma_{soft}$	$U(-0.8, -0.6)$	Power-law index for EUV extrapolation (Eq. 1).
<code>CO2_method</code>	{"linear", "log", "GP"}	CO <sub>2</sub> escape rate interpolation method (Sec. 2.3).
$\epsilon$	$5 \times 10^{U(-2, -1)}$	Escape efficiency for energy-limited CH <sub>4</sub> escape.

<sup>a</sup> K. Righter & D. P. O'Brien (2011)

$$K_{tide} = \left(1 - \frac{3}{2\zeta} + \frac{1}{2\zeta^3}\right) \quad (2b)$$

$$\zeta = \frac{R_{Hill}}{R_{xuv}} \quad (2c)$$

where  $G$  is the gravitational constant, and  $M_p$  and  $R_p$  are the planetary mass and radius. The efficiency  $\epsilon$ , which measures the cooling effect, is not well constrained as discussed in Sec. 1. Here, we adopt a uniform distribution for the logarithm of efficiency,  $\log \epsilon \sim \mathcal{U}(-3, -1)$ .

$R_{xuv}$  represents the planetary radius where the atmosphere becomes optically thick to XUV photons. Some studies assume  $R_{xuv} = R_p$  (Y. Ito & M. Ikoma 2021; E. Stafne & J. Becker 2024), others obtain  $R_{xuv}$  by integrating the XUV absorption cross-section (R. A. Murray-Clay et al. 2009; E. D. Lopez et al. 2012; J. E. Owen & H. E. Schlichting 2024; T. Yoshida et al. 2022). The tidal enhancement factor,  $K_{tide}$ , accounts for the reduced energy required for atmospheric escape within the planet's Roche lobe (N. V. Erkaev et al. 2016). For  $R_{xuv}$  smaller than twice Hill radius,  $K_{tide} < 2$ , and variations in  $K_{tide}$  are neglected here.

Hydrodynamic simulations for heavy mean-molecular-weight atmospheres remain limited, preventing meaningful inter-model comparisons. This paper serves as an initial analysis to investigate how the cosmic shoreline can be determined using more realistic atmospheric escape rates derived from hydrodynamic simulations. We emphasize the need for more modeling work.

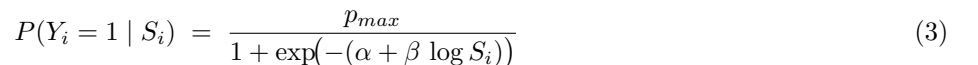
By combining the escape rate prescription with the stellar model described above, the atmospheric escape rate as a function of time for a planet orbiting a specific type of star at a given semi-major axis can be determined. Instead of providing a single value, we show a range of atmospheric escape rates for a planet with a given mass and orbital distance, incorporating all previously discussed uncertainties. The contributions of each uncertainty component are illustrated in Fig. B5, using CO<sub>2</sub> as an example. The key assumptions and the sources of uncertainties are listed in Table. B1.

For CO<sub>2</sub> and CH<sub>4</sub> atmospheres, the results apply to planets with masses ranging from 0.5 to 10  $M_\oplus$ . However, for N<sub>2</sub>/O<sub>2</sub> and H<sub>2</sub>O atmospheres, hydrodynamic simulations are only available for Earth-sized planets.

### 3. STATISTICAL METHOD

With atmospheric escape subject to many uncertainties (e.g., stellar XUV flux, interpolation methods, evolutionary timescales), we use a Monte Carlo approach to statistically estimate the "cosmic shoreline." Here, the cosmic shoreline is defined as the critical bolometric instellation ( $S^*$ ) above which a planet has less than a 90% probability of retaining its atmosphere, given an initial volatile inventory  $M_{0,v}$ . We explore how the cosmic shoreline depends on stellar mass and planetary mass, among other parameters that are harder to control (e.g., stellar age). Each uncertain parameter is drawn from an assumed probability distribution (Table 2), and for each draw, we calculate the total atmospheric loss ( $M_{loss}$ ) over the planet's lifetime. For Monte Carlo simulations at fixed  $M_p$  and  $M_*$ , we conduct  $10^4$  trials, labeling each outcome  $i$  according to whether the planet retains its atmosphere:

$$Y_i = \begin{cases} 1, & \text{if } M_{loss} \geq M_{0,v}, \\ 0, & \text{if } M_{loss} < M_{0,v}. \end{cases}$$





where  $\alpha$  and  $\beta$  are parameters fit to our Monte Carlo dataset  $\{(S_i, Y_i)\}$ . The  $p_{max}$  is a free parameter for CR24 N<sub>2</sub>/O<sub>2</sub> simulations but is forced to be 1 for other cases, which will be explained later. With  $\hat{\alpha}$  and  $\hat{\beta}$  are obtained, we solve for the critical instellation  $S^*$  that yields a chosen probability  $p_0$  of complete atmospheric loss:

$$p_0 = P(Y_i = 1 | S^*) = \frac{p_{max}}{1 + \exp(-(\hat{\alpha} + \hat{\beta} \log S^*))}, \quad (4)$$

which implies

$$\log S^* = \frac{\ln\left(\frac{p_0}{p_0 - p_{max}}\right) - \hat{\alpha}}{\hat{\beta}}. \quad (5)$$

We then obtain the critical instellation with a given loss probability  $p_0$ . We use  $p_0 = 10\%$  as the center value of the cosmic shoreline and show the range between  $p_0 = 50\%$  and  $p_0 = 1\%$ , which are corresponding to 90%, 50%, 99% probability of atmospheric retention.

From our 10,000-point Monte Carlo sample for a given planetary mass and stellar mass, we then employ a bootstrap approach to obtain a robust estimate of the critical instellation  $S^*$  for a chosen probability level  $p_0$ . Specifically, we randomly draw 5,000 data points from the original set and we refit the logistic model to this bootstrap sample to obtain parameters and compute the corresponding critical instellation,  $S^*$ . We repeat it for 10 times and then average the 10 resulting  $S^*$  values to get the critical instellation.

Fig. B8 illustrates an example logistic fit. By repeating this procedure for various stellar and planetary masses while incorporating the uncertainties in formation time, age, and other factors, we trace out the cosmic shoreline in parameter space.

#### 4. COSMIC SHORELINE

The cosmic shoreline in this study is defined as the critical bolometric instellation ( $S_{bol}^*$ ) above which a planet is highly unlikely to retain its atmosphere, given the mass of volatile available for loss. We focus on thermal escape driven by stellar XUV flux.  $S_{bol}^*$  depends on  $M_*$ , as the cumulative XUV flux varies with stellar type, and on  $M_p$ , which affects gravitational binding energy.

Additionally,  $S^*$  depends on the initial volatile mass. For CO<sub>2</sub>- and CH<sub>4</sub>-dominated atmospheres, we assume an initial C mass ranging from  $10^{-4} \times$  to  $10^{-2} \times$  planetary mass. For N<sub>2</sub>/O<sub>2</sub> atmospheres, we assume a fixed available N mass, which may not fully capture reality, as such atmospheres may not originate from the initial volatile partitioning during planet formation, but could be replenished later through a water loss redox pump mechanism which is time-dependent and flux-limited (R. D. Wordsworth 2016; L. Schaefer et al. 2016; R. D. Wordsworth et al. 2018; E. S. Kite & L. Schaefer 2021). To reflect this uncertainty, we use a dashed line to represent the cosmic shoreline for N<sub>2</sub>/O<sub>2</sub> atmospheres with a fixed initial nitrogen mass fraction. For H<sub>2</sub>O atmospheres, we consider an initial water mass between  $10^{-4}$  and  $10^{-2}$  of the planetary mass. If these volatiles remain in the atmosphere, this corresponds to surface pressures of approximately  $10^2$  and  $10^4$  bar.

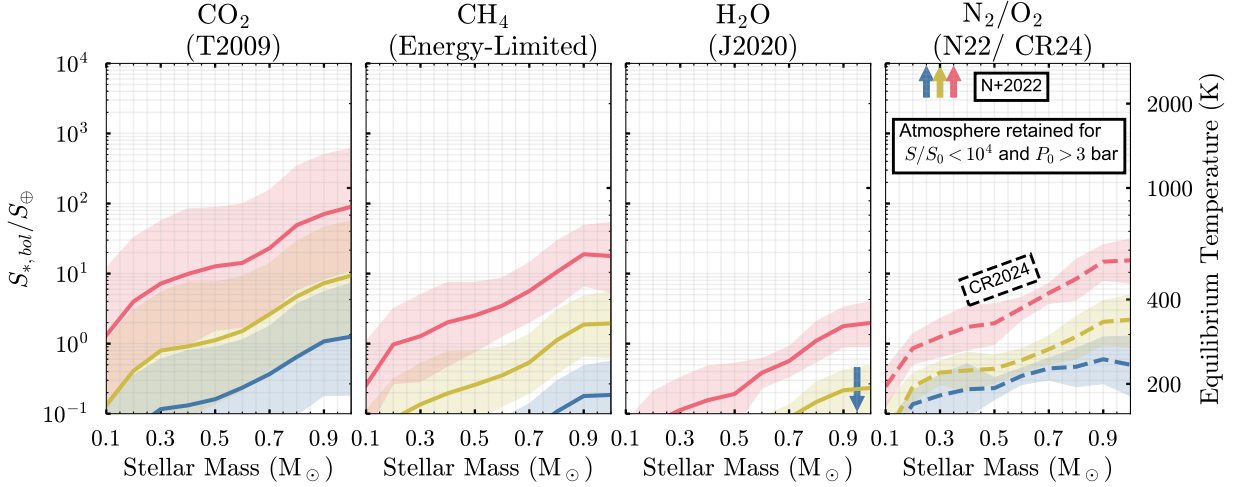
##### 4.1. Instellation vs Stellar Mass

Fig. 2 shows the cosmic shoreline for for  $1 M_\oplus$  planets as a function of stellar mass.

The blue line represents an initial volatile fraction of  $10^{-4}$  in planetary mass, which is roughly the atmosphere + silicate carbon mass ratios of Earth and Venus. Exoplanets located below this blue line could retain an atmosphere if they possessed Earth-like volatile inventories or more. The red line corresponds to an initial volatile fraction of  $10^{-2}$ , considered by us an upper limit for volatile mass. Exoplanets lying above this red line have little chance of retaining an atmosphere, even under highly volatile-rich conditions.

For CO<sub>2</sub> and CH<sub>4</sub> atmospheres, the cosmic shoreline shifts closer for lower-mass stars because their extended pre-main-sequence phase maintains high XUV flux for gigayears, leading to prolonged atmospheric loss. In contrast, for planets orbiting Sun-like stars, the escape rates become negligible after roughly 100 million years. The kink at  $0.5 M_{\odot}$  arises from a discontinuity between the E. F. Guinan et al. (2016) and A. P. Jackson et al. (2012) models.

The uncertainties overlap when the initial volatile mass differs by less than one order of magnitude. This wide range is due mostly to the uncertain CO<sub>2</sub> interpolation method for CO<sub>2</sub>-dominated atmospheres and the wide range of logarithmic heating efficiencies ( $\epsilon$ ) considered. When comparing the cosmic shorelines for CO<sub>2</sub> and CH<sub>4</sub> atmospheres, the CH<sub>4</sub> shoreline is consistently closer to the star, but the differences at higher stellar masses are smaller than at lower stellar masses. Specifically, for an initial volatile fraction of  $f_{\text{initial}} = 10^{-2}$ , the relative difference in  $\log(S/S_0)$



**Figure 2:** Cosmic shoreline for  $1 M_{\oplus}$  planets depicted as the critical bolometric instellation ( $S_{\text{bol}}^*$ )—normalized to Earth’s insolation—plotted against stellar mass for various atmospheric compositions. The right y-axis also shows the corresponding equilibrium temperature ( $T_{\text{eq}}$ ), assuming no albedo and perfect redistribution. Blue, yellow, and red lines correspond to initial volatile fractions of  $10^{-4}$ ,  $10^{-3}$ , and  $10^{-2}$  in planetary mass, respectively. The shaded regions represent a 50–99% probability range of atmospheric retention output by our model, and the solid curves represent 90% probability of atmospheric retention. For  $\text{H}_2\text{O}$  atmospheres, the blue line lies below  $1 S_{\text{bol},*}/S_{\oplus}$ . For an  $\text{N}_2/\text{O}_2$  atmosphere, predictions from A. Nakayama et al. (2022) (N+2022) suggest that all three cosmic shoreline curves exceed  $10^4 S_{\text{bol},*}/S_{\oplus}$ , indicating extreme resilience to atmospheric escape. In contrast, R. D. Chatterjee & R. T. Pierrehumbert (2024) (CR2024) predicts a much lower cosmic shoreline (the dashed lines in the lower right corner).

between  $\text{CO}_2$  and  $\text{CH}_4$  is 58.9% for a  $0.1 M_{\odot}$  star, while it decreases to 9.3% for a  $1.0 M_{\odot}$  star.

For  $\text{H}_2\text{O}$  atmospheres, the escape rate is very high. Only for  $M_* > 0.7 M_{\odot}$  can a planet at around Earth’s instellation retain its atmosphere, and only if the initial volatile mass is 1% of the planetary mass. The difference between the  $\text{CH}_4$  and  $\text{H}_2\text{O}$  can be explained by the hydrodynamic simulations of C. P. Johnstone (2020) finding a much higher effective efficiency. However, if the line cooling effect explored in (T. Yoshida et al. 2022) was included, they may be more similar. However, this is not the upper limit for planet  $\text{H}_2\text{O}$  content (S. N. Raymond et al. 2004; R. Luque & E. Pallé 2022; K. Moore et al. 2024). With 30% initial  $\text{H}_2\text{O}$ , the cosmic shoreline extends to 3 instellations for M dwarfs and up to 200 instellations for Sun-like stars. However, such high water content may be unstable due to the boil-off effect described in J. E. Owen & Y. Wu (2016). A more realistic shoreline should account for this effect, and it would be farther from the star, as indicated by the downward arrows.

Our results indicate that Earth would have lost an equivalent of 200 bars of  $\text{H}_2\text{O}$  if fully evaporated, which contradicts Earth’s history. A key missing mechanism in this study is the cold trap from condensation for habitable planets, which could protect the surface liquid water. Additionally, as water escapes from water-rich worlds and the XUV flux decreases over time,  $\text{O}_2$  may accumulate in the atmosphere (L. Schaefer et al. 2016; C. P. Johnstone et al. 2018; E. S. Kite & L. Schaefer 2021), a process not accounted for in our model.

For  $\text{N}_2/\text{O}_2$  atmospheres, predictions vary significantly between reference studies. The estimates based on A. Nakayama et al. (2022) suggest that a planet with an initial N and O mass of  $10^{-4} M_p$  can retain its atmosphere even at instellations of 10,000 times Earth’s insolation. In contrast, predictions derived from R. D. Chatterjee & R. T. Pierrehumbert (2024) indicate that atmospheric stripping could occur at much lower instellations (dashed curves in the lower right corner of Fig. 2). Resolving this discrepancy requires further work on atomic line cooling and ionization effects, to provide a more reliable constraint on  $\text{N}_2/\text{O}_2$  atmospheric escape. The CR24 results indicate that for low-mass host stars, the cosmic shorelines become independent of the initial volatile fraction. Instead, their location is primarily determined by the XUV flux threshold at which the escape regime transitions from Jeans escape to hydrodynamic escape.

#### 4.2. Comparison to Known Transiting Planets

For the following analyses, we compare our newly-derived cosmic shorelines to rocky planets from three sources:

a subset with  $R_p < 1.8R_\oplus$  or  $M_p < 10M_\oplus$  of TESS Best in Class for transmission and emission spectroscopy with JWST, as updated by Tom Evans-Soma (private communication) (E. M. R. Kempton et al. 2018; B. J. Hord et al. 2024), selected JWST targets<sup>2,3</sup>, and Rocky Worlds DDT TUCs<sup>4</sup>. To select rocky planets, we apply two criteria:  $M_p < 10M_\oplus$  and a radius below the radius gap, defined by  $\log_{10}(R_p/R_\oplus) = 0.11 \log_{10}(P/\text{days}) + 0.37$  (Eq. 4 of C. S. K. Ho & V. Van Eylen (2023)). The planetary characteristics were obtained via the NASA Exoplanet Archive. We checked for and removed mass values for planets that only have maximum or minimum reported masses. For planets without mass data and  $R_p < 1.6 R_\oplus$  [a possible dividing line between ‘rocky’ and volatile-rich low density worlds (L. A. Rogers 2015; R. Cloutier & K. Menou 2020)], properties were estimated assuming an Earth-like composition using the relation from L. Zeng et al. (2019). For planets with both radius and mass measurements, densities were calculated and scaled relative to an Earth-like composition at the same radius, defined as  $\rho^*(R_p)$ . A low density may indicate a thick atmosphere, higher volatile content, or measurement uncertainty. The dataset was processed using the NASA ExoArchive Aggregator<sup>5</sup> to obtain the TSM (transmission spectroscopy metric) and ESM (emission spectroscopy metric).

#### 4.3. Instellation vs Escape Velocity

Fig. 3 shows the cosmic shoreline for CO<sub>2</sub>- and CH<sub>4</sub>-dominated atmospheres as a function of planetary escape velocity,  $v_{esc}$ . Hydrodynamic simulations for steam and N<sub>2</sub>/O<sub>2</sub> atmospheres do not provide results for varying  $M_p$ . For each  $M_p$ , the  $v_{esc}$  is calculated assuming an Earth-like composition (L. Zeng et al. 2019).

The thick blue curve represents the traditional cosmic shoreline of K. J. Zahnle & D. C. Catling (2017) for reference. We adopt their cumulative XUV irradiation-based shoreline from their Fig. 2 and convert it to bolometric instellation using the scaling relation  $S_{bol} = F_{XUV}(L_*/L_\odot)^{0.6}$  (their Eq. 27). The red line corresponds to an initial volatile mass of  $10^{-2} \times$  planetary mass as an upper limit, while the blue line represents  $10^{-4}$  planetary mass as a lower limit.

55 Cnc e, which likely has a thick atmosphere despite its very high insolation (R. Hu et al. 2024), lies below or near the 90% cosmic shoreline for  $f_{\text{initial}} = 10^{-2}$  for both CO<sub>2</sub> and N<sub>2</sub>/O<sub>2</sub> atmospheres, while it is beyond the energy-limited estimate of the cosmic shoreline in the CH<sub>4</sub> case. Similarly, TOI-431 b, another hot rocky super-Earth with low dayside emission—implying a *tentative* atmospheric detection (C. Monaghan et al. 2025)—also aligns closely with the 90% shoreline for  $f_{\text{initial}} = 10^{-2}$ . LHS 1478 b (P. C. August et al. 2025), which has a *tentatively* detected atmosphere—suggested by a possible shallow eclipse that, if confirmed, would be consistent with an atmosphere—falls near the 90% cosmic shoreline for  $f_{\text{initial}} = 10^{-2}$  for both CO<sub>2</sub> and N<sub>2</sub>/O<sub>2</sub> atmospheres.

For the TRAPPIST-1 system, both TRAPPIST-1 b and c lie inside the  $f_{\text{initial}} = 10^{-2}$  but outside the  $f_{\text{initial}} = 10^{-4}$  boundary for all three compositions. The non-detection of atmospheres for these planets may suggest that their initial volatile content is likely lower than  $f_{\text{initial}} = 0.01$ .

Whereas Earth and Venus are on the airless side of model runs, this is not necessarily a prediction of airlessness, as there is also the limiting factor of supply of volatiles on escape rate, which may be especially acute in the star’s early phase of saturation in ionising luminosity.

The overall pattern of scaled density reveals that blue and green dots, representing less-dense planets, tend to cluster farther to the cosmic shoreline compared to red and orange dots, suggesting that planets with lower scaled densities are less susceptible to atmospheric loss. Further implications of this trend will be explored in detail in Sec. 5.

The cosmic shoreline moves to lower instellation for low  $M_*$ , and most TUCs orbit M-dwarfs. Many of these planets fall within the red shaded region, indicating a potential to detect atmospheres around them if their initial volatile content exceeds 1 wt% of their planetary mass. In contrast, planets in the gray zone have a probability of less than 0.5 of retaining an atmosphere, even with an initial volatile content of 1 wt%. These planets are therefore unlikely to be suitable candidates for atmospheric retention.

The cosmic shorelines for both CO<sub>2</sub> and CH<sub>4</sub> atmospheres shift inward with increasing planetary escape velocity, indicating that more massive planets are better at retaining their atmospheres against hydrodynamic escape. For CH<sub>4</sub>, the energy-limited escape rate ( $\text{kg} \cdot \text{s}^{-1}$ ) does not change much with planetary mass (see Fig. 1), so the increase in the critical instellation is purely due to the greater volatile reservoir available for more massive planets, as the volatile-to-total mass ratio is fixed. In contrast, for CO<sub>2</sub>, the critical instellation rises a lot for more massive planets. This stronger gravity requires higher temperatures for efficient thermal escape to occur, which continues until adiabatic

<sup>2</sup> <https://www.stsci.edu/~nnikolov/TrExoLiSTS/JWST/trexolists.html>

<sup>3</sup> <https://www.stsci.edu/~nnikolov/DIExoLiSTS/diexolists.html>

<sup>4</sup> <https://outerspace.stsci.edu/pages/viewpage.action?pageId=257035126>

<sup>5</sup> <https://github.com/lkreibberg/TSM>

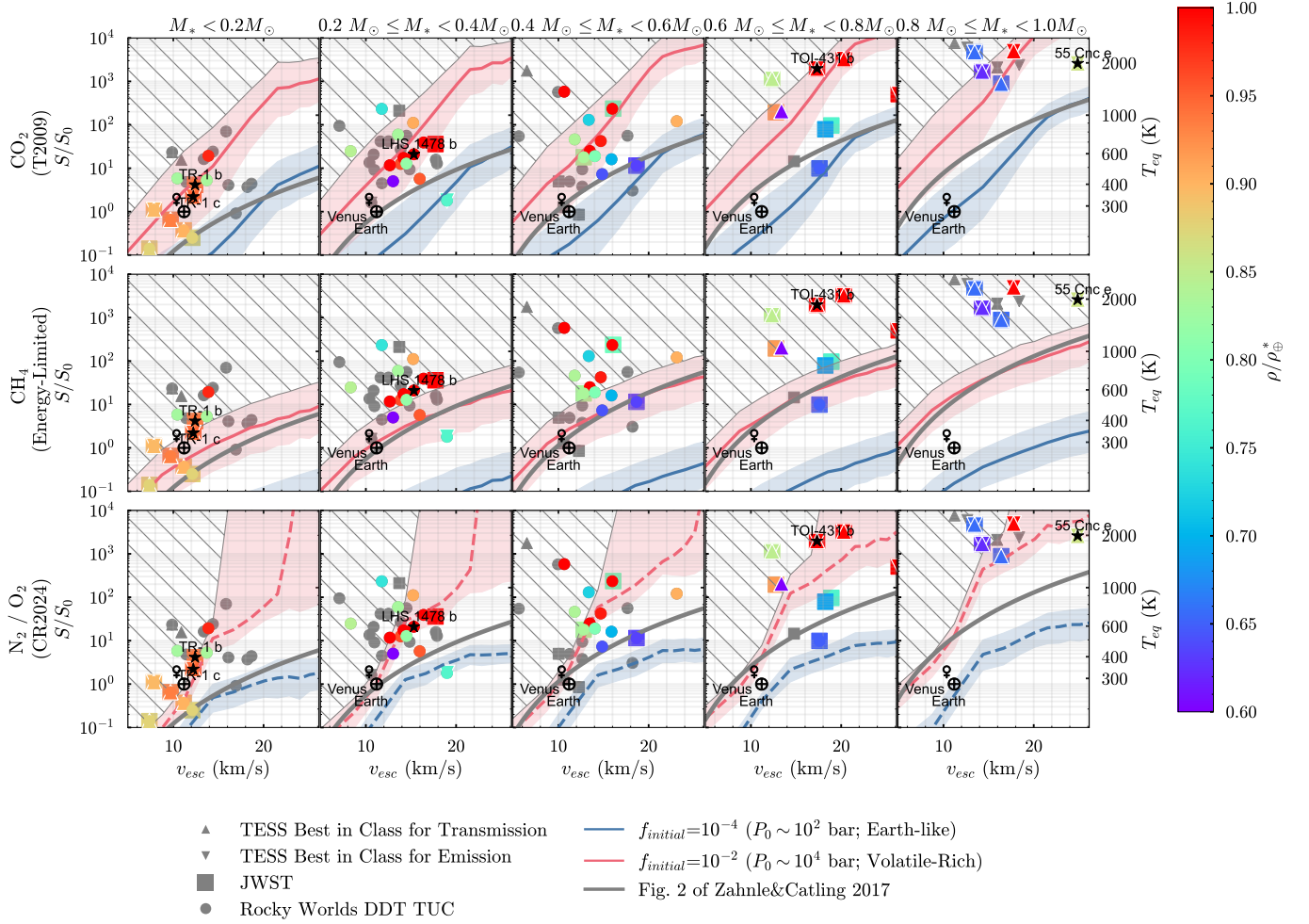


**Figure 3:** Cosmic shoreline displayed as the critical bolometric instellation ( $S_{bol}^*$ )—normalized to Earth’s insolation—versus planetary escape velocity. The right y-axis also shows the corresponding equilibrium temperature ( $T_{eq}$ ), assuming no albedo and perfect redistribution. The top row show results for  $\text{CO}_2$ -dominated atmosphere, the medium row shows  $\text{CH}_4$ -dominated atmosphere, and the bottom row show  $\text{N}_2/\text{O}_2$  atmosphere. Each column corresponds to a specific range of host stellar masses. Blue and red lines indicate initial volatile fractions of  $10^{-4}$  and  $10^{-2}$  of the planetary mass, respectively. The shaded regions in blue and red represent a 50–99% probability of atmosphere retention. The dots mark exoplanet targets from four different samples. For planets with both radius and mass measurements, the density—scaled to that of a planet with Earth-like composition ( $\rho_\oplus(M_p)$ )—is color-coded. Lower densities may suggest thicker atmospheres or higher volatile content. For comparison, the thick blue line represents the cosmic shoreline defined by XUV flux from Fig. 2 of K. J. Zahnle & D. C. Catling (2017), converted into bolometric flux using the relation  $S = F_{\text{XUV}}(L_*/L_\odot)^{0.6}$  (their Eq. 27). The hatched region above the 50% red line represents conditions where planets are unlikely to retain an atmospheres. Venus, Earth, TRAPPIST-1 b & c, 55 Cnc e, LHS 1478 b, and TOI-431 b are plotted for reference.

cooling effects become dominant and suppress further escape. An example is 55 Cnc e, an 8 Earth-mass planet orbiting a K star. It lies below the red cosmic shoreline set by a 1 wt% volatile mass fraction, meaning the detection of a secondary atmosphere at such high instellation is not surprising if 55 Cnc e formed volatile-rich (B.-O. Demory et al. 2016; R. Hu et al. 2024; J. A. Patel et al. 2024).

The slope of the cosmic shoreline determined using energy-limited estimates closely resembles the traditional cosmic shoreline. However, the shoreline derived from hydrodynamic simulations for  $\text{CO}_2$  atmospheres shifts closer to the star for more massive planets.

The shape of the cosmic shoreline for  $\text{N}_2/\text{O}_2$  atmospheres varies with initial volatile content. When the initial

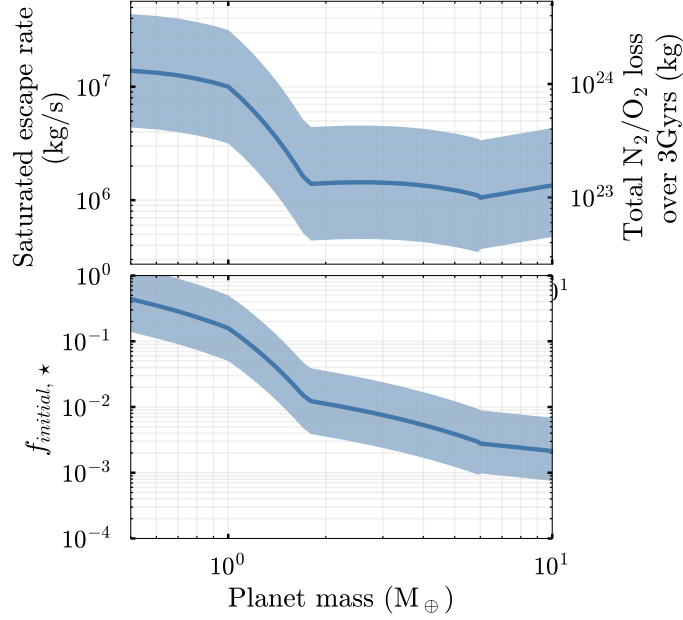


**Figure 4:** Upper Panel: Saturated escape rate of  $\text{N}_2/\text{O}_2$  atmospheres as a function of planetary mass, based on R. D. Chatterjee & R. T. Pierrehumbert (2024). The left y-axis represents the total atmospheric loss over 3 Gyrs, which also defines the critical initial volatile content required for atmospheric retention over this timescale—planets with an initial volatile mass above this threshold can retain their atmosphere regardless of historical XUV flux intensity. The critical initial volatile fraction (relative to planetary mass) ( $f_{\text{initial},*}$ ) sufficient to sustain an atmosphere over 3 Gyrs, independent of historical XUV flux intensity, shown as a function of planetary mass. The shaded region represents uncertainties arising from two limits of the energy-limited regime (see Table. 1).

nitrogen and oxygen mass is  $10^{-4}M_p$ , the shape of cosmic shoreline largely follows the traditional energy-limited estimate from K. J. Zahnle & D. C. Catling (2017), shifting to higher instellations with increasing stellar mass.

For the upper-limit case with  $f_{\text{initial}} = 10^{-2}$ , the cosmic shoreline initially follows the energy-limited trend for lower-mass planets but rises steeply around Earth mass, with larger uncertainties. This is because the saturated escape regime limits total volatile loss, and more massive planets are able to retain their atmosphere as their initial volatile mass exceeds this threshold.

For low-mass stars with extended X-ray saturation phases, atmospheric loss depends on stellar age instead of XUV flux. Since we sample planets with a wide range of ages, those experiencing the same XUV flux may either retain or lose their atmosphere, leading to a broad logistic probability-determined cosmic shoreline. In contrast, for more massive stars with shorter saturation phases, the total loss is less age-dependent, reducing uncertainties.

According to R. D. Chatterjee & R. T. Pierrehumbert (2024), atomic line cooling strongly suppresses escape rates at high XUV flux, making the escape rate nearly constant and independent of XUV flux (see Fig. 1). This saturation effect limits the total atmospheric loss, regardless of the historical XUV exposure. The maximum atmospheric loss can be estimated by multiplying the saturated escape rate by the planet’s age. In Fig. 4, we show the saturated atmospheric escape rate and the maximum atmospheric loss over 3 Gyrs (upper panel) along with the corresponding critical initial volatile fraction ( $f_{\text{initial},*}$ ) (lower panel), which represents the minimum volatile inventory required to make atmospheric retention over this timescale independent of historical XUV flux. As shown in Fig. 4, for planets with  $M_p > 1.5M_{\oplus}$ ,  $f_{\text{initial},*} < 10^{-2}$ , confirming that the upper-limit case can always retain its atmosphere, even at extremely close orbital distances.

#### 4.4. Best Planets for Atmospheric Retention

The initial priority metric for DDT TUC targets was based on the tangential distance between the star and the traditional cosmic shoreline. Given the changing curvature of the cosmic shoreline, we propose refining the priority metric to measure the vertical distance—specifically, the difference in the base-10 logarithm of instellation between the planet and the cosmic shoreline for a 1 wt% volatile mass fraction at a given planetary mass. The updated



priority scores are presented in Table 3, where the first three columns list scores separately for CO<sub>2</sub>, CH<sub>4</sub>, and N<sub>2</sub>/O<sub>2</sub> atmospheres, sorted in ascending order by CO<sub>2</sub> priority score.

We highlight planets with high observability metrics that are likely “rocky”; those with a radius below  $1.6 R_{\oplus}$  or a normalized density above  $0.8 \rho_{\oplus}^*$ . We consider planets with an emission spectroscopy metric (ESM) above that of TRAPPIST-1 c’s (ESM=1.7, amenable to atmospheric reconnaissance with MIRI F1500W) or a transmission spectroscopy metric (TSM) greater than 10 (the threshold for atmospheric characterization suggested by E. M. R. Kempton et al. 2018).

Eclipse observations are particularly powerful for identifying candidate atmosphere on rocky planets (e.g., M. Mansfield et al. 2019; D. D. B. Koll et al. 2019; J. Ih et al. 2023) while providing useful geological information for planets without atmospheres (e.g., B. P. Coy et al. 2024; K. Paragas et al. 2025).

**Table 3.** Atmospheric Retention Targets Ranked by Priority Metric for CO<sub>2</sub>-Dominated Atmospheres

Planet	Priority Metric			$R_p$ ( $R_{\oplus}$ )	$M_p$ ( $M_{\oplus}$ )	$v_{esc}$ (km/s)	$\rho^6$ ( $\rho_{\oplus}^*$ )	$M_*$ ( $M_{\odot}$ )	$T_{eq}$ (K)	K-mag	$(R_p/R_s)^2$ (ppm)	ESM <sup>7</sup>	TSM <sup>8</sup>
	[CO <sub>2</sub> ]	[CH <sub>4</sub> ]	[N <sub>2</sub> /O <sub>2</sub> ]										
TOI-1452 b	-2.46	-0.65	-1.60	1.67	4.82	19.0	0.77	0.25	322	9.7	2997	0.53	38.0
TOI-198 b	-2.38	-0.68	-1.67	1.44	3.82	18.2	1 <sup>†</sup>	0.47	368	7.9	900	0.63	5.2
TOI-406 c	-1.95	0.04	-1.37	1.32	2.08	14.0	0.80	0.41	580	8.8	871	2.52	8.3
TOI-776 b	-1.86	-0.12	-1.16	1.80	5.00	18.7	0.63	0.54	511	7.6	898	2.67	49.8
K2-415 b	-1.67	0.20	-0.80	1.01	7.50	30.4	4.77	0.16	411	9.9	2165	1.19	1.9
TOI-260 b	-1.63	-0.08	-0.91	1.71	4.23	17.6	0.65	0.62	493	6.5	660	2.54	66.1
TOI-1634 b	-1.59	0.60	-1.48	1.77	7.57	23.1	0.90	0.45	922	8.6	1305	13.98	53.6
TOI-1467 b	-1.56	0.11	-0.85	1.92	9.00	24.2	0.80	0.49	573	8.6	1290	3.49	31.5
LP 890-9 c	-1.45	-0.23	-0.32	1.37	25.30	48.1	4.49	0.12	271	11.3	6135	0.22	0.7
TOI-700 d	-1.39	-0.66	-0.51	1.07	1.29	12.3	1 <sup>†</sup>	0.41	266	8.6	549	0.05	3.5
LTT 1445 A b	-1.18	0.09	-0.21	1.34	2.73	16.0	0.95	0.26	429	6.5	2070	6.07	34.3
TRAPPIST-1 g	-1.17	-0.44	-0.17	1.13	1.32	12.1	0.88	0.09	196	10.3	7440	0.04	15.1
TOI-1680 b	-1.10	0.34	0.02	1.47	4.08	18.7	1 <sup>†</sup>	0.18	402	10.8	4096	1.31	6.3
TOI-244 b	-1.03	0.04	-0.31	1.52	2.68	14.9	0.64	0.43	456	8.0	1050	1.93	70.0
TOI-178 c	-1.00	0.79	-0.33	1.67	4.77	18.9	0.76	0.65	873	8.7	554	3.88	33.9
TOI-237 b	-0.97	0.33	0.17	1.44	3.82	18.2	1 <sup>†</sup>	0.18	385	10.9	3952	1.01	5.8
HD 260655 c	-0.95	0.29	-0.23	1.53	3.09	15.9	0.70	0.44	556	5.9	1020	8.81	195.5
TOI-836 b	-0.91	0.75	-0.20	1.70	4.53	18.2	0.69	0.68	828	6.8	544	7.39	77.4
TOI-700 e	-0.88	-0.29	0.14	0.95	0.85	10.6	1 <sup>†</sup>	0.41	295	8.6	433	0.07	4.1
TOI-771 b	-0.84	0.44	0.13	1.42	3.63	17.9	1 <sup>†</sup>	0.22	526	9.7	2951	4.58	10.9
TOI-1468 b	-0.80	0.74	0.17	1.28	3.21	17.7	1.24	0.34	680	8.5	1191	6.25	9.9
TRAPPIST-1 f	-0.79	-0.16	0.17	1.04	1.04	11.2	0.90	0.09	216	10.3	6374	0.09	16.8
Kepler-167 d	-0.71	0.34	0.01	1.24	2.16	14.8	1 <sup>†</sup>	0.78	542	11.8	229	0.09	0.5
TOI-4559 b	-0.67	0.56	0.28	1.42	3.56	17.7	1 <sup>†</sup>	0.39	553	8.6	1229	3.19	7.9
55 Cnc e	-0.66	1.55	-0.59	1.90	9.38	24.9	0.86	0.91	1958	4.0	342	71.22	226.2
K2-239 d	-0.66	0.02	0.26	1.10	1.41	12.6	1 <sup>†</sup>	0.40	399	10.0	785	0.33	3.9
LP 890-9 b	-0.64	0.47	0.49	1.32	13.20	35.4	3.24	0.12	395	11.3	5721	1.56	1.8
GJ 486 b	-0.54	0.86	0.46	1.29	2.77	16.4	1.09	0.31	695	6.4	1364	21.71	36.3
TRAPPIST-1 h	-0.50	0.03	0.61	0.76	0.33	7.4	0.88	0.09	170	10.3	3327	0.00	15.9
L 98-59 d	-0.44	0.39	0.51	1.58	2.14	13.0	0.48	0.31	415	7.1	2183	4.19	260.4
Gliese 12 b	-0.44	0.23	0.72	0.90	10.00	37.3	8.42	0.24	312	7.8	934	0.34	1.1

<sup>6</sup> the density scaled to that of a planet with Earth-like composition

<sup>7</sup> Emission spectroscopy metric from E. M. R. Kempton et al. (2018)

<sup>8</sup> Transmission spectroscopy metric from E. M. R. Kempton et al. (2018)

TOI-1693 b	-0.44	0.82	0.28	1.41	3.51	17.7	1 <sup>†</sup>	0.49	764	8.3	790	6.06	7.9
TOI-2096 b	-0.43	0.53	0.44	1.24	2.19	14.8	1 <sup>†</sup>	0.23	486	11.0	2455	1.48	6.5
LHS 1478 b	-0.42	0.73	0.49	1.24	2.33	15.3	1.05	0.24	595	8.8	2074	6.76	17.8
WASP-47 e	-0.38	1.83	-0.31	1.83	9.00	24.8	0.93	1.06	2325	10.2	209	3.04	11.2
L 98-59 c	-0.35	0.63	0.51	1.34	2.25	14.5	0.82	0.31	525	7.1	1570	7.40	28.8
Kepler-446 b	-0.32	0.98	0.82	1.15	1.64	13.4	1 <sup>†</sup>	0.19	557	12.8	2285	0.93	3.9
TRAPPIST-1 e	-0.31	0.27	0.78	0.92	0.69	9.7	0.93	0.09	249	10.3	4940	0.19	19.9
K2-239 c	-0.29	0.30	0.72	1.00	1.01	11.2	1 <sup>†</sup>	0.40	427	10.0	649	0.36	4.3
GJ 357 b	-0.27	0.67	0.62	1.20	1.84	13.9	0.96	0.34	523	6.5	1047	6.16	27.6
K2-239 b	-0.26	0.42	0.65	1.10	1.41	12.6	1 <sup>†</sup>	0.40	502	10.0	785	0.82	4.9
TRAPPIST-1 c	-0.25	0.50	0.76	1.10	1.31	12.2	0.95	0.09	338	10.3	7024	1.71	24.2
HD 260655 b	-0.22	0.81	0.50	1.24	2.14	14.7	0.99	0.44	708	5.9	668	11.78	28.7
LHS 1140 c	-0.21	0.71	0.87	1.27	1.91	13.7	0.83	0.18	421	8.8	2810	2.90	21.3
TOI-700 b	-0.19	0.38	0.86	0.91	0.73	10.0	1 <sup>†</sup>	0.41	415	8.6	398	0.36	5.9
TOI-270 b	-0.18	0.61	0.66	1.21	1.58	12.8	0.83	0.40	581	8.3	847	3.24	12.9
LHS 1815 b	-0.18	0.70	0.61	1.09	1.58	13.5	1.14	0.50	617	8.0	398	1.88	6.6
K2-129 b	-0.17	0.52	0.88	1.04	1.15	11.8	1 <sup>†</sup>	0.36	404	8.9	701	0.52	6.7
LTT 1445 A c	-0.04	0.78	0.92	1.07	1.37	12.7	1.06	0.26	514	6.5	1320	7.68	41.7
TRAPPIST-1 b	-0.02	0.75	0.99	1.12	1.37	12.4	0.94	0.09	396	10.3	7269	3.78	28.4
TOI-1685 b	0.17	1.44	0.89	1.47	3.03	16.1	0.79	0.45	1089	8.8	856	11.68	12.2
Wolf 327 b	0.19	1.45	0.91	1.24	2.53	16.0	1.13	0.41	1087	8.4	769	12.27	12.7
K2-141 b	0.19	2.24	0.71	1.51	4.97	20.3	1.06	0.71	2100	8.4	414	14.97	60.4
TOI-6086 b	0.21	1.08	1.14	1.18	1.81	13.9	1 <sup>†</sup>	0.25	632	10.0	1731	4.15	11.1
Kepler-1107 b	0.22	1.94	0.86	1.45	3.92	18.4	1 <sup>†</sup>	0.86	1943	12.2	290	1.44	1.4
LHS 1678 d	0.27	0.94	1.40	0.98	0.94	11.0	1 <sup>†</sup>	0.34	482	8.3	743	1.44	13.3
GJ 3929 b	0.27	1.02	1.27	1.09	1.75	14.2	1.23	0.31	566	7.9	975	4.12	14.2
TRAPPIST-1 d	0.28	0.82	1.42	0.79	0.39	7.8	0.90	0.09	285	10.3	3624	0.34	25.5
TOI-4527.01	0.31	1.74	1.03	0.91	0.72	10.0	1 <sup>†</sup>	0.48	1359	7.0	289	12.75	30.3
LTT 3780 b	0.33	1.47	1.24	1.32	2.46	15.2	0.90	0.38	902	8.2	1022	13.07	17.7
GJ 1132 b	0.34	1.27	1.43	1.19	1.84	13.9	0.98	0.19	582	8.3	2467	9.82	29.9
TOI-1416 b	0.35	1.68	0.93	1.62	3.48	16.4	0.65	0.80	1515	7.7	353	9.70	83.1
GJ 3473 b	0.38	1.33	1.26	1.26	1.86	13.6	0.83	0.36	771	8.8	1036	6.87	14.6
TOI-1450 A b	0.44	1.11	1.36	1.13	1.26	11.8	0.84	0.48	722	7.6	466	4.50	13.9
LP 791-18 b	0.50	1.40	1.57	1.21	2.00	14.4	1 <sup>†</sup>	0.14	616	10.6	3811	6.95	15.7
LP 791-18 d	0.52	1.13	1.54	1.03	0.90	10.4	0.83	0.14	431	10.6	2763	1.44	15.1
LHS 1678 c	0.52	1.19	1.71	0.94	1.40	13.6	1.59	0.34	532	8.3	683	1.88	8.7
GJ 806 b	0.56	1.42	1.36	1.33	1.90	13.4	0.72	0.41	938	6.5	886	24.40	45.1
LHS 475 b	0.60	1.28	1.72	0.97	0.92	10.9	1 <sup>†</sup>	0.27	593	7.7	950	5.24	26.3
LHS 3844 b	0.64	1.72	1.76	1.30	2.61	15.8	1 <sup>†</sup>	0.15	804	9.1	3953	28.62	35.1
TOI-5720 b	0.65	1.41	1.66	1.09	4.30	22.2	2.54	0.38	706	9.3	692	2.97	2.6
TOI-1444 b	0.72	2.31	1.34	1.42	3.58	17.8	1.00	0.95	2130	9.1	204	4.48	5.0
TOI-431 b	0.75	2.24	1.46	1.28	3.07	17.3	1.20	0.78	1862	6.7	258	15.68	15.7
TOI-544 b	0.76	1.62	1.56	2.02	2.89	13.4	0.29	0.63	999	7.8	890	13.00	178.1
K2-91 b	0.76	1.53	1.76	1.22	2.05	14.5	1 <sup>†</sup>	0.38	760	10.6	1222	3.32	6.5
TOI-6008 b	0.81	1.50	1.87	1.03	4.00	22.0	2.84	0.23	705	9.5	1548	6.55	5.2
TOI-1860 b	0.83	2.10	1.41	1.31	2.66	16.0	1 <sup>†</sup>	0.99	1885	6.8	163	7.98	12.5
TOI-178 b	0.87	1.65	1.71	1.15	1.50	12.8	0.92	0.65	1040	8.7	264	2.71	6.4
SPECULOOS-3 b	0.88	1.49	1.86	0.98	0.93	10.9	1 <sup>†</sup>	0.10	551	10.5	5571	8.13	36.7
TOI-1442 b	0.96	1.90	1.85	1.17	1.76	13.7	1 <sup>†</sup>	0.29	1072	10.1	1197	9.40	12.6
TOI-1807 b	1.13	2.14	1.70	1.50	2.44	14.3	0.62	0.80	1694	7.6	335	11.68	18.8

TOI-540 b	1.22	1.81	2.29	0.90	0.70	9.9	1 <sup>†</sup>	0.16	611	8.9	1898	6.75	37.7
L 98-59 b	1.22	1.82	2.43	0.85	0.47	8.3	0.84	0.31	619	7.1	632	5.05	41.5
GJ 1252 b	1.39	2.15	2.39	1.19	1.32	11.8	0.74	0.38	1086	7.9	786	16.42	31.8
TOI-500 b	1.72	2.46	2.60	1.17	1.42	12.3	0.85	0.74	1614	7.7	247	8.44	15.5
TOI-561 b	1.77	2.68	2.41	1.40	2.02	13.5	0.66	0.81	2302	8.4	232	7.97	14.0
GJ 367 b	1.77	2.36	2.78	0.70	0.63	10.6	1.96	0.46	1363	5.8	194	16.24	31.2
GJ 238 b	1.82	2.33	2.78	0.57	0.14	5.6	1 <sup>†</sup>	0.42	758	7.0	146	2.00	26.1
K2-183 b	2.05	2.88	2.79	1.10	1.41	12.6	1 <sup>†</sup>	0.94	2451	11.0	134	1.46	2.9
LHS 1678 b	2.07	2.63	3.17	0.69	0.35	8.0	1.24	0.34	866	8.3	362	3.90	21.8
K2-157 b	2.47	3.14	3.35	1.00	1.01	11.2	1 <sup>†</sup>	0.94	2601	11.0	109	1.31	3.3
K2-223 b	2.54	3.12	3.60	0.89	0.67	9.7	1 <sup>†</sup>	1.06	2271	9.8	67	1.03	4.2

**Table 3.** Planets located below the cosmic shorelines for  $f_{\text{initial}} = 10^{-4}$  are marked with an asterisk (\*). The scores for each atmospheric composition represent the difference in the base-10 logarithm of instellation between the planet and the cosmic shoreline for a 1 wt% volatile mass fraction at a given planetary mass. <sup>†</sup> These planets lack a measured mass value and we assume an Earth-like composition for these calculations.

## 5. TREND OF RATIO DENSITY

The transit radius  $R_{\text{transit}}$  corresponds to the altitude where the atmosphere becomes sufficiently opaque in a slant viewing geometry, under which  $\sim 1/e$  starlight will be blocked. If opaque clouds or hazes are present, transit radius then corresponds to the altitude of the cloud tops (E. D. Lopez et al. 2012; P. Gao et al. 2020; P. Gao & D. Powell 2021).

Since planetary mass ( $M_p$ ) can be measured through radial velocity observations, planet density can be calculated using the transit radius:  $\rho = M_p / (4/3\pi R_{\text{transit}}^3)$ . Because the transit radius includes the atmospheric contribution, the measured density ( $\rho$ ) can be lower than the density of the solid portion of the planet alone. By comparing the observed density with theoretical density estimates for rocky planets, we can distinguish planets with substantial atmospheres from bare rocky worlds (L. A. Rogers 2015; D. Jontof-Hutter 2019; R. Luque & E. Pallé 2022).

As the cosmic shoreline serves as a boundary separating bare rocky planets from those with significant atmospheres in planetary-mass–instellation space, we expect statistical trends in the observed densities of exoplanets. Specifically, density should increase with instellation and decrease with planetary mass because planets that experience weaker XUV flux and have higher gravity are more likely to retain their atmospheres and have lower densities. This trend provides an observational test for the cosmic shoreline hypothesis.

### 5.1. Vertical Thermal Structure

To see how atmosphere boosts planetary radius, we construct a one-dimensional vertical structure model that considers the thermal structure of the atmosphere and the underlying magma ocean, if present. Using this, we estimate the transit radius of a planet with a given volatile content by accounting for radiative and convective layers of atmosphere, volatile partitioning between the atmosphere and magma, and the effect of hydrostatic equilibrium on atmospheric extent. We then derive the density ratio to an Earth-like composition and perform statistical analysis to investigate how the cosmic shoreline influences the trend of the ratio density.

This model, with several simplifying assumptions, is intended to demonstrate the concept rather than provide precise predictions. For this study, we focus on CO<sub>2</sub> atmospheres as a representative case, given that the Mid-Infrared Instrument (MIRI) on JWST is most sensitive to CO<sub>2</sub> detection at 15  $\mu\text{m}$ , and given the importance of CO<sub>2</sub> for solar-system rocky planets.

We first consider a two-layer atmospheric structure, as illustrated in panel (1) of Fig. 5: 1. a radiative upper atmosphere, where the temperature is isothermal above the radiative-convective boundary (RCB), and 2. a convective lower atmosphere, where the temperature profile follows an adiabatic gradient. RCB temperature is determined by radiative equilibrium, assuming an albedo of 0.3:

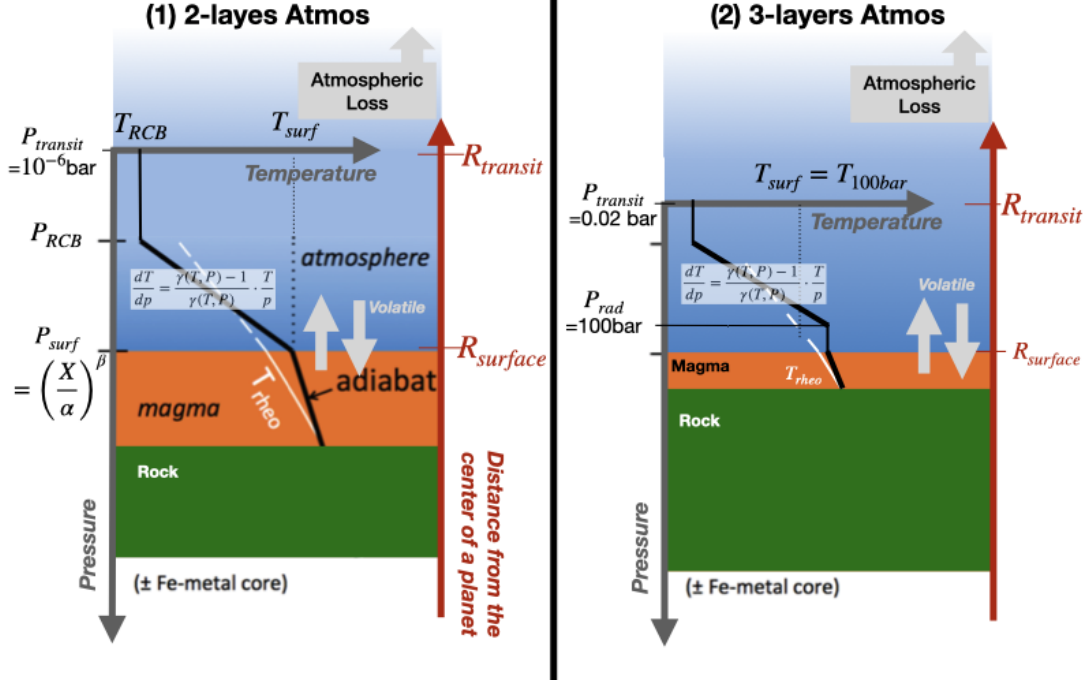


**Figure 5:** Planetary Thermal Structure and Two End-Member Estimates for Transit Radius. The thin black line denotes an isothermal atmosphere in the radiative layer, while the thick black line represents an adiabatic profile in the convective layer. The adiabatic index  $\gamma$  varies with temperature and pressure, as shown in Fig. B11. The radiative-convective boundary (RCB) temperature is set by energy balance with an albedo of 0.3:  $T_{RCB} = ((1 - 0.3)S/\sigma)^{1/4}$ . The surface temperature ( $T_{surf}$ ) is calculated by extending the dry adiabatic profile from the RCB to the surface (a) or to the top of the radiative layer near the surface (b). The white line corresponds to the rheological transition ( $\sim 40\%$  melt fraction) P-T relation for rock, with dashed white sections indicating depths where no rock is present. If  $T_{surf} > T_{rheo}(P = P_{surf})$ , the surface is molten, forming a magma ocean. The intersection of the thick black line with the white line marks the depth at which magma crystallizes, defining the extent of the magma layer. Volatiles are assumed to be partitioned between the magma and atmosphere, with surface pressure governed by the solubility law as a function of the volatile concentration in the magma ( $X$ ): ( $P_{surf} = (X/\alpha)^\beta$ ), where  $\alpha$  and  $\beta$  are obtained from T. Lichtenberg et al. (2021a). The pressure level probed during a transit ( $P_{transit}$ ) is set to a constant value, with the corresponding altitude determined under hydrostatic balance. Gravity ( $g$ ) changes with altitude in our calculation. The transit radius ( $R_{transit}$ ), measured radius via the transit method, is the distance from this altitude to the planetary center. (1) Upper-limit estimate of atmospheric height: Assumes the entire atmosphere below the RCB is fully convective, following a dry adiabatic profile.  $P_{transit} = 10^{-6}$  bar. (2) Lower-limit estimate of atmospheric height: Assumes a radiative layer extends from the surface up to  $P = 100$  bar.  $P_{transit} = 0.02$  bar.

$$T_{RCB} = \left( \frac{(1 - 0.3)S}{4\sigma} \right)^{1/4} \quad (6)$$

where  $S$  is the instellation, and  $\sigma$  is the Stefan-Boltzmann constant. This formulation assumes that heat is efficiently redistributed across the planet by a thick atmosphere, leading to a uniform temperature distribution. Below the RCB, the surface temperature ( $T_{surf}$ ) is obtained by integrating a dry adiabatic profile down to the surface. In the convective region, where pressure and temperature vary significantly, the heat capacity ratio ( $\gamma$ ) is not constant but instead depends on both temperature and pressure. We account for this variation by expressing  $\gamma$  as a function of these parameters, computed using NASA's Chemical Equilibrium with Applications (CEA) tool<sup>9</sup> (S. Gordon & B. J. McBride 1994), as shown in Fig. B11.

For thick  $\text{CO}_2$ -dominated atmospheres, however, the convective zone may not extend all the way to the surface. Instead, a radiative-equilibrium isothermal layer can develop near the surface due to strong absorption of stellar

<sup>9</sup> <https://cearun.grc.nasa.gov/>

Dependence of Atmospheric Puffiness on Volatile Fraction at  $T_{eq} = 1000K$

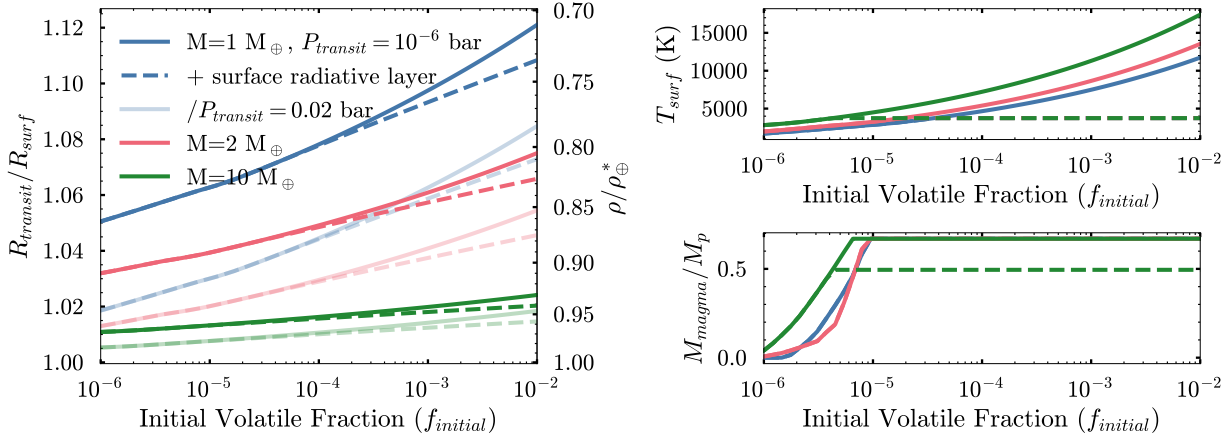


**Figure 6:** Atmospheric Radius Boosting effect. Left: The ratio of the transit radius to the radius of the solid surface (including the magma layer if present) as a function of the initial volatile fraction ( $f_{\text{initial}}$ ). The right y-axis shows the corresponding ratioed density. Solid lines correspond to the two-layer model (Scenario (a) in Fig. 5) with  $P_{\text{transit}} = 10^{-6}$  bar, where the atmosphere consists of a convective lower layer and an isothermal upper layer beyond the radiative-convective boundary (RCB). Dashed lines represent the three-layer model (Scenario (b) in Fig. 5 but with adjusted  $P_{\text{transit}}$ ), which includes an additional radiative layer near the surface. The lighter-colored lines indicate the same atmospheric conditions, but the transit radius is measured at  $P_{\text{transit}} = 0.02$  bar. Upper Right: Surface temperature for the different atmospheric scenarios described above. At  $T \gtrsim 10^4 K$ , the silicate and Fe will expand (S. J. Lock & S. T. Stewart 2017), which is not considered in our model. Lower Right: Magma ocean mass fraction for different atmospheric structures. The layered structure of the atmosphere influences the transit radius only when  $f_{\text{initial}}$  is sufficiently high for the surface pressure to exceed 100 bar. The choice of  $P_{\text{transit}}$  has a much greater impact on the derived transit radius than the atmospheric structure alone.

radiation and internal heating (F. Selsis et al. 2023; B. Peng & D. Valencia 2024). Since a full radiative transfer calculation is beyond the scope of this model, we adopt a simplified assumption: in the lower-limit estimate of atmospheric height (panel (2) of Fig. 5), the radiative layer begins at a pressure of 100 bar. This assumption allows us to explore the potential range of atmospheric extent while acknowledging uncertainties in radiative transport.

The extent of a possible magma ocean is constrained by the rheological transition temperature ( $T_{\text{rheo}}$ ) at a given pressure, corresponding to  $\sim 40\%$  melt fraction for silicate rock (following the method of E. S. Kite & M. N. Barnett (2020) using D. Andraut et al. (2011)). If  $T_{\text{surf}} > T_{\text{rheo}}(P = P_{\text{surf}})$ , the surface remains molten, and volatiles can continue to exchange between the atmosphere and magma ocean. The partitioning of volatiles is governed by a solubility law that relates surface pressure to the volatile concentration in the magma ( $X_{\text{magma}}$ ):

$$P_{\text{surf}} = (X_{\text{magma}}/\alpha)^\beta \quad (7)$$

where  $\alpha = 1.94 \times 10^{-3}$  and  $\beta = 0.714$  are empirical parameters for  $\text{CO}_2$  obtained from T. Lichtenberg et al. (2021a). We acknowledge that solubility depends on both temperature and pressure; our model considers only pressure.

To link this atmospheric model to transit observations, we assume ( $P_{\text{transit}}$ ) as a constant value obtained from previous studies. The altitude at this level is derived by assuming hydrostatic balance. Two end-member scenarios are considered for estimating the atmospheric height:

1. Upper-limit estimate: The atmosphere below the RCB is assumed to be fully convective, following a dry adiabatic profile. The transit pressure is set to  $P_{\text{transit}} = 10^{-6}$  bar, which is set by cloud top (P. Gao et al. 2020).
2. Lower-limit estimate: A radiative layer is assumed to develop near the surface, limiting atmospheric expansion. The transit pressure is set to  $P_{\text{transit}} = 0.02$  bar (E. D. Lopez et al. 2012), where the opacity source is clear sky.

By applying this model, we can investigate how instellation and volatile content influence the transit radius  $R_{\text{transit}}$ ,



**Table 3:** Model input parameters used for Monte Carlo simulation.

Parameter	Distribution / Range	Description
$M_*$	$U(0.1, 1)$	Stellar mass.
$M_p$	$U(0.5, 1)$	Planetary mass.
$S/S_0$	$10^{U(1,4)}$	Bolometric instellation scaled to Earth value.
$f_{\text{initial}}$	$10^{U(-4, -2)}$	Initial volatile fraction.
$R_p$	(a) $R_{\oplus}^*$ (b) $N(R_{\oplus}^*, \sigma); \sigma = (R_{\text{silicate}}^* - R_{\oplus}^*)/3$ (c) $N(R_{\oplus}^*, \sigma); \sigma = (R_{\text{silicate}}^* - R_{\oplus}^*)$	Planetary radius

which accounts for both the solid body (including magma layer) and the atmospheric height at  $P_{\text{transit}}$  (Fig. 6).

Since planetary mass ( $M_p$ ) can often be constrained through radial velocity measurements or TTVs, we can get planet density using the transit radius:  $\rho = M_p / \frac{4}{3}\pi R_{\text{transit}}^3$ . Because the transit radius includes the atmospheric contribution, the measured density ( $\rho$ ) will always be lower than the density of the solid portion of the planet alone for worlds with thick atmosphere. Comparing the observed density to theoretical models of rocky planets can help distinguish planets with substantial atmospheres from bare rocky worlds.

### 5.2. Monte Carlo Simulations

We use a Monte Carlo approach similar to the one described in Sec. 2, but with additional variables, incorporating the final atmospheric height after loss and the corresponding planetary density. The newly introduced variables and their distributions are listed in Table 3.

To quantify the variation in the bulk density of the solid portion of the planet (S. Xu & A. Bonsor 2021), we generate three samples under different assumptions about the distribution of planetary radii. Given a planetary mass ( $M_p$ ), the radius is assigned according to the following distributions:

- (a) No Compositional Variance.: Fixed Earth-like Composition: The radius is set to  $R_{\oplus}^*(M_p)$ , assuming a composition of 32.5% Fe + 67.5% MgSiO<sub>3</sub>.
- (b) Narrow Normal Distribution: The radius is drawn from a normal distribution centered at  $R_{\oplus}^*(M_p)$ , with a standard deviation equal to one-third of the difference between  $R_{\oplus}^*(M_p)$  and  $R_{\text{silicate}}^*(M_p)$ , where  $R_{\text{silicate}}^*(M_p)$  corresponds to a pure MgSiO<sub>3</sub> composition.
- (c) Wide Normal Distribution: The radius is drawn from a normal distribution centered at  $R_{\oplus}^*(M_p)$ , with a standard deviation of the difference between  $R_{\oplus}^*(M_p)$  and  $R_{\text{silicate}}^*(M_p)$ .

All calculations are based on the mass-radius relations provided by L. Zeng et al. (2019). Since the maximum volatile fraction in our simulations is limited to 1% of the planetary mass, we neglect any contribution of atmospheric mass to  $M_p$ . The mass-radius diagram for the solid-body of planets, showing these compositional variations, is presented in Fig. B13. The symmetric sampling of radii introduces a bias, leading to a fat tail of low-density planets. Among the tested scenarios, scenario (b) is the most realistic.

For each assumption regarding solid-body density variation, we generate  $10^4$  data points and compute their time-integrated atmospheric loss. Using the remaining atmosphere, we then determine the corresponding transit radius using both upper- and lower-limit estimates and density. The density is then normalized by a theoretical model of an Earth-like composition ( $\rho/\rho_{\oplus}^*$ ) (L. Zeng et al. 2019).

### 5.3. Predictions with Cosmic Shoreline

We present the results of Monte Carlo simulations under assumptions (a) and (b) in Fig. 7. The two middle panels show planetary mass against equilibrium temperature, an alternative representation of the traditional cosmic shoreline format, as escape velocity scales with planetary mass, and equilibrium temperature is derived from instellation.

In panel (a), where all planets are assumed to have an Earth-like composition, the ratioed density  $\rho/\rho_{\oplus}^*$  does not exceed 1. The light yellow dots, representing planets with a ratioed density of 1, correspond to bare rocky planets that

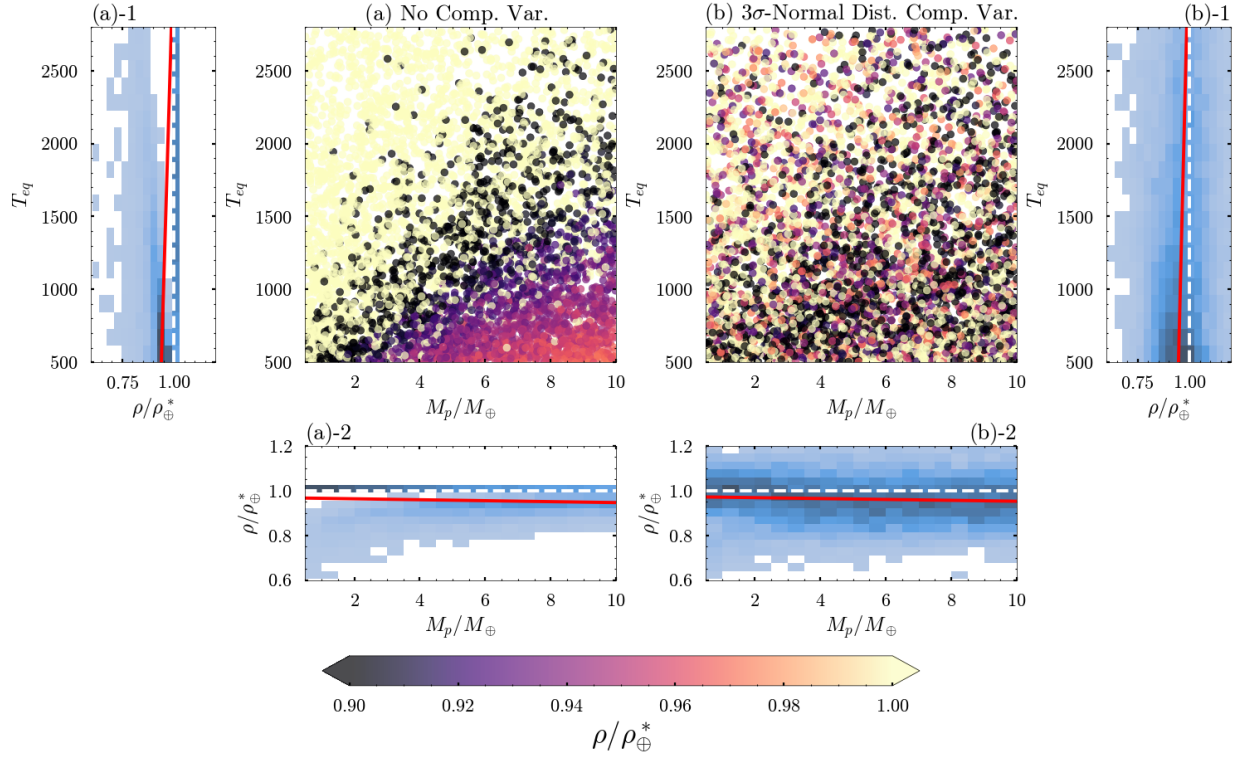


**Figure 7:** How the cosmic shoreline shapes the trend of ratioed density ( $\rho/\rho_{\oplus}^*$ ) for Different Assumptions of Solid-Body Density Distribution (Scenario (a) and (b) as seen in Table 3). Panels (a) and (b) present scatter plots of a subset of  $10^3$  planets, plotted as planetary mass ( $M_p$ ) against equilibrium temperature ( $T_{eq}$ )—an alternative representation of the traditional cosmic shoreline format, since  $v_{esc}$  scales with  $M_p$ , and  $T_{eq}$  is derived from instellation ( $S/S_0$ ). The dots are color-coded by the ratioed density with the upper-limit estimate, where atmosphere has two layers and  $P_{transit} = 10^{-6}$  bar. In (a), the cosmic shoreline shapes the boundary between yellow dots (bare rocks without atmosphere) and black dots (planets where the radius-boosting effect of an atmosphere is most distinguishable). In (b), where solid-body density varies, the transition is less distinct, but a visual trend remains, with more yellow points clustered in the upper-left region (high-temperature, low-mass planets), indicating that atmospheric loss is more severe in this regime. For better visualization, the color scale is limited between 0.9 and 1.0, although actual density values can extend beyond this range. Panels (a)-1 and (b)-1: A bivariate histogram is computed and visualized as a heatmap, where darker colors indicate higher number density. Linear regression of  $\rho/\rho_{\oplus}^*$  as a function of equilibrium temperature ( $T_{eq}$ ) for the full 10,000-planet sample. A decreasing trend is observed, as planets at high  $T_{eq}$  are more likely to be bare rocks with higher densities. Panels (a)-2 and (b)-2: Linear regression of  $\rho/\rho_{\oplus}^*$  as a function of planetary mass ( $M_p$ ), also showing a decreasing trend. This is because lower-mass planets are more likely to be stripped of their atmospheres, leading to a larger fraction of high-density bare rocky planets at lower masses.

have completely lost their atmospheres. These planets are adjacent to the black dots, which exhibit the lowest ratioed density due to a substantial atmospheric contribution and a more pronounced radius-boosting effect. The transition zone from yellow to black dots follows the shape of the cosmic shoreline, as shown in Fig. 3. This boundary is not a strict cutoff but rather a transition zone influenced by factors such as initial volatile content and other parameters listed in Table 2.

Starting from the transition zone, for planets with  $\rho/\rho_{\oplus}^* < 1$ , the ratioed density exhibits a trend of increasing toward the lower right (higher mass, lower irradiation planets). Two key factors contribute to this effect: 1. Atmospheric survival constraint: Retaining an atmosphere requires that the initial volatile content exceeds the cumulative atmospheric mass loss over time. Since total atmospheric loss increases with increasing  $T_{eq}$ , planets with low volatile inventories are more likely to be completely stripped, leaving behind bare rocky cores. Conversely, planets with significantly higher initial volatile content can sustain substantial atmospheres, leading to pronounced radius inflation. 2. Atmospheric radius-boosting effect: At higher  $T_{eq}$ , atmospheric scale heights are larger due to increased thermal expansion. This

amplifies the difference in transit radius between atmosphere-bearing and stripped planets, making the contrast in radiod density more prominent even if the absolute atmospheric mass is similar.

A similar but less pronounced trend appears in panel (a)-2, where the radiod density increases with planetary mass. This is driven by the same mechanisms: higher-mass planets have stronger gravity and stronger cooling effect, making atmospheric retention easier, while also experiencing a less pronounced radius-boosting effect from a given atmospheric mass.

We show bivariate histograms and perform linear regression for radiod density as a function of  $T_{\text{eq}}$  in panel (a)-1 and as a function of planetary mass ( $M_p$ ) in panel (a)-2. The horizontal line at  $\rho/\rho_{\oplus}^* = 1$  consists of planets that have completely lost their atmospheres. Along this line, the color transitions from dark to light as  $M_p$  increases and  $T_{\text{eq}}$  decreases, indicating that fewer planets experience complete atmospheric loss, while more planets retain sufficient volatiles, resulting in  $\rho/\rho_{\oplus}^* < 1$ . Consequently, the linear regression exhibits a decreasing trend with decreasing  $T_{\text{eq}}$ .

In panel (a)-1, at high  $T_{\text{eq}}$ , a distinct gap appears between the atmosphere-bearing planets ( $\rho/\rho_{\oplus}^* < 1$ ) and the completely stripped rocky cores ( $\rho/\rho_{\oplus}^* = 1$ ). As  $T_{\text{eq}}$  decreases, the gap narrows, reflecting the reduced impact of atmospheric expansion and mass loss. This trend aligns with the color transition in the scatter plot.

For assumption (b) of narrow normal distribution, the variation in the solid portion's density introduces scatter, making the distinct trends observed in (a) less visually apparent. The transition zone between atmosphere-bearing and stripped planets becomes more diffuse. Despite this, the linear regression still reveals a consistent decreasing trend in radiod density with decreasing  $T_{\text{eq}}$  and increasing  $M_p$ , similar to (a). This suggests that despite the uncertainty in solid-body density, the underlying effect of atmospheric retention and loss, as shaped by the cosmic shoreline, remains statistically significant. We do not present results for assumption (c), as it follows a similar pattern with even greater scatter while preserving the same overall statistical behavior.

The decreasing trend in radiod density is statistically significant for a sample of 10,000 planets, but it may not be reliably detected with smaller sample sizes. To estimate the minimum number of observed exoplanets required to confirm this trend, we conduct a 500-time bootstrap analysis.

We assume that mass measurement errors are much smaller than the intrinsic variations in solid composition and did not add observational bias. We draw subsamples from our 10,000-planet sample without replacement. For each subsample of a given size, we perform a linear regression to obtain the slope of the radiod density trend. Repeating this process 500 times, we construct a distribution of slope values for each sample size. The 90% confidence interval of this distribution is represented by the shaded region in Fig. 8, indicating the range within which the slope is expected to vary. Where the whole shaded region crosses the line slope=0 gives an estimate of the minimum number of observed exoplanets needed to confirm the expected density trend influenced by atmospheric loss and the cosmic shoreline.

In Fig. 8, we present the results of our bootstrap analysis for both the lower- and upper-limit estimates of the transit radius. For assumption (a), where all planets have an Earth-like composition, there is no significant difference between the two estimates. However, for assumption (b), where the solid density follows a normal distribution, the required sample size for detecting the trend in the lower-limit estimate is approximately twice as large as that for the upper-limit estimate.

For assumptions (a) and (b), the decreasing trend of  $\rho/\rho_{\oplus}^*$  with  $T_{\text{eq}}$  could be constrained with a sample of  $\sim 100$  exoplanets. However, constraining the trend with planetary mass ( $M_p$ ) requires a larger sample size. If the variation in solid composition is as large as in assumption (c), the required sample size exceeds 1000, making it difficult to detect the trend with near-future exoplanet observations.

Here, we propose a novel approach to examine the cosmic shoreline, but it remains challenging to achieve with current exoplanet data. Transit and emission spectroscopy remain the most effective methods for constraining the shoreline.

## 6. DISCUSSION

The hydrodynamic simulations discussed in Sec. 2.3 have many uncertainties. These simulations provide atmospheric loss rates as a function of XUV flux; however, the XUV wavelength range varies across models. For example, F. Tian (2009) and C. P. Johnstone (2020) consider XUV wavelengths up to 1050 Å and 1000 Å, respectively, while A. Nakayama et al. (2022) restricts the range to 910 Å to exclude Lyman- $\alpha$  emission. Although the resulting impact is not explicitly included in our model, it is expected to fall within the uncertainties of our EUV extrapolation, as I. Ribas et al. (2005) shows that the flux ratio between 920–1180 Å and 1–920 Å is 0.03 for a 0.1 Gyr star and 0.2 for the Sun.

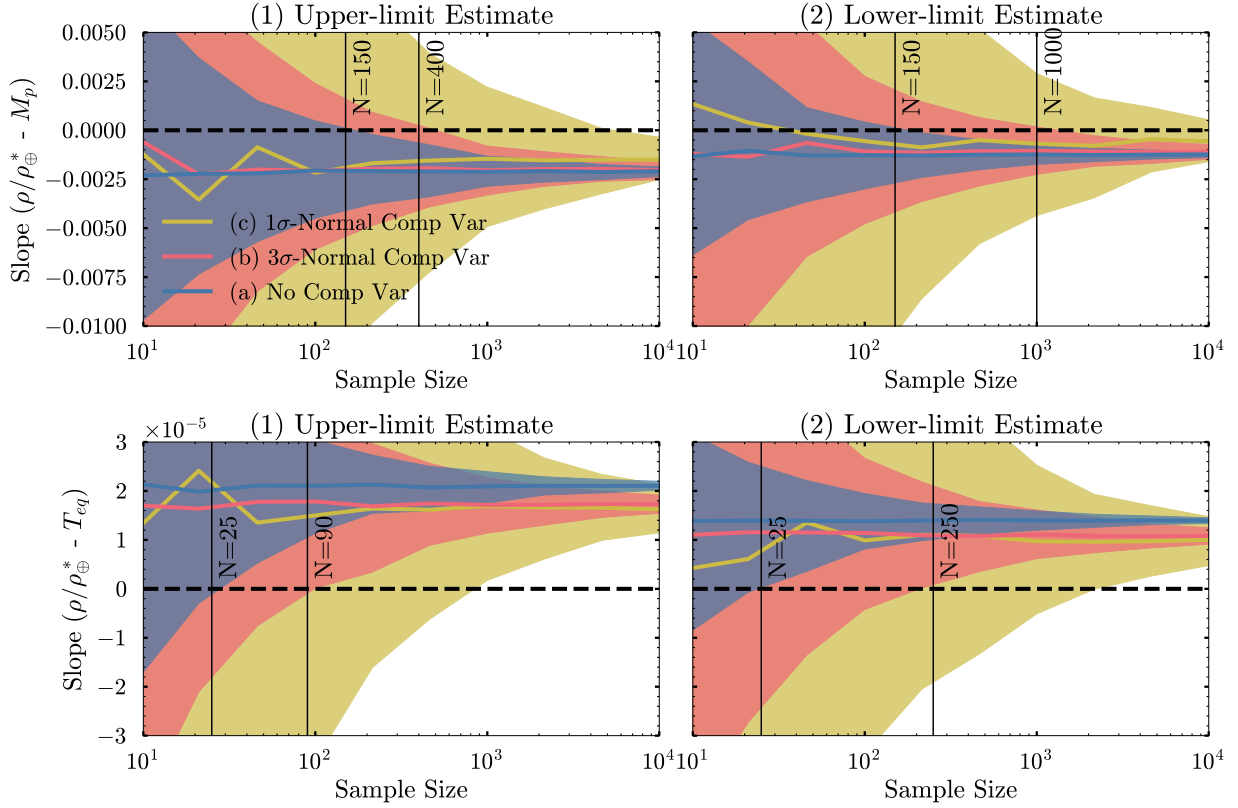


**Figure 8:** Constraining the slope of ratioed density trends with varying sample sizes. Column (1) corresponds to the upper-limit estimate of the transit radius, where atmosphere has two layers and  $P_{transit} = 10^{-6}$ bar, while column (2) represents the lower-limit estimate, where atmosphere has three layers and  $P_{transit} = 0.02$ bar. The upper row illustrates how well the slope of the scaled density ( $\rho/\rho_{\oplus}^*$ ) as a function of planetary mass ( $M_p$ ) can be constrained, which is negative when considering the full sample of  $10^4$  simulated planets. The lower row presents the same analysis for equilibrium temperature ( $T_{eq}$ ), where the slope is positive for the full sample. The solid lines indicate the median slope values derived from bootstrap resampling, while the shaded regions represent the 90% confidence intervals. The results illustrate how increasing the sample size improves the precision of the slope estimation, with the equilibrium temperature trend being more robustly constrained than the planetary mass trend.

Additionally, Table 1 in [C. P. Johnstone \(2020\)](#) provides an X-ray-to-EUV relation that deviates from our EUV extrapolation, suggesting differences in spectral shapes between our model and their input, as well as potential differences from other hydrodynamic simulations. We do not know the cause of the difference. However, [C. P. Johnstone et al. \(2021\)](#) show a consistent relation (Fig. B3)

[A. Nakayama et al. \(2022\)](#) show that atomic line cooling can cool the upper atmosphere sufficiently to prevent hydrodynamic escape. This effect is also emphasized by [M. Zhang et al. \(2022b\)](#). Other radiative cooling effects affect hydrodynamic escape of mineral atmospheres ([Y. Ito & M. Ikoma 2021](#)) and  $H_2$ -rich atmospheres. These include contributions from Lyman- $\alpha$  cooling (e.g., [R. A. Murray-Clay et al. 2009](#); [M. Zhang et al. 2022b](#), but see also [D. Linssen et al. 2024](#)), metal cooling (e.g., [T. Yoshida & K. Kuramoto 2020](#); [M. Zhang et al. 2022b](#); [T. Yoshida et al. 2022](#); [M. Zhang et al. 2024](#); [D. Linssen et al. 2024](#); [R. Rosener et al. 2025](#)), and molecular cooling ([T. Yoshida et al. 2024](#)).

However, some inconsistencies exist between [A. Nakayama et al. \(2022\)](#) and other studies. [R. D. Chatterjee & R. T. Pierrehumbert \(2024\)](#), suggests that in the scenarios modeled by [A. Nakayama et al. \(2022\)](#), considering an ionized exobase would push the atmosphere into a hydrodynamic regime, enhancing escape. Furthermore, including ambipolar diffusion could increase the escape rate. More work is needed to understand the processes to interpret JWST data.

In this study, we argue that the solid mantle volatile content is much smaller than the volatile in magma and atmosphere, so we neglect that part. However, if the initial volatile inventory is exceptionally high, even a small

fraction trapped in the mantle could later outgas via volcanism to form a detectable atmosphere. Additionally, for  $\text{N}_2/\text{O}_2$  atmospheres, revival through a water loss redox pump is more likely, which is time-dependent (R. D. Wordsworth 2016; L. Schaefer et al. 2016; E. S. Kite & L. Schaefer 2021). Thus models that incorporates escape-driven magma ocean solidification, chemical equilibrium, mantle outgassing, and atmospheric evolution along with stellar evolution are needed (e.g., E. S. Kite & M. N. Barnett 2020; J. Krissansen-Totton 2023; J. Krissansen-Totton et al. 2024).

The EUV extrapolation and stellar mass loss scaling used in our model assume that the observed spectral of the Sun are representative of other stars, which may not account for the diversity in stellar properties and activity levels. For X-ray, we just accept standard models but the stars might differ from each other (T. Penz et al. 2008; L. Tu et al. 2015). For example, some stars might stay in the saturated phase for different lengths of time. These variations could lead to a variation of integrated X-ray, EUV, and XUV emissions.

As a test, we prescribe a non-thermal ion escape rate for  $\text{CO}_2$ -dominated atmospheres. The stellar mass loss rate due to coronal wind is estimated using the scaling law from B. E. Wood et al. (2021):

$$\log_{10} \left[ \frac{\dot{M}_*}{4\pi R_*^2} \left( \frac{M_\odot}{4\pi R_\odot^2} \right)^{-1} \right] = k_{\dot{M}} \cdot \log_{10} \left( \frac{F_{X,*}}{F_{X,\odot}} \right) + 0.35 \quad (8)$$

where  $\dot{M}_*$  is the stellar mass loss rate (kg/s),  $R_*$  is the stellar radius (obtained from the Baraffe model), and  $F_X$  is the stellar X-ray flux at the stellar surface, all scaled to solar values. The fitting parameter  $k_{\dot{M}} = 0.77 \pm 0.04$ , with an intercept of 0.35 calibrated to GJ 887.

We then use the 3D magnetohydrodynamic simulations from L. Chin et al. (2024) for unmagnetized rocky exoplanets, normalizing their ion escape rates using Eq. 2 from C. Dong et al. (2018) to derive the loss coefficient  $\dot{M}_{C,0}$ , allowing us to calculate the carbon loss rate under varying stellar wind conditions:

$$\dot{M}_C = \dot{M}_{C,0} \cdot \left( \frac{R_p}{a_p} \right)^2 \dot{M}_* \quad (9)$$

where  $\dot{M}_C$  is the carbon loss rate,  $R_p$  is the planetary radius, and  $a_p$  is the planet's semi-major axis. The C loss rate accounts only for  $\text{CO}_2^+$  ions, based on the chemical reactions in Table 2 of C. Dong et al. (2017). The stellar mass loss rate used in L. Chin et al. (2024) is  $\dot{M}_{*,0} = 9.29 \times 10^{-13} M_\odot/\text{yr}$ .

We find that non-thermal  $\text{CO}_2$  loss rates are two orders of magnitude lower than thermal escape rates and therefore exclude them from further analysis.

Additionally, impact erosion can significantly strip atmospheres, particularly during the early stages of planetary formation (e.g., H. E. Schlichting & S. Mukhopadhyay 2018; J. A. Kegerreis et al. 2020; M. C. Wyatt et al. 2020). The influence of planetary magnetic fields, which can mitigate atmospheric escape O. Cohen et al. (2014), and the role of occasional but intense stellar activity cycles in modulating escape rates, also warrant further investigation (W. Wagner 1988; J. M. Chadney et al. 2015; W. G. Levine et al. 2024). Additionally, it is important to understand how cooling effects and the resulting escape rates change with various atmospheric mixtures. Incorporating these factors into future studies is warranted.

This study provides a first-step analysis of how density trends can be used to test the cosmic shoreline (Sec. 5), but it is based on simplified assumptions and considers only  $\text{CO}_2$ -dominated atmospheres. Future work might expand to include atmospheres with varied compositions and incorporate a more realistic atmospheric structure, especially for the possible thermal inversion under high-pressure and high-temperature conditions (F. Selsis et al. 2023), and determine transit radii using detailed radiative transfer calculations.

In Sec. 5, we only considered density variations in the solid body while centering the composition around an Earth-like composition. We also did a sensitivity test with an alternative assumption where planetary radii are uniformly distributed between  $R_{\text{silicate}}(M_p)$  and  $R_{\text{iron}}(M_p)$ . Under this assumption, the scaled density  $\rho/\rho_{\oplus\text{-like}}$  retains the same decreasing trend with decreasing equilibrium temperature. However, it exhibits an increasing trend with planetary mass. This arises from the intrinsic mass-radius relation of the solid body alone (see Fig. B13), where more massive planets tend to have higher solid-body densities. This introduces a potential complication in interpreting the trend, as any dependence of solid-body composition on  $M_p$  and/or  $T_{\text{eq}}$  could contribute to or alter the pattern. Further investigation is needed to disentangle the influence of atmospheric retention from intrinsic density variations of the planetary core (D. Valencia et al. 2007; L. A. Rogers & S. Seager 2010).

Even if the density variations are centered around an Earth-like composition, our results indicate that achieving



statistically significant conclusions with near-future datasets will be challenging. Additionally, we have not accounted for observational uncertainties. Therefore, JWST transmission and emission spectroscopy remain the most effective methods for detecting atmospheres on rocky planets and testing the cosmic shoreline.

## 7. CONCLUSION

With the cosmic shoreline defined as the critical bolometric instellation ( $S_{bol}^*$ ) above which a planet is highly unlikely to retain its atmosphere, given the mass of volatile available for loss, we use the results of previous hydrodynamic atmospheric models (F. Tian 2009; F. Tian et al. 2009; C. P. Johnstone 2020; A. Nakayama et al. 2022; R. D. Chatterjee & R. T. Pierrehumbert 2024) and stellar evolution models (I. Baraffe et al. 2015; A. P. Jackson et al. 2012; F. Selsis et al. 2023; G. W. King & P. J. Wheatley 2020) and find:

1. Cosmic shoreline as a transition zone: The location of the cosmic shoreline depends on atmospheric composition and initial volatile content. Instead of a sharp dividing line, we expect a gradual transition between airless worlds and planets retaining substantial atmospheres. Atmosphere non-detection can help constrain the maximum volatile content which may applies for other planets in the system.
2. Dependence on stellar mass: The cosmic shoreline shifts towards higher instellation with increasing stellar mass, as higher-mass stars emit less cumulative XUV radiation over their lifetimes. As a result, planets orbiting Sun-like stars are more likely to retain their atmospheres compared to those around lower-mass stars. (F. Tian 2015a; F. Tian & S. Ida 2015)
3. Dependence on planetary mass: The cosmic shoreline also shifts towards higher instellation with increasing planetary mass, and this shift is more pronounced than in traditional cosmic shoreline estimates due to strong radiative line cooling.
4. New metric: To account for this, we introduce a priority metric that quantifies the difference between a planet's instellation and the critical instellation required for atmospheric retention at a given planetary mass. A ranked list of target exoplanets based on this metric is provided in Table 3.
5. Testing the cosmic shoreline with scaled density: Due to the radius-boosting effect of atmospheres, the scaled density ( $\rho/\rho_{\oplus\text{-like}}$ ) provides an alternative way to test the cosmic shoreline. Since atmospheric retention becomes less likely at higher instellation and lower planetary mass, an increasing trend in scaled density with increasing instellation and decreasing planetary mass could be tested using  $\sim 100$  exoplanets. However, it is difficult to achieve in the near future due to limited database.

This research has made use of the NASA Exoplanet Archive, which is operated by the California Institute of Technology, under contract with the National Aeronautics and Space Administration under the Exoplanet Exploration Program. We thank Michael Zhang, David Catling, Ted Bergin, Dorian Abbot, RJ Graham, Bowen Fan, Robin Wordsworth, Jegu Ih, Madison Brady, Caroline Piaulet, and Lily Zhao for insightful discussions.

## REFERENCES

- |   |  |
|---|--|
| <p>Adibekyan, V., Deal, M., Dorn, C., et al. 2024, Linking the primordial composition of planet building disks to the present-day composition of rocky exoplanets, <i>Astronomy and Astrophysics</i>, 692, A67, doi: <a href="https://doi.org/10.1051/0004-6361/202452193">10.1051/0004-6361/202452193</a></p> <p>Andrault, D., Bolfan-Casanova, N., Nigro, G. L., et al. 2011, Solidus and liquidus profiles of chondritic mantle: Implication for melting of the Earth across its history, <i>Earth and Planetary Science Letters</i>, 304, 251, doi: <a href="https://doi.org/10.1016/j.epsl.2011.02.006">10.1016/j.epsl.2011.02.006</a></p> | <p>August, P. C., Buchhave, L. A., Diamond-Lowe, H., et al. 2025, Hot Rocks Survey I: A possible shallow eclipse for LHS 1478 b, <i>Astronomy &amp; Astrophysics</i>, 695, A171, doi: <a href="https://doi.org/10.1051/0004-6361/202452611">10.1051/0004-6361/202452611</a></p> <p>Baraffe, I., Homeier, D., Allard, F., &amp; Chabrier, G. 2015, New evolutionary models for pre-main sequence and main sequence low-mass stars down to the hydrogen-burning limit, <i>Astronomy &amp; Astrophysics</i>, 577, A42, doi: <a href="https://doi.org/10.1051/0004-6361/201425481">10.1051/0004-6361/201425481</a></p> |
|---|--|

- Benneke, B., Roy, P.-A., Coulombe, L.-P., et al. 2024, JWST Reveals CH<sub>4</sub>, CO<sub>2</sub>, and H<sub>2</sub>O in a Metal-rich Miscible Atmosphere on a Two-Earth-Radius Exoplanet, arXiv, doi: [10.48550/ARXIV.2403.03325](https://doi.org/10.48550/ARXIV.2403.03325)
- Bergin, E. A., Blake, G. A., Ciesla, F., Hirschmann, M. M., & Li, J. 2015, Tracing the ingredients for a habitable earth from interstellar space through planet formation, *Proceedings of the National Academy of Sciences*, 112, 8965, doi: [10.1073/pnas.1500954112](https://doi.org/10.1073/pnas.1500954112)
- Bergin, E. A., Kempton, E. M.-R., Hirschmann, M., et al. 2023, Exoplanet Volatile Carbon Content as a Natural Pathway for Haze Formation, *The Astrophysical Journal Letters*, 949, L17, doi: [10.3847/2041-8213/acd377](https://doi.org/10.3847/2041-8213/acd377)
- Blanchard, I., Rubie, D., Jennings, E., et al. 2022, The metal-silicate partitioning of carbon during Earth's accretion and its distribution in the early solar system, *Earth and Planetary Science Letters*, 580, 117374, doi: [10.1016/j.epsl.2022.117374](https://doi.org/10.1016/j.epsl.2022.117374)
- Bond, J. C., Lauretta, D. S., & O'Brien, D. P. 2010, Making the Earth: Combining dynamics and chemistry in the Solar System, *Icarus*, 205, 321, doi: [10.1016/j.icarus.2009.07.037](https://doi.org/10.1016/j.icarus.2009.07.037)
- Caldioli, A., Haardt, F., Gallo, E., et al. 2022, Irradiation-driven escape of primordial planetary atmospheres: II. Evaporation efficiency of sub-Neptunes through hot Jupiters, *Astronomy & Astrophysics*, 663, A122, doi: [10.1051/0004-6361/202142763](https://doi.org/10.1051/0004-6361/202142763)
- Catling, D. C., & Kasting, J. F. 2017, Atmospheric Evolution on Inhabited and Lifeless Worlds. <https://ui.adsabs.harvard.edu/abs/2017aeil.book.....C>
- Chadney, J. M., Galand, M., Unruh, Y. C., Koskinen, T. T., & Sanz-Forcada, J. 2015, XUV-driven mass loss from extrasolar giant planets orbiting active stars, *Icarus*, 250, 357, doi: [10.1016/j.icarus.2014.12.012](https://doi.org/10.1016/j.icarus.2014.12.012)
- Chatterjee, R. D., & Pierrehumbert, R. T. 2024, Novel Physics of Escaping Secondary Atmospheres May Shape the Cosmic Shoreline, arXiv, doi: [10.48550/arXiv.2412.05188](https://doi.org/10.48550/arXiv.2412.05188)
- Chen, H., & Jacobson, S. A. 2022, Impact induced atmosphere-mantle exchange sets the volatile elemental ratios on primitive Earths, *Earth and Planetary Science Letters*, 594, 117741, doi: [10.1016/j.epsl.2022.117741](https://doi.org/10.1016/j.epsl.2022.117741)
- Chin, L., Dong, C., & Lingam, M. 2024, Role of Planetary Radius on Atmospheric Escape of Rocky Exoplanets, *The Astrophysical Journal Letters*, 963, L20, doi: [10.3847/2041-8213/ad27d8](https://doi.org/10.3847/2041-8213/ad27d8)
- Cloutier, R., & Menou, K. 2020, Evolution of the radius valley around low-mass stars from Kepler and K2, *The Astronomical Journal*, 159, 211
- Cohen, O., Drake, J. J., Gloer, A., et al. 2014, MAGNETOSPHERIC STRUCTURE AND ATMOSPHERIC JOULE HEATING OF HABITABLE PLANETS ORBITING M-DWARF STARS, *The Astrophysical Journal*, 790, 57, doi: [10.1088/0004-637X/790/1/57](https://doi.org/10.1088/0004-637X/790/1/57)
- Coy, B. P., Ih, J., Kite, E. S., et al. 2024, Population-level Hypothesis Testing with Rocky Planet Emission Data: A Tentative Trend in the Brightness Temperatures of M-Earths, arXiv, doi: [10.48550/arXiv.2412.06573](https://doi.org/10.48550/arXiv.2412.06573)
- Demory, B.-O., Gillon, M., De Wit, J., et al. 2016, A map of the large day-night temperature gradient of a super-Earth exoplanet, *Nature*, 532, 207, doi: [10.1038/nature17169](https://doi.org/10.1038/nature17169)
- Denman, T. R., Leinhardt, Z. M., Carter, P. J., & Mordasini, C. 2020, Atmosphere loss in planet-planet collisions, *Monthly Notices of the Royal Astronomical Society*, 496, 1166, doi: [10.1093/mnras/staa1623](https://doi.org/10.1093/mnras/staa1623)
- Dong, C., Jin, M., Lingam, M., et al. 2018, Atmospheric escape from the TRAPPIST-1 planets and implications for habitability, *Proceedings of the National Academy of Sciences*, 115, 260, doi: [10.1073/pnas.1708010115](https://doi.org/10.1073/pnas.1708010115)
- Dong, C., Lingam, M., Ma, Y., & Cohen, O. 2017, Is Proxima Centauri b Habitable? A Study of Atmospheric Loss, *The Astrophysical Journal Letters*, 837, L26, doi: [10.3847/2041-8213/aa6438](https://doi.org/10.3847/2041-8213/aa6438)
- Elkins-Tanton, L. 2008, Linked magma ocean solidification and atmospheric growth for Earth and Mars, *Earth and Planetary Science Letters*, 271, 181, doi: [10.1016/j.epsl.2008.03.062](https://doi.org/10.1016/j.epsl.2008.03.062)
- Erkaev, N. V., Lammer, H., Odert, P., et al. 2016, EUV-driven mass-loss of protoplanetary cores with hydrogen-dominated atmospheres: the influences of ionization and orbital distance, *Monthly Notices of the Royal Astronomical Society*, 460, 1300, doi: [10.1093/mnras/stw935](https://doi.org/10.1093/mnras/stw935)
- Erkaev, N. V., Lammer, H., Odert, P., et al. 2013, XUV-Exposed, Non-Hydrostatic Hydrogen-Rich Upper Atmospheres of Terrestrial Planets. Part I: Atmospheric Expansion and Thermal Escape, *Astrobiology*, 13, 1011, doi: [10.1089/ast.2012.0957](https://doi.org/10.1089/ast.2012.0957)
- Fischer-Gödde, M., & Kleine, T. 2017, Ruthenium isotopic evidence for an inner Solar System origin of the late veneer, *Nature*, 541, 525, doi: [10.1038/nature21045](https://doi.org/10.1038/nature21045)
- Gaidos, E., Claytor, Z., Dungee, R., Ali, A., & Feiden, G. A. 2023, The TIME Table: rotation and ages of cool exoplanet host stars, *Monthly Notices of the Royal Astronomical Society*, 520, 5283, doi: [10.1093/mnras/stad343](https://doi.org/10.1093/mnras/stad343)

- Gao, P., & Powell, D. 2021, A Universal Cloud Composition on the Nightsides of Hot Jupiters, *The Astrophysical Journal Letters*, 918, L7, doi: [10.3847/2041-8213/ac139f](https://doi.org/10.3847/2041-8213/ac139f)
- Gao, P., Thorngren, D. P., Lee, E. K. H., et al. 2020, Aerosol composition of hot giant exoplanets dominated by silicates and hydrocarbon hazes, *Nature Astronomy*, 4, 951, doi: [10.1038/s41550-020-1114-3](https://doi.org/10.1038/s41550-020-1114-3)
- Gordon, S., & McBride, B. J. 1994, Computer program for calculation of complex chemical equilibrium compositions and applications. Part 1: Analysis., Tech. rep. <https://ntrs.nasa.gov/citations/19950013764>
- Gronoff, G., Arras, P., Baraka, S., et al. 2020, Atmospheric Escape Processes and Planetary Atmospheric Evolution, *Journal of Geophysical Research: Space Physics*, 125, e2019JA027639, doi: [10.1029/2019JA027639](https://doi.org/10.1029/2019JA027639)
- Gu, J. T., Peng, B., Ji, X., et al. 2024, Composition of Earth's initial atmosphere and fate of accreted volatiles set by core formation and magma ocean redox evolution, *Earth and Planetary Science Letters*, 629, 118618, doi: [10.1016/j.epsl.2024.118618](https://doi.org/10.1016/j.epsl.2024.118618)
- Guinan, E. F., Engle, S. G., & Durbin, A. 2016, LIVING WITH A RED DWARF: ROTATION AND X-RAY AND ULTRAVIOLET PROPERTIES OF THE HALO POPULATION KAPTEYN'S STAR\*, *The Astrophysical Journal*, 821, 81, doi: [10.3847/0004-637X/821/2/81](https://doi.org/10.3847/0004-637X/821/2/81)
- Halliday, A. N. 2013, The origins of volatiles in the terrestrial planets, *Geochimica et Cosmochimica Acta*, 105, 146, doi: [10.1016/j.gca.2012.11.015](https://doi.org/10.1016/j.gca.2012.11.015)
- Hasegawa, Y., & Swain, M. R. 2024, Bulk and Atmospheric Metallicities as Direct Probes of Sequentially Varying Accretion Mechanisms of Gas and Solids Onto Planets, *The Astrophysical Journal Letters*, 973, L46, doi: [10.3847/2041-8213/ad7957](https://doi.org/10.3847/2041-8213/ad7957)
- Hier-Majumder, S., & Hirschmann, M. M. 2017, The origin of volatiles in the Earth's mantle, *Geochemistry, Geophysics, Geosystems*, 18, 3078, doi: [10.1002/2017GC006937](https://doi.org/10.1002/2017GC006937)
- Hirschmann, M. M., Bergin, E. A., Blake, G. A., Ciesla, F. J., & Li, J. 2021, Early volatile depletion on planetesimals inferred from C-S systematics of iron meteorite parent bodies, *Proceedings of the National Academy of Sciences*, 118, e2026779118, doi: [10.1073/pnas.2026779118](https://doi.org/10.1073/pnas.2026779118)
- Ho, C. S. K., & Van Eylen, V. 2023, A deep radius valley revealed by *Kepler* short cadence observations, *Monthly Notices of the Royal Astronomical Society*, 519, 4056, doi: [10.1093/mnras/stac3802](https://doi.org/10.1093/mnras/stac3802)
- Hord, B. J., Kempton, E. M.-R., Evans-Soma, T. M., et al. 2024, Identification of the Top TESS Objects of Interest for Atmospheric Characterization of Transiting Exoplanets with JWST, *The Astronomical Journal*, 167, 233, doi: [10.3847/1538-3881/ad3068](https://doi.org/10.3847/1538-3881/ad3068)
- Hu, R., Bello-Arufe, A., Zhang, M., et al. 2024, A secondary atmosphere on the rocky exoplanet 55 Cancri e, *Nature*, 630, 609, doi: [10.1038/s41586-024-07432-x](https://doi.org/10.1038/s41586-024-07432-x)
- Ih, J., Kempton, E. M.-R., Whittaker, E. A., & Lessard, M. 2023, Constraining the thickness of TRAPPIST-1 b's atmosphere from its JWST secondary eclipse observation at 15  $\mu$ m, *The Astrophysical Journal Letters*, 952, L4
- Ito, Y., & Ikoma, M. 2021, Hydrodynamic escape of mineral atmosphere from hot rocky exoplanet. I. Model description, *Monthly Notices of the Royal Astronomical Society*, 502, 750, doi: [10.1093/mnras/staa3962](https://doi.org/10.1093/mnras/staa3962)
- Jackson, A. P., Davis, T. A., & Wheatley, P. J. 2012, The coronal X-ray-age relation and its implications for the evaporation of exoplanets: X-ray-age relation and exoplanet evaporation, *Monthly Notices of the Royal Astronomical Society*, 422, 2024, doi: [10.1111/j.1365-2966.2012.20657.x](https://doi.org/10.1111/j.1365-2966.2012.20657.x)
- Johansen, A., Ronnet, T., Schiller, M., Deng, Z., & Bizzarro, M. 2023, Anatomy of rocky planets formed by rapid pebble accretion: III. Partitioning of volatiles between planetary core, mantle, and atmosphere, *Astronomy & Astrophysics*, 671, A76, doi: [10.1051/0004-6361/202142143](https://doi.org/10.1051/0004-6361/202142143)
- Johnstone, C. P. 2020, Hydrodynamic Escape of Water Vapor Atmospheres near Very Active Stars, *The Astrophysical Journal*, 890, 79, doi: [10.3847/1538-4357/ab6224](https://doi.org/10.3847/1538-4357/ab6224)
- Johnstone, C. P., Bartel, M., & Güdel, M. 2021, The active lives of stars: a complete description of rotation and XUV evolution of F, G, K, and M dwarfs, *Astronomy & Astrophysics*, 649, A96, doi: [10.1051/0004-6361/202038407](https://doi.org/10.1051/0004-6361/202038407)
- Johnstone, C. P., Güdel, M., Lammer, H., & Kislyakova, K. G. 2018, Upper atmospheres of terrestrial planets: Carbon dioxide cooling and the Earth's thermospheric evolution, *Astronomy & Astrophysics*, 617, A107, doi: [10.1051/0004-6361/201832776](https://doi.org/10.1051/0004-6361/201832776)
- Jontof-Hutter, D. 2019, The Compositional Diversity of Low-Mass Exoplanets, *Annual Review of Earth and Planetary Sciences*, 47, 141, doi: [10.1146/annurev-earth-053018-060352](https://doi.org/10.1146/annurev-earth-053018-060352)

- Kegerreis, J. A., Eke, V. R., Catling, D. C., et al. 2020, Atmospheric Erosion by Giant Impacts onto Terrestrial Planets: A Scaling Law for any Speed, Angle, Mass, and Density, *The Astrophysical Journal*, 901, L31, doi: [10.3847/2041-8213/abb5fb](https://doi.org/10.3847/2041-8213/abb5fb)
- Kempton, E. M. R., Bean, J. L., Louie, D. R., et al. 2018, A Framework for Prioritizing the TESS Planetary Candidates Most Amenable to Atmospheric Characterization, *Publications of the Astronomical Society of the Pacific*, 130, 114401, doi: [10.1088/1538-3873/aad6f6](https://doi.org/10.1088/1538-3873/aad6f6)
- King, G. W., & Wheatley, P. J. 2020, EUV irradiation of exoplanet atmospheres occurs on Gyr time-scales, *Monthly Notices of the Royal Astronomical Society: Letters*, 501, L28, doi: [10.1093/mnras/501.1/laa186](https://doi.org/10.1093/mnras/501.1/laa186)
- King, G. W., Wheatley, P. J., Salz, M., et al. 2018, The XUV environments of exoplanets from Jupiter-size to super-Earth, *Monthly Notices of the Royal Astronomical Society*, doi: [10.1093/mnras/sty1110](https://doi.org/10.1093/mnras/sty1110)
- Kite, E. S., & Barnett, M. N. 2020, Exoplanet secondary atmosphere loss and revival, *Proceedings of the National Academy of Sciences*, 117, 18264, doi: [10.1073/pnas.2006177117](https://doi.org/10.1073/pnas.2006177117)
- Kite, E. S., & Schaefer, L. 2021, Water on Hot Rocky Exoplanets, *The Astrophysical Journal Letters*, 909, L22, doi: [10.3847/2041-8213/abe7dc](https://doi.org/10.3847/2041-8213/abe7dc)
- Koll, D. D. B., Malik, M., Mansfield, M., et al. 2019, Identifying Candidate Atmospheres on Rocky M Dwarf Planets via Eclipse Photometry, *ApJ*, 886, 140, doi: [10.3847/1538-4357/ab4c91](https://doi.org/10.3847/1538-4357/ab4c91)
- Kral, Q., Wyatt, M. C., Triaud, A. H. M. J., et al. 2018, Cometary impactors on the TRAPPIST-1 planets can destroy all planetary atmospheres and rebuild secondary atmospheres on planets f, g, and h, *Monthly Notices of the Royal Astronomical Society*, 479, 2649, doi: [10.1093/mnras/sty1677](https://doi.org/10.1093/mnras/sty1677)
- Krasnopolsky, V. A., Maillard, J. P., & Owen, T. C. 2004, Detection of methane in the martian atmosphere: evidence for life? *Icarus*, 172, 537, doi: [10.1016/j.icarus.2004.07.004](https://doi.org/10.1016/j.icarus.2004.07.004)
- Krissansen-Totton, J. 2023, Implications of Atmospheric Nondetections for Trappist-1 Inner Planets on Atmospheric Retention Prospects for Outer Planets, *The Astrophysical Journal Letters*, 951, L39, doi: [10.3847/2041-8213/acdc26](https://doi.org/10.3847/2041-8213/acdc26)
- Krissansen-Totton, J., Wogan, N., Thompson, M., & Fortney, J. J. 2024, The erosion of large primary atmospheres typically leaves behind substantial secondary atmospheres on temperate rocky planets, *Nature Communications*, 15, 8374, doi: [10.1038/s41467-024-52642-6](https://doi.org/10.1038/s41467-024-52642-6)
- Levine, W. G., Vissapragada, S., Feinstein, A. D., et al. 2024, Exoplanet Aeronomy: A Case Study of WASP-69b's Variable Thermosphere, *arXiv*, doi: [10.48550/ARXIV.2405.19177](https://doi.org/10.48550/ARXIV.2405.19177)
- Lichtenberg, T., Bower, D. J., Hammond, M., et al. 2021a, Vertically Resolved Magma Ocean–Protoatmosphere Evolution: H<sub>2</sub>, H<sub>2</sub>O, CO<sub>2</sub>, CH<sub>4</sub>, CO, O<sub>2</sub>, and N<sub>2</sub> as Primary Absorbers, *Journal of Geophysical Research: Planets*, 126, e2020JE006711, doi: [10.1029/2020JE006711](https://doi.org/10.1029/2020JE006711)
- Lichtenberg, T., Drażkowska, J., Schönbachler, M., Golabek, G. J., & Hands, T. O. 2021b, Bifurcation of planetary building blocks during Solar System formation, *Science*, 371, 365, doi: [10.1126/science.abb3091](https://doi.org/10.1126/science.abb3091)
- Lichtenberg, T., Golabek, G. J., Burn, R., et al. 2019, A water budget dichotomy of rocky protoplanets from 26Al-heating, *Nature Astronomy*, 3, 307, doi: [10.1038/s41550-018-0688-5](https://doi.org/10.1038/s41550-018-0688-5)
- Linssen, D., Shih, J., MacLeod, M., & Oklopčić, A. 2024, The open-source sunbather code: modeling escaping planetary atmospheres and their transit spectra, *arXiv*, <http://arxiv.org/abs/2404.12775>
- Liu, B., Johansen, A., Lambrechts, M., Bizzarro, M., & Haugbølle, T. 2022, Natural separation of two primordial planetary reservoirs in an expanding solar protoplanetary disk, *Science Advances*, 8, eabm3045, doi: [10.1126/sciadv.abm3045](https://doi.org/10.1126/sciadv.abm3045)
- Lock, S. J., & Stewart, S. T. 2017, The structure of terrestrial bodies: Impact heating, corotation limits, and synestias, *Journal of Geophysical Research: Planets*, 122, 950, doi: [10.1002/2016JE005239](https://doi.org/10.1002/2016JE005239)
- Looveren, G. V., Güdel, M., Saikia, S. B., & Kislyakova, K. 2024, Airy worlds or barren rocks? On the survivability of secondary atmospheres around the TRAPPIST-1 planets, *Astronomy & Astrophysics*, 683, A153, doi: [10.1051/0004-6361/202348079](https://doi.org/10.1051/0004-6361/202348079)
- Looveren, G. V., Saikia, S. B., Herbort, O., et al. 2025, Habitable Zone and Atmosphere Retention Distance (HaZARD) - Stellar-evolution-dependent loss models of secondary atmospheres, *Astronomy & Astrophysics*, 694, A310, doi: [10.1051/0004-6361/202452998](https://doi.org/10.1051/0004-6361/202452998)



- Lopez, E. D., & Fortney, J. J. 2014, UNDERSTANDING THE MASS–RADIUS RELATION FOR SUB-NEPTUNES: RADIUS AS A PROXY FOR COMPOSITION, *The Astrophysical Journal*, 792, 1, doi: [10.1088/0004-637X/792/1/1](https://doi.org/10.1088/0004-637X/792/1/1)
- Lopez, E. D., Fortney, J. J., & Miller, N. 2012, HOW THERMAL EVOLUTION AND MASS-LOSS SCULPT POPULATIONS OF SUPER-EARTHS AND SUB-NEPTUNES: APPLICATION TO THE KEPLER-11 SYSTEM AND BEYOND, *The Astrophysical Journal*, 761, 59, doi: [10.1088/0004-637X/761/1/59](https://doi.org/10.1088/0004-637X/761/1/59)
- Luque, R., & Pallé, E. 2022, Density, not radius, separates rocky and water-rich small planets orbiting M dwarf stars, *Science*, 377, 1211, doi: [10.1126/science.abl7164](https://doi.org/10.1126/science.abl7164)
- Madhusudhan, N., Sarkar, S., Constantinou, S., et al. 2023, Carbon-bearing Molecules in a Possible Hycean Atmosphere, *The Astrophysical Journal*, 956, L13, doi: [10.3847/2041-8213/acf577](https://doi.org/10.3847/2041-8213/acf577)
- Malamud, U., Podolak, M., Podolak, J. I., & Bodenheimer, P. H. 2024, Uranus and Neptune as methane planets: Producing icy giants from refractory planetesimals, *Icarus*, 421, 116217, doi: [10.1016/j.icarus.2024.116217](https://doi.org/10.1016/j.icarus.2024.116217)
- Mansfield, M., Kite, E. S., Hu, R., et al. 2019, Identifying Atmospheres on Rocky Exoplanets through Inferred High Albedo, *ApJ*, 886, 141, doi: [10.3847/1538-4357/ab4c90](https://doi.org/10.3847/1538-4357/ab4c90)
- Marty, B., & Zimmermann, L. 1999, Volatiles (He, C, N, Ar) in mid-ocean ridge basalts: assesment of shallow-level fractionation and characterization of source composition, *Geochimica et Cosmochimica Acta*, 63, 3619, doi: [10.1016/S0016-7037\(99\)00169-6](https://doi.org/10.1016/S0016-7037(99)00169-6)
- Monaghan, C., Roy, P.-A., Benneke, B., et al. 2025, Low 4.5  $\mu$  m Dayside Emission Disfavors a Dark Bare-Rock scenario for the Hot Super-Earth TOI-431 b, *arXiv preprint arXiv:2503.09698*
- Moore, K., David, B., Zhang, A. Y., & Cowan, N. B. 2024, Water Evolution and Inventories of Super-Earths Orbiting Late M Dwarfs, *The Astrophysical Journal*, 972, 131, doi: [10.3847/1538-4357/ad6444](https://doi.org/10.3847/1538-4357/ad6444)
- Murray-Clay, R. A., Chiang, E. I., & Murray, N. 2009, Atmospheric Escape From Hot Jupiters, *The Astrophysical Journal*, 693, 23, doi: [10.1088/0004-637X/693/1/23](https://doi.org/10.1088/0004-637X/693/1/23)
- Nakayama, A., Ikoma, M., & Terada, N. 2022, Survival of Terrestrial N<sub>2</sub>–O<sub>2</sub> Atmospheres in Violent XUV Environments through Efficient Atomic Line Radiative Cooling, *The Astrophysical Journal*, 937, 72, doi: [10.3847/1538-4357/ac86ca](https://doi.org/10.3847/1538-4357/ac86ca)
- Owen, J. E. 2019, Atmospheric Escape and the Evolution of Close-In Exoplanets, *Annual Review of Earth and Planetary Sciences*, 47, 67, doi: [10.1146/annurev-earth-053018-060246](https://doi.org/10.1146/annurev-earth-053018-060246)
- Owen, J. E., & Schlichting, H. E. 2024, Mapping out the parameter space for photoevaporation and core-powered mass-loss, *Monthly Notices of the Royal Astronomical Society*, 528, 1615, doi: [10.1093/mnras/stad3972](https://doi.org/10.1093/mnras/stad3972)
- Owen, J. E., & Wu, Y. 2016, ATMOSPHERES OF LOW-MASS PLANETS: THE “BOIL-OFF”, *The Astrophysical Journal*, 817, 107, doi: [10.3847/0004-637X/817/2/107](https://doi.org/10.3847/0004-637X/817/2/107)
- Paragas, K., Knutson, H. A., Hu, R., et al. 2025, A New Spectral Library for Modeling the Surfaces of Hot, Rocky Exoplanets, *The Astrophysical Journal*, 981, 130
- Patel, J. A., Brandeker, A., Kitzmann, D., et al. 2024, JWST reveals the rapid and strong day-side variability of 55 Cancri e, *Astronomy & Astrophysics*, 690, A159, doi: [10.1051/0004-6361/202450748](https://doi.org/10.1051/0004-6361/202450748)
- Peng, B., & Valencia, D. 2024, Puffy Venuses: The Mass–Radius Impact of Carbon-rich Atmospheres on Lava Worlds, *The Astrophysical Journal*, 976, 202, doi: [10.3847/1538-4357/ad6f03](https://doi.org/10.3847/1538-4357/ad6f03)
- Penz, T., Micela, G., & Lammer, H. 2008, Influence of the evolving stellar X-ray luminosity distribution on exoplanetary mass loss, *Astronomy and Astrophysics*, 477, 309, doi: [10.1051/0004-6361:20078364](https://doi.org/10.1051/0004-6361:20078364)
- Piette, A. A. A., Gao, P., Brugman, K., et al. 2023, Rocky Planet or Water World? Observability of Low-density Lava World Atmospheres, *The Astrophysical Journal*, 954, 29, doi: [10.3847/1538-4357/acdef2](https://doi.org/10.3847/1538-4357/acdef2)
- Preibisch, T., & Feigelson, E. D. 2005, The Evolution of X-Ray Emission in Young Stars, *The Astrophysical Journal Supplement Series*, 160, 390, doi: [10.1086/432094](https://doi.org/10.1086/432094)
- Raymond, S. N., Quinn, T., & Lunine, J. I. 2004, Making other earths: dynamical simulations of terrestrial planet formation and water delivery, *Icarus*, 168, 1, doi: [10.1016/j.icarus.2003.11.019](https://doi.org/10.1016/j.icarus.2003.11.019)
- Redfield, S., Batalha, N., Benneke, B., et al. 2024, Report of the Working Group on Strategic Exoplanet Initiatives with HST and JWST, *arXiv*, doi: [10.48550/arXiv.2404.02932](https://doi.org/10.48550/arXiv.2404.02932)
- Reynard, B., & Sotin, C. 2023, Carbon-rich icy moons and dwarf planets, *Earth and Planetary Science Letters*, 612, 118172, doi: [10.1016/j.epsl.2023.118172](https://doi.org/10.1016/j.epsl.2023.118172)
- Ribas, I., Guinan, E. F., Gudel, M., & Audard, M. 2005, Evolution of the Solar Activity over Time and Effects on Planetary Atmospheres. I. High-Energy Irradiances (1–1700 Å), *The Astrophysical Journal*, 622, 680, doi: [10.1086/427977](https://doi.org/10.1086/427977)



- Ribas, I., Bolmont, E., Selsis, F., et al. 2016, The habitability of Proxima Centauri b: I. Irradiation, rotation and volatile inventory from formation to the present, *Astronomy & Astrophysics*, 596, A111, doi: [10.1051/0004-6361/201629576](https://doi.org/10.1051/0004-6361/201629576)
- Righter, K., & O'Brien, D. P. 2011, Terrestrial planet formation, *Proceedings of the National Academy of Sciences*, 108, 19165, doi: [10.1073/pnas.1013480108](https://doi.org/10.1073/pnas.1013480108)
- Rogers, L. A. 2015, MOST 1.6 EARTH-RADIUS PLANETS ARE NOT ROCKY, *The Astrophysical Journal*, 801, 41, doi: [10.1088/0004-637X/801/1/41](https://doi.org/10.1088/0004-637X/801/1/41)
- Rogers, L. A., & Seager, S. 2010, A FRAMEWORK FOR QUANTIFYING THE DEGENERACIES OF EXOPLANET INTERIOR COMPOSITIONS, *The Astrophysical Journal*, 712, 974, doi: [10.1088/0004-637X/712/2/974](https://doi.org/10.1088/0004-637X/712/2/974)
- Rosener, R., Zhang, M., & Bean, J. L. 2025, Detectability of Emission from Exoplanet Outflows Calculated by pyTPCI, a New 1D Radiation-Hydrodynamic Code, doi: [10.3847/1538-4357/ada6ab](https://doi.org/10.3847/1538-4357/ada6ab)
- Rubie, D. C., Jacobson, S. A., Morbidelli, A., et al. 2015, Accretion and differentiation of the terrestrial planets with implications for the compositions of early-formed Solar System bodies and accretion of water, *Icarus*, 248, 89, doi: [10.1016/j.icarus.2014.10.015](https://doi.org/10.1016/j.icarus.2014.10.015)
- Sakuraba, H., Kurokawa, H., Genda, H., & Ohta, K. 2021, Numerous chondritic impactors and oxidized magma ocean set Earth's volatile depletion, *Scientific Reports*, 11, 20894, doi: [10.1038/s41598-021-99240-w](https://doi.org/10.1038/s41598-021-99240-w)
- Schaefer, L., Wordsworth, R. D., Berta-Thompson, Z., & Sasselov, D. 2016, PREDICTIONS OF THE ATMOSPHERIC COMPOSITION OF GJ 1132b, *The Astrophysical Journal*, 829, 63, doi: [10.3847/0004-637X/829/2/63](https://doi.org/10.3847/0004-637X/829/2/63)
- Schlichting, H. E., & Mukhopadhyay, S. 2018, Atmosphere Impact Losses, *Space Science Reviews*, 214, 34, doi: [10.1007/s11214-018-0471-z](https://doi.org/10.1007/s11214-018-0471-z)
- Selsis, F., Kasting, J. F., Levrard, B., et al. 2007, Habitable planets around the star Gl 581? *Astronomy & Astrophysics*, 476, 1373, doi: [10.1051/0004-6361:20078091](https://doi.org/10.1051/0004-6361:20078091)
- Selsis, F., Leconte, J., Turbet, M., Chaverot, G., & Bolmont, 2023, A cool runaway greenhouse without surface magma ocean, *Nature*, 620, 287, doi: [10.1038/s41586-023-06258-3](https://doi.org/10.1038/s41586-023-06258-3)
- Sinclair, C. A., Wyatt, M. C., Morbidelli, A., & Nesvorný, D. 2020, Evolution of the Earth's atmosphere during Late Veneer accretion, *Monthly Notices of the Royal Astronomical Society*, 499, 5334, doi: [10.1093/mnras/staa3210](https://doi.org/10.1093/mnras/staa3210)
- Sossi, P. A. 2021, Atmospheres in the baking, *Nature Astronomy*, 5, 535, doi: [10.1038/s41550-021-01353-9](https://doi.org/10.1038/s41550-021-01353-9)
- Stafne, E., & Becker, J. 2024, Predicting CO2 Gas Layer Thickness due to Mantle Outgassing in the Exoplanet Census, *Research Notes of the AAS*, 8, 176, doi: [10.3847/2515-5172/ad5f30](https://doi.org/10.3847/2515-5172/ad5f30)
- Swastik, C., Banyal, R. K., Narang, M., et al. 2023, Age Distribution of Exoplanet Host Stars: Chemical and Kinematic Age Proxies from GAIA DR3, *The Astronomical Journal*, 166, 91, doi: [10.3847/1538-3881/ace782](https://doi.org/10.3847/1538-3881/ace782)
- Tian, F. 2009, THERMAL ESCAPE FROM SUPER EARTH ATMOSPHERES IN THE HABITABLE ZONES OF M STARS, *The Astrophysical Journal*, 703, 905, doi: [10.1088/0004-637X/703/1/905](https://doi.org/10.1088/0004-637X/703/1/905)
- Tian, F. 2015a, History of water loss and atmospheric O2 buildup on rocky exoplanets near M dwarfs, *Earth and Planetary Science Letters*, 432, 126, doi: [10.1016/j.epsl.2015.09.051](https://doi.org/10.1016/j.epsl.2015.09.051)
- Tian, F. 2015b, Atmospheric Escape from Solar System Terrestrial Planets and Exoplanets, *Annual Review of Earth and Planetary Sciences*, 43, 459, doi: [10.1146/annurev-earth-060313-054834](https://doi.org/10.1146/annurev-earth-060313-054834)
- Tian, F., & Ida, S. 2015, Water contents of Earth-mass planets around M dwarfs, *Nature Geoscience*, 8, 177, doi: [10.1038/ngeo2372](https://doi.org/10.1038/ngeo2372)
- Tian, F., Kasting, J. F., Liu, H.-L., & Roble, R. G. 2008, Hydrodynamic planetary thermosphere model: 1. Response of the Earth's thermosphere to extreme solar EUV conditions and the significance of adiabatic cooling, *Journal of Geophysical Research: Planets*, 113, doi: [10.1029/2007JE002946](https://doi.org/10.1029/2007JE002946)
- Tian, F., Kasting, J. F., & Solomon, S. C. 2009, Thermal escape of carbon from the early Martian atmosphere, *Geophysical Research Letters*, 36, 2008GL036513, doi: [10.1029/2008GL036513](https://doi.org/10.1029/2008GL036513)
- Tognelli, E., Prada Moroni, P. G., & Degl'Innocenti, S. 2018, Theoretical uncertainties on the radius of low- and very-low-mass stars, *Monthly Notices of the Royal Astronomical Society*, 476, 27, doi: [10.1093/mnras/sty195](https://doi.org/10.1093/mnras/sty195)
- Tu, L., Johnstone, C. P., Güdel, M., & Lammer, H. 2015, The extreme ultraviolet and X-ray Sun in Time: High-energy evolutionary tracks of a solar-like star, *Astronomy & Astrophysics*, 577, L3, doi: [10.1051/0004-6361/201526146](https://doi.org/10.1051/0004-6361/201526146)
- Valencia, D., Sasselov, D. D., & O'Connell, R. J. 2007, Detailed Models of Super-Earths: How Well Can We Infer Bulk Properties? *The Astrophysical Journal*, 665, 1413, doi: [10.1086/519554](https://doi.org/10.1086/519554)

- Vilhu, O. 1984, The nature of magnetic activity in lower main sequence stars., *Astronomy and Astrophysics*, 133, 117.  
<https://ui.adsabs.harvard.edu/abs/1984A&A...133..117V>
- Wagner, W. 1988, Observations of 1–8 Å solar X-ray variability during solar cycle 21, *Advances in Space Research*, 8, 67, doi: [10.1016/0273-1177\(88\)90173-1](https://doi.org/10.1016/0273-1177(88)90173-1)
- Watson, A. J., Donahue, T. M., & Walker, J. C. 1981, The dynamics of a rapidly escaping atmosphere: Applications to the evolution of Earth and Venus, *Icarus*, 48, 150, doi: [10.1016/0019-1035\(81\)90101-9](https://doi.org/10.1016/0019-1035(81)90101-9)
- Wood, B. E., Müller, H.-R., Redfield, S., et al. 2021, New Observational Constraints on the Winds of M dwarf Stars\*, *The Astrophysical Journal*, 915, 37, doi: [10.3847/1538-4357/abfda5](https://doi.org/10.3847/1538-4357/abfda5)
- Wordsworth, R., & Kreidberg, L. 2022, Atmospheres of Rocky Exoplanets, *Annual Review of Astronomy and Astrophysics*, 60, 159, doi: [10.1146/annurev-astro-052920-125632](https://doi.org/10.1146/annurev-astro-052920-125632)
- Wordsworth, R. D. 2016, Atmospheric nitrogen evolution on Earth and Venus, *Earth and Planetary Science Letters*, 447, 103, doi: [10.1016/j.epsl.2016.04.002](https://doi.org/10.1016/j.epsl.2016.04.002)
- Wordsworth, R. D., Schaefer, L. K., & Fischer, R. A. 2018, Redox Evolution via Gravitational Differentiation on Low-mass Planets: Implications for Abiotic Oxygen, Water Loss, and Habitability, *The Astronomical Journal*, 155, 195, doi: [10.3847/1538-3881/aab608](https://doi.org/10.3847/1538-3881/aab608)
- Wyatt, M. C., Kral, Q., & Sinclair, C. A. 2020, Susceptibility of planetary atmospheres to mass-loss and growth by planetesimal impacts: the impact shoreline, *Monthly Notices of the Royal Astronomical Society*, 491, 782, doi: [10.1093/mnras/stz3052](https://doi.org/10.1093/mnras/stz3052)
- Xu, S., & Bonsor, A. 2021, Exogeology from Polluted White Dwarfs, *arXiv*, doi: [10.48550/arXiv.2108.08384](https://doi.org/10.48550/arXiv.2108.08384)
- Yoshida, T., & Kuramoto, K. 2020, Sluggish hydrodynamic escape of early martian atmosphere with reduced chemical compositions, *Icarus*, 345, 113740, doi: [10.1016/j.icarus.2020.113740](https://doi.org/10.1016/j.icarus.2020.113740)
- Yoshida, T., Terada, N., Ikoma, M., & Kuramoto, K. 2022, Less Effective Hydrodynamic Escape of H<sub>2</sub>–H<sub>2</sub>O Atmospheres on Terrestrial Planets Orbiting Pre-main-sequence M Dwarfs, *The Astrophysical Journal*, 934, 137, doi: [10.3847/1538-4357/ac7be7](https://doi.org/10.3847/1538-4357/ac7be7)
- Yoshida, T., Terada, N., & Kuramoto, K. 2024, Suppression of hydrodynamic escape of an H<sub>2</sub>-rich early Earth atmosphere by radiative cooling of carbon oxides, *Progress in Earth and Planetary Science*, 11, 59, doi: [10.1186/s40645-024-00666-3](https://doi.org/10.1186/s40645-024-00666-3)
- Zahnle, K. J., & Catling, D. C. 2017, The Cosmic Shoreline: The Evidence that Escape Determines which Planets Have Atmospheres, and what this May Mean for Proxima Centauri B, *The Astrophysical Journal*, 843, 122, doi: [10.3847/1538-4357/aa7846](https://doi.org/10.3847/1538-4357/aa7846)
- Zeng, L., Jacobsen, S. B., Sasselov, D. D., et al. 2019, Growth model interpretation of planet size distribution, *Proceedings of the National Academy of Sciences*, 116, 9723, doi: [10.1073/pnas.1812905116](https://doi.org/10.1073/pnas.1812905116)
- Zhang, M., Cauley, P. W., Knutson, H. A., et al. 2022a, More Evidence for Variable Helium Absorption from HD 189733b, *The Astronomical Journal*, 164, 237, doi: [10.3847/1538-3881/ac9675](https://doi.org/10.3847/1538-3881/ac9675)
- Zhang, M., Dai, F., Bean, J. L., Knutson, H. A., & Rescigno, F. 2023, Outflowing Helium from a Mature Mini-Neptune, *The Astrophysical Journal*, 953, L25, doi: [10.3847/2041-8213/aced51](https://doi.org/10.3847/2041-8213/aced51)
- Zhang, M., Knutson, H. A., Wang, L., Dai, F., & Barragán, O. 2022b, Escaping Helium from TOI 560.01, a Young Mini-Neptune, *The Astronomical Journal*, 163, 67, doi: [10.3847/1538-3881/ac3fa7](https://doi.org/10.3847/1538-3881/ac3fa7)
- Zhang, M., Bean, J. L., Wilson, D., et al. 2024, Constraining atmospheric composition from the outflow: helium observations reveal the fundamental properties of two planets straddling the radius gap, *arXiv*, doi: [10.48550/ARXIV.2409.08318](https://doi.org/10.48550/ARXIV.2409.08318)

## APPENDIX

## A. CARBON DISTRIBUTION DURING MAGMA OCEAN SOLIDIFICATION

We distribute volatile between the magma, single-species atmosphere, and mantle reservoirs during magma ocean solidification as follows.

For nitrogen-rich cases, owing to the extremely low solubility of  $N_2$  in solids, the mass of nitrogen in the residual mantle can be neglected (S. Hier-Majumder & M. M. Hirschmann 2017).

For carbon-rich cases, we assume that as the magma cools and crystallizes, the atmosphere remains in equilibrium with the magma ocean surface according to the solubility law (T. Lichtenberg et al. 2021a). Additionally, we assume that the initial mass of the magma ocean is 2/3 of the planetary mass, and we only consider the carbon distributed between magma and atmosphere but neglect the partition into Fe-alloy core (I. Blanchard et al. 2022). The carbon mass distribution is calculated as a function of the changing magma mass during crystallization. As the magma mass decreases, carbon is redistributed between the atmosphere, magma ocean, and solid mantle.

## VARIABLES AND CONSTANTS

The key variables used in our model include  $C_{\text{atm}}$ ,  $C_{\text{magma}}$ , and  $C_{\text{mantle}}$ , which represent the carbon mass in the atmosphere, magma, and mantle, respectively, with the total carbon mass  $C_0$  remaining constant. The magma ocean mass is denoted as  $M_{\text{magma}}$ , and the carbon concentration in the magma is given by  $f = C_{\text{magma}}/M_{\text{magma}}$ . The partition coefficient for mantle-magma exchange is represented by  $D_{\text{mm}}$  (assumed constant). The solubility law linking surface pressure to carbon concentration in magma is parameterized by the constants  $\alpha$  and  $\beta$ , following T. Lichtenberg et al. (2021a), such that  $P_{\text{surf}} = (f/\alpha)^\beta$ . To simplify calculations, we define a factor  $k_{Ps} = \frac{12}{\text{MMW}} \cdot \frac{4\pi R_p^2}{g}$ , where  $R_p$  is the planetary radius,  $g$  is the gravitational acceleration, and the 12/MMW factor accounts for the mean molecular ratio of carbon to atmospheric species. MMW=44 for  $\text{CO}_2$  and MMW=16 for  $\text{CH}_4$ . This allows the atmospheric carbon mass to be expressed as  $C_{\text{atm}} = k_{Ps} \cdot P_{\text{surf}}$ .

## GOVERNING EQUATIONS

## 1. Mass Conservation:

$$C_{\text{atm}} + C_{\text{magma}} + C_{\text{mantle}} = C_0 \quad (\text{A1})$$

## 2. Carbon in atmosphere T. Lichtenberg et al. (2021a):

$$C_{\text{atm}} = k_{Ps} \left( \frac{f}{\alpha} \right)^\beta \quad (\text{A2})$$

This equation reflects the equilibrium between the atmospheric carbon and the carbon dissolved in the magma ocean surface. For  $\text{CO}_2$ ,  $\alpha = 1.937 \times 10^{-15} \text{Pa}^{-1}$ ;  $\beta = 0.714$ , and for  $\text{CH}_4$ ,  $\alpha = 9.937 \times 10^{-14} \text{Pa}^{-1}$ ;  $\beta = 1.000$  (T. Lichtenberg et al. 2021a)

## 3. Carbon in Magma:

$$C_{\text{magma}} = f M_{\text{magma}} \quad (\text{A3})$$

## 4. Mantle Carbon Change:

$$dC_{\text{mantle}} = -D_{\text{mm}} f dM_{\text{magma}} \quad (\text{A4})$$

This equation accounts for the partition of carbon from the magma into the solid mantle during solidification, with  $D_{\text{mm}}$  representing the partitioning behavior.

## DERIVATION OF THE DIFFERENTIAL EQUATION

Starting from the mass conservation equation A1, differentiating both sides and rearranging:

$$dC_{\text{mantle}} = -dC_{\text{atm}} - dC_{\text{magma}} \quad (\text{A5})$$

Differentiating equation A3:

$$dC_{\text{magma}} = f \cdot dM_{\text{magma}} + dM_{\text{magma}} \cdot df \quad (\text{A6})$$

From equation A2, express  $C_{\text{atm}}$  and differentiate:

$$dC_{\text{atm}} = k_{Ps} \alpha^{-\beta} \beta f^{\beta-1} df \quad (\text{A7})$$

Define a constant for simplification  $A = k_{Ps} \alpha^{-\beta} \beta$

Substitute equations A6 and A7 into equation A5:

$$f(D_{\text{mm}} + 1) dM_{\text{magma}} + (M_{\text{magma}} + A f^{\beta-1}) df = 0 \quad (\text{A8})$$

### SOLVING ODE

Let's consider  $M_{\text{magma}}$  as a function of  $f$ :

$$\frac{dM_{\text{magma}}}{df} = -\frac{M_{\text{magma}}}{f(D_{\text{mm}} + 1)} - \frac{A f^{\beta-2}}{(D_{\text{mm}} + 1)} \quad (\text{A9})$$

The ODE has the standard linear form  $\frac{dM_{\text{magma}}}{df} + P(f)M_{\text{magma}} = Q(f)$ , where  $P(f) = \frac{1}{f(D_{\text{mm}} + 1)}$  and  $Q(f) = -\frac{A f^{\beta-2}}{D_{\text{mm}} + 1}$ . The integrating factor  $\mu(f)$  is:

$$\mu(f) = \exp\left(\int P(f) df\right) = \exp\left(\int \frac{1}{f(D_{\text{mm}} + 1)} df\right) = f^{\frac{1}{D_{\text{mm}} + 1}} \quad (\text{A10})$$

Multiply both sides by the integrating factor and simplify:

$$\frac{d}{df} \left( f^{\frac{1}{D_{\text{mm}} + 1}} M_{\text{magma}} \right) = -\frac{A f^{\beta-2 + \frac{1}{D_{\text{mm}} + 1}}}{D_{\text{mm}} + 1} \quad (\text{A11})$$

Integrate with respect to  $f$  and let  $n = \beta - 2 + \frac{1}{D_{\text{mm}} + 1}$  for simplification:

$$f^{\frac{1}{D_{\text{mm}} + 1}} M_{\text{magma}} = -\frac{A}{(D_{\text{mm}} + 1)(n + 1)} f^{n+1} + \text{const} \quad (\text{A12})$$

where the integral constant (const) can be solved by the assumed initial condition.

### INTEGRAL CONSTANT DETERMINED BY INITIAL CONDITION

We assume the initial magma mass is  $M_{\text{magma},0} = 2/3 M_p$ , and the carbon is only distributed between magma and the atmosphere. With the solubility law, we can write down the mass conservation equation as:

$$C_0 = C_{\text{atm},0} + C_{\text{magma},0} = k_{Ps} \left( \frac{f_0}{\alpha} \right)^\beta + f_0 M_{\text{magma},0} \quad (\text{A13})$$

The equation can be solved numerically with the given total carbon mass  $C_0$ . And plug it back into equation A12, we can get the value of const.

Rearrange equation A12, the final expression of  $M_{\text{magma}}$  in terms of  $f$  is:

$$M_{\text{magma}} = \frac{A f^{\beta-1}}{(D_{\text{mm}} - 1) \left( \beta - 1 + \frac{1}{1 - D_{\text{mm}}} \right)} + \text{const} f^{-\frac{1}{1 - D_{\text{mm}}}} \quad (\text{A14})$$

Where:

- $A = \frac{12}{\text{MMW}} \cdot \frac{4\pi R_p^2}{g} \cdot \beta \alpha^{-\beta}$
- $\text{const} = f_0^{\frac{1}{D_{\text{mm}} + 1}} M_{\text{magma},0} + \frac{A}{(D_{\text{mm}} + 1)(n + 1)} f_0^{n+1}$

We have derived the differential equation considering how carbon partition into the solid mantle with the solidification of magma ocean  $dC_{\text{mantle}} = -f D_{\text{mm}} dM_{\text{magma}}$  and solved it to find how  $M_{\text{magma}}$  evolves with  $f$ . Using this solution, we can determine the evolution of all other variables with a given  $M_{\text{magma}}$ .

When setting  $M_{\text{magma}} = 0$ , that is the phase after fully solidification of the primordial magma ocean. And we show the distribution of carbon in different reservoirs in Fig. A1.

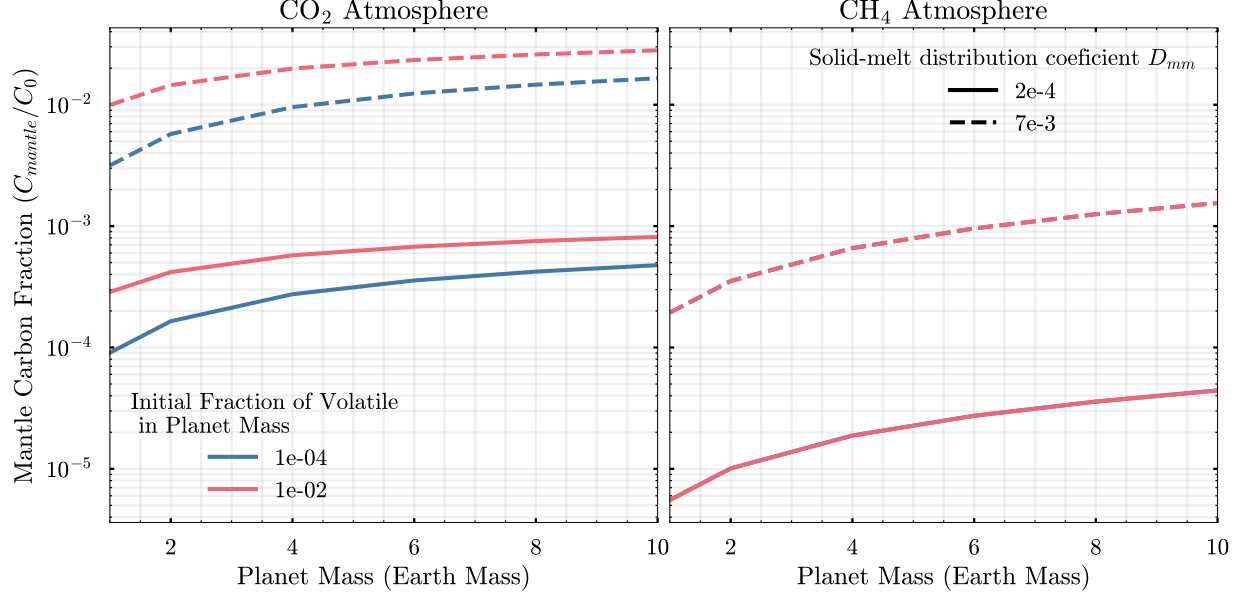


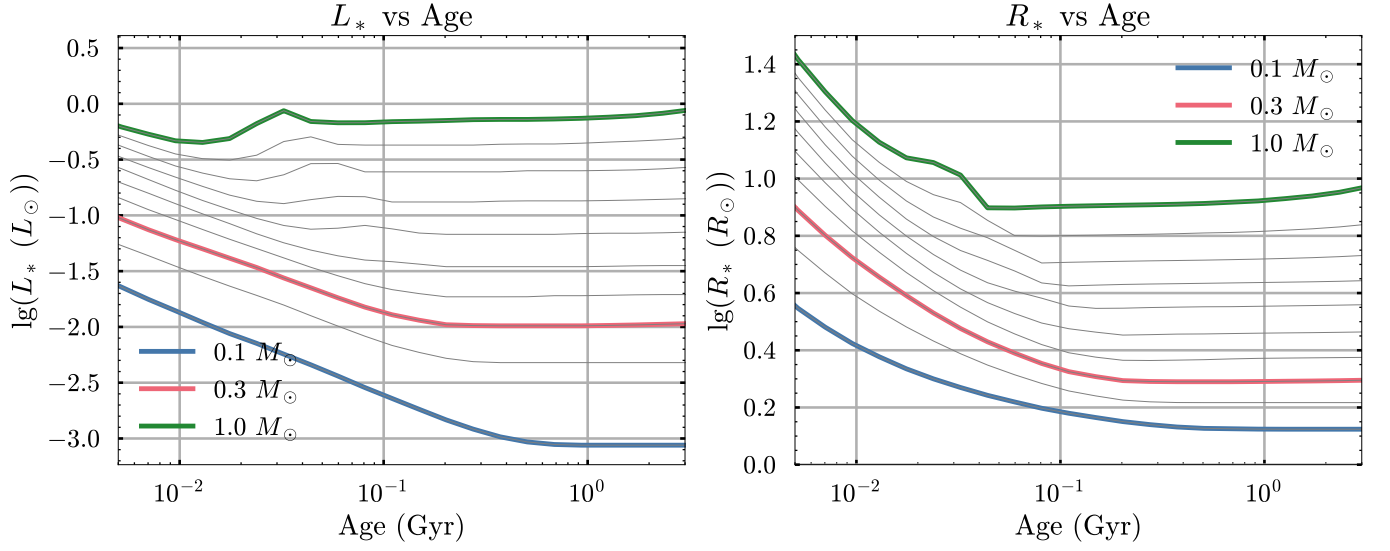
**Figure A1:** The fraction of carbon sequestered in the mantle relative to the total carbon mass after complete magma ocean solidification, shown as a function of planetary mass, for a pure-CO<sub>2</sub> atmosphere (left) and a pure-CH<sub>4</sub> atmosphere (right). The fraction increases with planetary mass due to the solubility law, which governs surface pressure, and the reduced atmospheric column mass at higher gravity with a given surface pressure. The blue line represents the lowest initial carbon case in our study, where the carbon-to-planetary mass ratio is  $10^{-4} M_p$ , while the pink line corresponds to the most carbon-rich case,  $10^{-2} M_p$ . A higher initial carbon concentration in the magma ocean results in more carbon being retained in the mantle post-solidification. Solid lines indicate a conservative solid-melt partition coefficient, while dashed lines represent a higher partition coefficient, following [L. Elkins-Tanton \(2008\)](#).



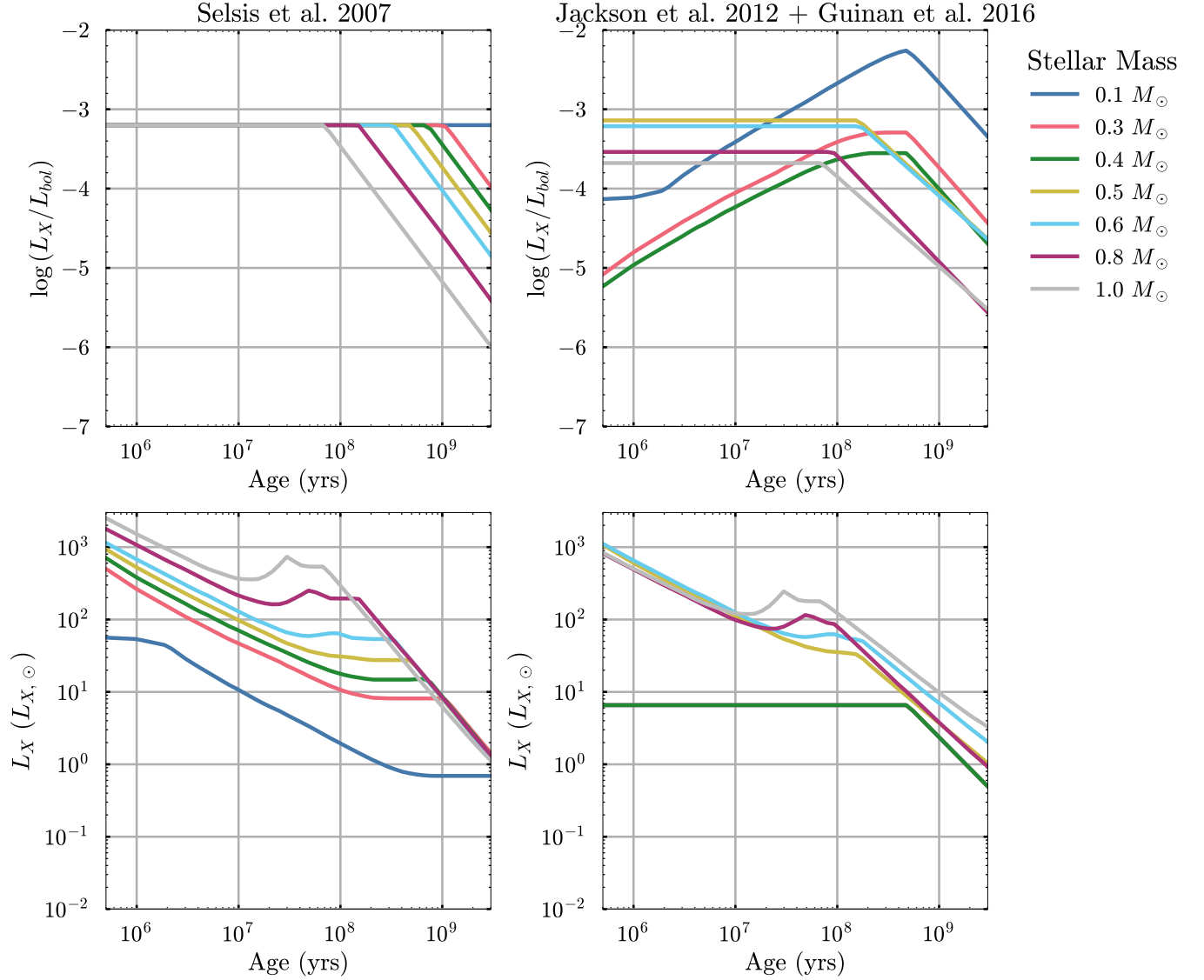
B. APPENDIX FIGURES

	Assumptions	
CO <sub>2</sub> (Thermal)	F. Tian et al. (2009), F. Tian (2009)	a. Neutral & Ion species included b. Jeans escape (hydrodynamic thermosphere) c. Heating: Collisions, chemical reactions, photoelectrons, radiative line heating d. Cooling: Recombination, molecular, Ly- $\alpha$ , and atomic oxygen 63 $\mu$ m emission
	1. Stellar bolometric luminosity: I. Baraffe et al. (2015) (no uncertainties included)	
	2. X-ray flux: A. P. Jackson et al. (2012) or F. Selsis et al. (2007)	
	3. EUV-to-X-ray ratio and uncertainties: G. W. King & P. J. Wheatley (2020)	
CO <sub>2</sub> (Non-Thermal)	L. Chin et al. (2024)	a. 3D Block-Adaptive-Tree Solar Wind Roe-type Upwind Scheme (BATS-R-US) b. Multispecies magnetohydrodynamic (MS-MHD) model c. Ion species: H <sup>+</sup> , O <sup>+</sup> , O <sub>2</sub> <sup>+</sup> , CO <sub>2</sub> <sup>+</sup> and ionospheric photochemistry d. Unmagnetized planets assumed
	1. Stellar bolometric luminosity: I. Baraffe et al. (2015) (no uncertainties included)	
	2. X-ray flux: A. P. Jackson et al. (2012) or F. Selsis et al. (2007)	
	3. Stellar mass loss rate scaled to X-ray: B. E. Wood et al. (2021) (no uncertainties included)	
H <sub>2</sub> O (Thermal)	C. P. Johnstone (2020)	a. Neutral & Ion species included b. Transonic hydrodynamic c. Heating: Collisions, ~500 chemical reactions, photoelectrons, radiative line heating d. Cooling: Recombination, molecular, Ly- $\alpha$ , and atomic oxygen 63 $\mu$ m emission
	1. Stellar bolometric luminosity: I. Baraffe et al. (2015) (no uncertainties included)	
	2. X-ray flux: A. P. Jackson et al. (2012) or F. Selsis et al. (2007)	
	3. EUV-to-X-ray ratio and uncertainties: G. W. King & P. J. Wheatley (2020)	
N <sub>2</sub> /O <sub>2</sub> (N22) (Thermal)	A. Nakayama et al. (2022)	a. Neutral & Ion species included b. Jeans escape (hydrodynamic thermosphere) c. Heating: Collisions, ~500 chemical reactions, photoelectrons, radiative line heating d. Cooling: Recombination, molecular, <b>atomic line cooling of N, C, and O</b>
	1. Stellar bolometric luminosity: I. Baraffe et al. (2015) (no uncertainties included)	
	2. X-ray flux: A. P. Jackson et al. (2012) or F. Selsis et al. (2007)	
	3. EUV-to-X-ray ratio and uncertainties: G. W. King & P. J. Wheatley (2020)	
N <sub>2</sub> /O <sub>2</sub> (C24) (Thermal)	R. D. Chatterjee & R. T. Pierrehumbert (2024)	a. Neutral & Ion species + <b>Ambipolar motion</b> b. Analytic approximations to transonic hydrodynamic and hydrostatic escape b. Heating: Parameterized c. Cooling: Recombination, <b>atomic line cooling of N and O</b> d. Introduces a new regime of global ion outflow controlled by a collisional-radiative thermostat
	1. Stellar bolometric luminosity: I. Baraffe et al. (2015) (no uncertainties included)	
	2. X-ray flux: A. P. Jackson et al. (2012) or F. Selsis et al. (2007)	
	3. EUV-to-X-ray ratio and uncertainties: G. W. King & P. J. Wheatley (2020)	
CH <sub>4</sub>	Energy-Limited Estimate	a. All uncertainties included in escape efficiency factor $\epsilon$ ( $0.05 < \epsilon < 0.5$ )
	1. Stellar bolometric luminosity: I. Baraffe et al. (2015) (no uncertainties included)	
	2. X-ray flux: A. P. Jackson et al. (2012) or F. Selsis et al. (2007)	
	3. EUV-to-X-ray ratio and uncertainties: G. W. King & P. J. Wheatley (2020)	

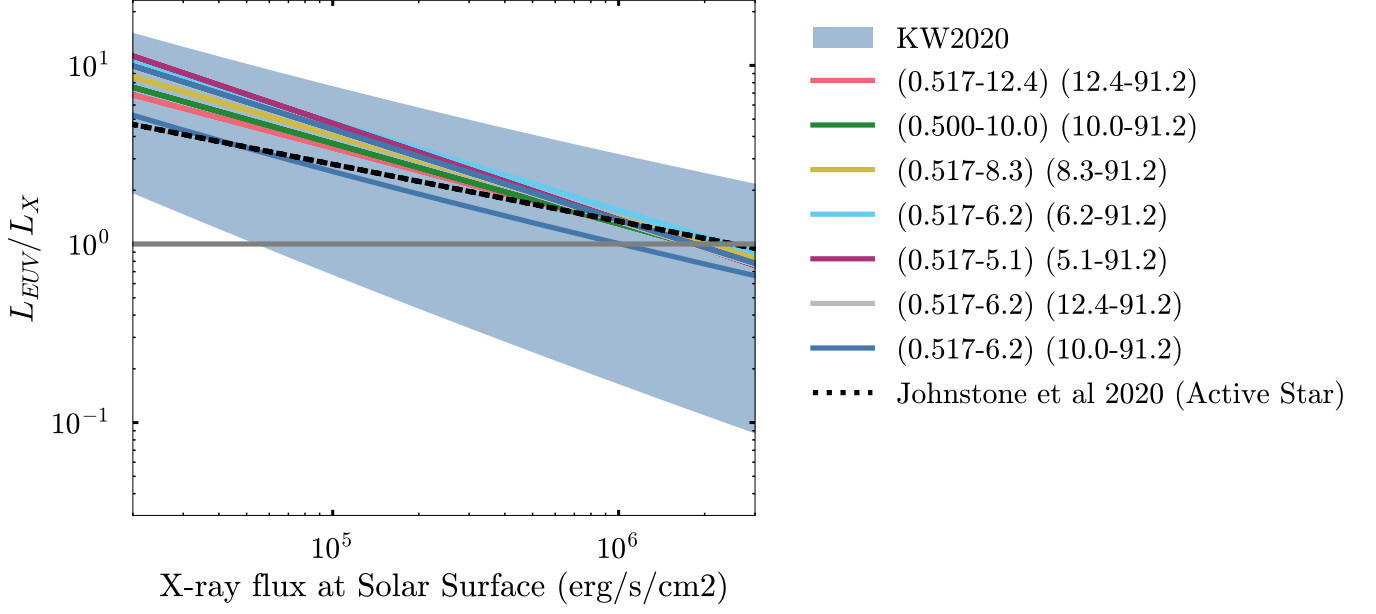
**Table B1:** Summary of model components for different atmospheric compositions. This includes key assumptions regarding species considered, heating and cooling mechanisms, and stellar input parameters.



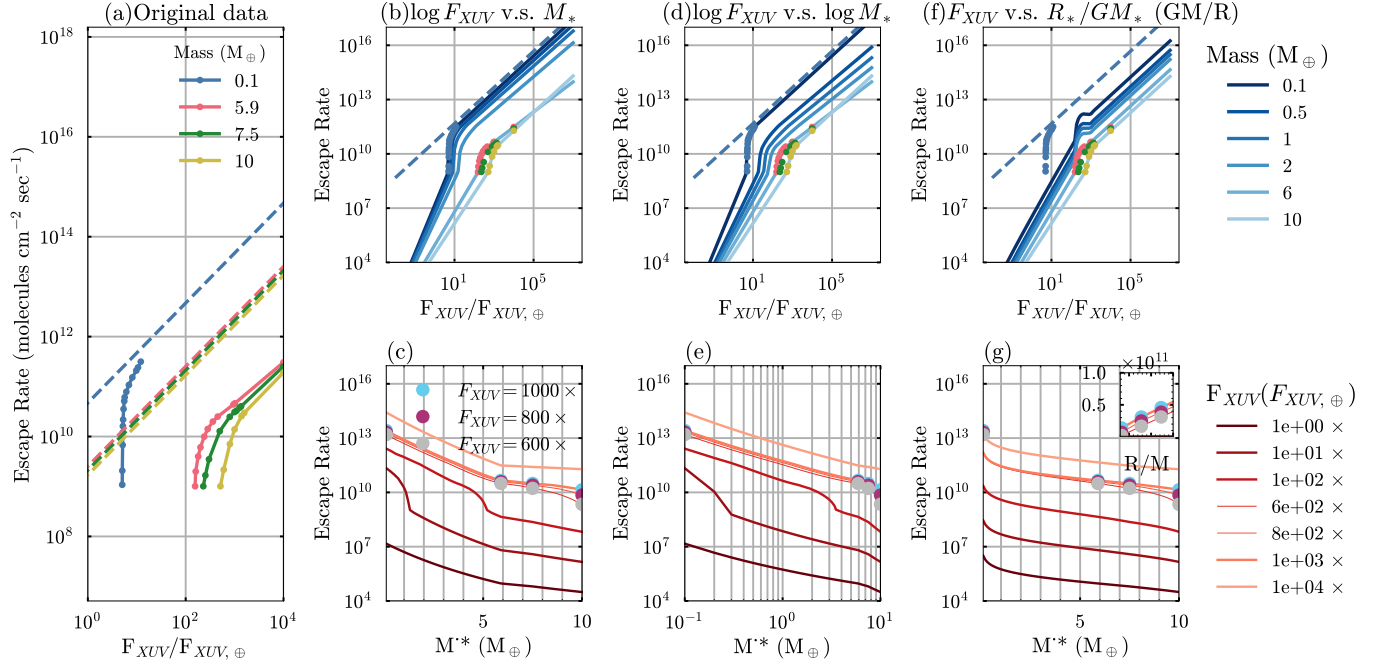
**Figure B1:** Stellar luminosity ( $L_{bol}$ ) normalized to the Sun's luminosity at the present-day ( $L_\odot$ ), and stellar radius ( $R_*$ ) normalized to the Sun's radius ( $R_\odot$ ) versus time from the model of [I. Baraffe et al. \(2015\)](#) for star masses ranging from  $0.1 - 1.0 M_\odot$ .



**Figure B2:** Upper panels: The ratio of X-ray luminosity to bolometric luminosity evolves over time for stellar masses from  $0.1 M_\odot$  to  $1 M_\odot$ . The left panel presents the parameterization from (F. Selsis et al. 2007), while the right panel shows the results obtained by combining data from (A. P. Jackson et al. 2012) and (E. F. Guinan et al. 2016). Lower panels: The X-ray luminosity scaled to solar X-ray flux evolves over time. In the lower right panel, the lines for  $M_* < 0.5 M_\odot$  overlap because E. F. Guinan et al. (2016) presents a unified X-ray evolution for M0–M5 stars.  $L_{x,\odot}/L_{bol,\odot} = 10^{-6.1}$ .



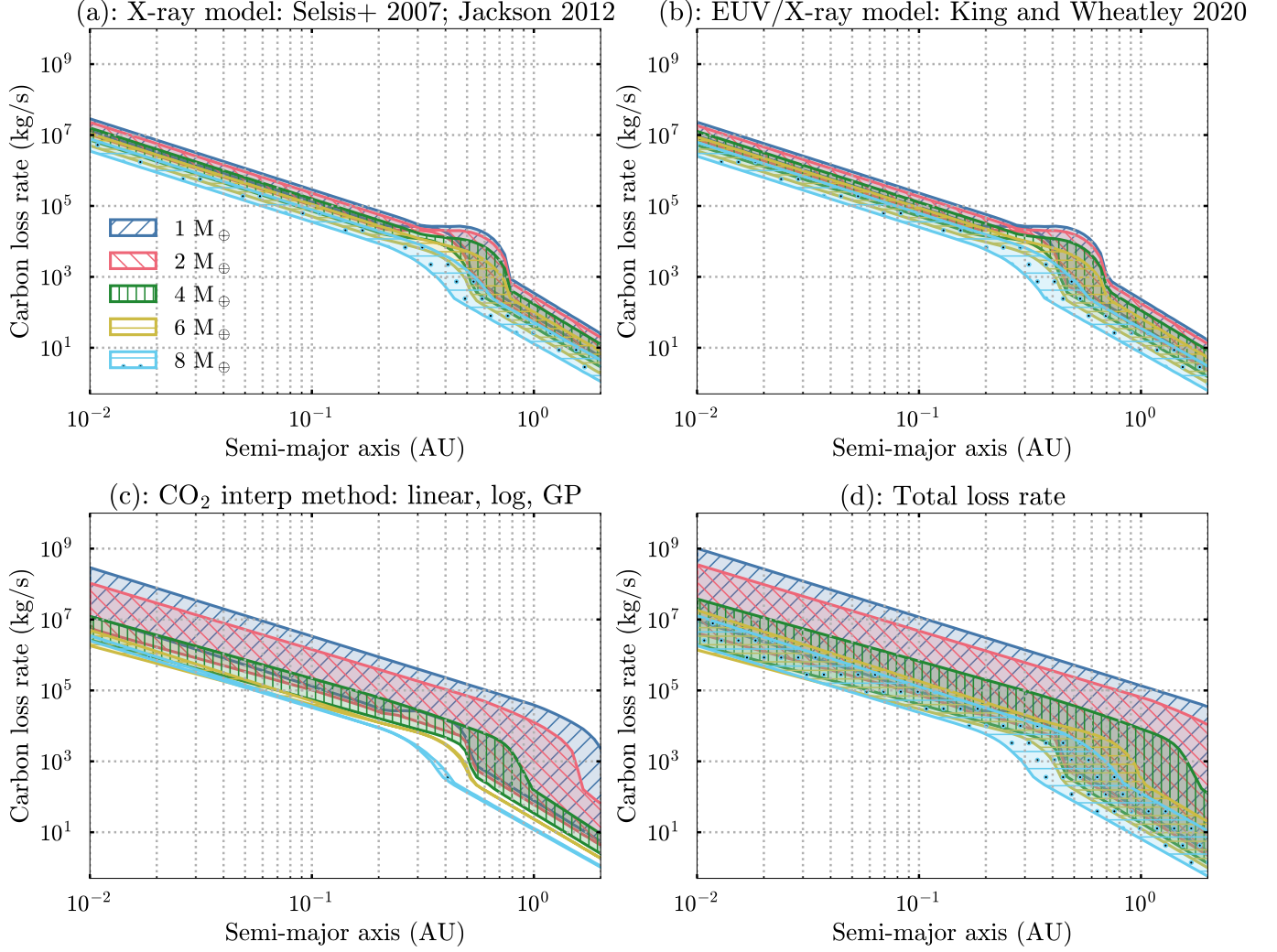
**Figure B3:** The ratio of EUV luminosity to X-ray luminosity is shown as a function of X-ray flux at Stellar surface. The X-ray flux is calculated for a 1 solar-mass star evolving from 1 Myr to 1 Gyr. The blue line and shaded region represent the results from [G. W. King & P. J. Wheatley \(2020\)](#) including uncertainties. Additional colorful lines, labeled with wavelength ranges in Å, are obtained from Table 4 of [G. W. King et al. \(2018\)](#), where the left bracket indicates the X-ray range and the right bracket indicates the EUV range. The dotted black line is derived from [C. P. Johnstone et al. \(2021\)](#).



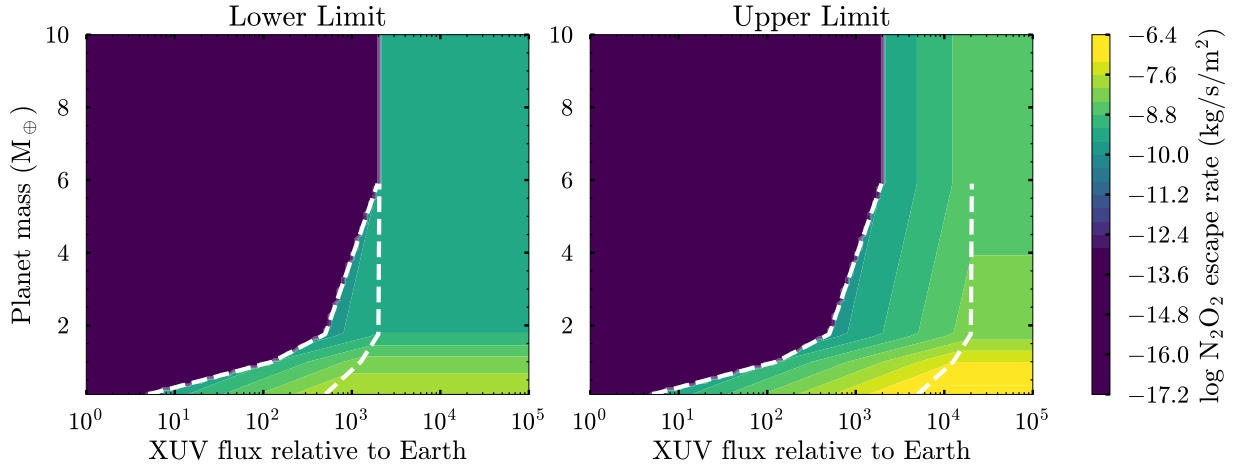
**Figure B4:** CO<sub>2</sub> escape rates are sensitive to interpolation approaches. Leftmost panel: Atmospheric escape rate as a function of XUV flux, scaled to Earth's present-day value. The dots and connected lines represent output from [F. Tian \(2009\)](#) and [F. Tian et al. \(2009\)](#). The rightmost points for super-Earths are extrapolated by [F. Tian \(2009\)](#). The dashed line shows the energy-limited escape rate assuming an efficiency of 0.1. We interpolate their model output and our results for near-Earth-sized planets are sensitive to the interpolate approach used. (b-g) show this sensitivity. In (b)&(c), we interpolate  $\log F_{\text{XUV}}$  with planetary mass  $M_p$ . (d)&(e) interpolates  $\log F_{\text{XUV}}$  with the logarithm of planetary mass ( $\log M_p$ ). (f)&(g) excludes Mars data and assumes the escape rate scales with gravitational potential energy ( $GM_p/R_p$ ), interpolating between  $F_{\text{XUV}}$  and  $R_p/(GM_p)$ . The upper panels illustrate how the escape rate varies with XUV flux for different planetary masses, while the lower panels show how the escape rate changes with planetary mass for various XUV flux levels. The dots represent benchmark output obtained from the leftmost panel, which are used for interpolation. Overall, the linear-planetary-mass provides higher escape rate estimates for near-Earth-sized planets compared to the other methods.



Carbon loss rates for planets with CO<sub>2</sub>-dominated atmospheres orbiting a Solar-like star at  $t = 100$  Myr



**Figure B5:** Carbon loss rate as a function of semi-major axis for planets with CO<sub>2</sub>-dominated atmospheres orbiting a Solar-like star at  $t = 1$  Myr. The shaded region represents the range between the maximum and minimum values under certain assumptions. The uncertainties are broken down as follows: (a): Using the center values of  $\gamma$  for EUV extrapolation and a interpolation of CO<sub>2</sub> escape rates to  $M_p$  (linear), the uncertainty comes solely from the choice of X-ray model. (b): Adopting the J12+G16 X-ray model and linear escape rate interpolation, the uncertainty arises only from the EUV extrapolation. (c): Using the J12+G16 X-ray model and center EUV extrapolation values, the uncertainty stems only from escape rate interpolation. (d): Incorporating all uncertainties. The uncertainties from the X-ray model and EUV extrapolation are of the same order of magnitude. The uncertainty from the interpolation method of CO<sub>2</sub> escape rates is more significant for near-Earth-sized planets but negligible for super-Earths. The total uncertainty results in the loss rates for an 8 Earth-radius planet overlapping with those of a 1 Earth-radius planet.

N<sub>2</sub>/O<sub>2</sub> Escape Rate: CR24 Model

**Figure B6:** The loss rate per surface area for an N<sub>2</sub>/O<sub>2</sub> atmosphere is shown as a function of XUV flux and planetary mass, interpolated/extrapolated from [R. D. Chatterjee & R. T. Pierrehumbert \(2024\)](#). The dark purple region indicates where hydrostatic escape occurs, with the escape rate fixed at  $10^{-13}$  kg/s/m<sup>2</sup>. The white dashed lines show bounds to the energy-limited regime.

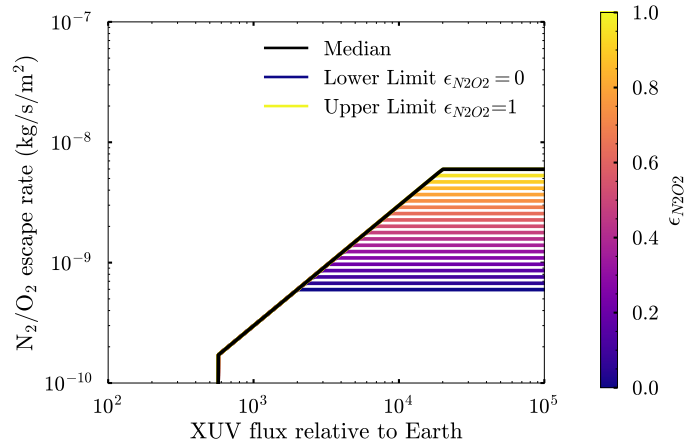


**Figure B7:** The N<sub>2</sub>/O<sub>2</sub> loss rate as a function of XUV flux. In our Monte Carlo simulations, we randomly sample the  $\epsilon_{N_2O_2}$  from a uniform distribution between 0 and 1. The variations in escape rates resulting from this sampling are illustrated by the colorful lines.

Example: Logistic regression to determine Critical  $S/S_0$   
( $\text{CO}_2$  atmos,  $M_p = 1M_\oplus$ ,  $M_* = 0.4M_\odot$ )

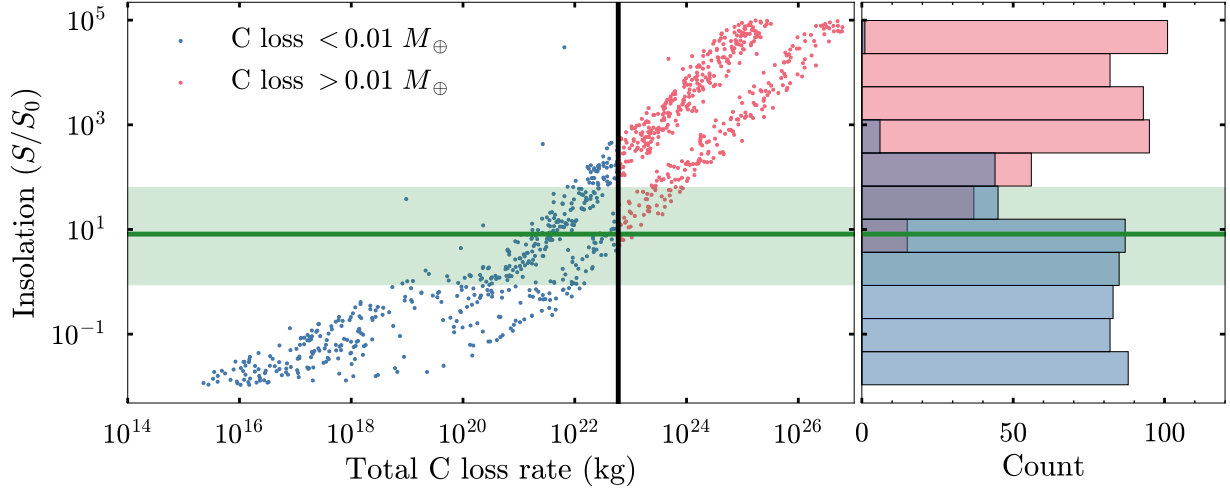


**Figure B8:** Example Monte Carlo simulation results for an Earth-mass planet with a  $\text{CO}_2$  atmosphere orbiting a  $0.4 M_\odot$  star. Left: Bolometric instellation, scaled to earth's value ( $S/S_0$ ), plotted against the total carbon mass lost. Blue dots indicate Monte Carlo outcomes in which the planet retains its atmosphere (with a initial carbon mass of  $0.01 M_\oplus$ ), while orange dots indicate outcomes in which the atmosphere is stripped. The middle green line marks the critical instellation at  $p_0 = 0.9$ , meaning there is a 50% probability of atmospheric retention at that flux level. The shaded region spans from  $p_0 = 0.99$  (lower boundary) to  $p_0 = 0.5$  (upper boundary), illustrating instellation thresholds for 99% and 50% retention probability, respectively. To obtain a robust estimate of the critical instellation  $S^*$  at a given  $p_0$ , we draw 5,000-point bootstrap samples from our 10,000-point Monte Carlo dataset (in 10 iterations), refit the logistic model each time, and then average the resulting  $S^*$  values. Right: Histograms of the instellation values for planets that retain atmosphere (blue) versus those that lose it (orange).

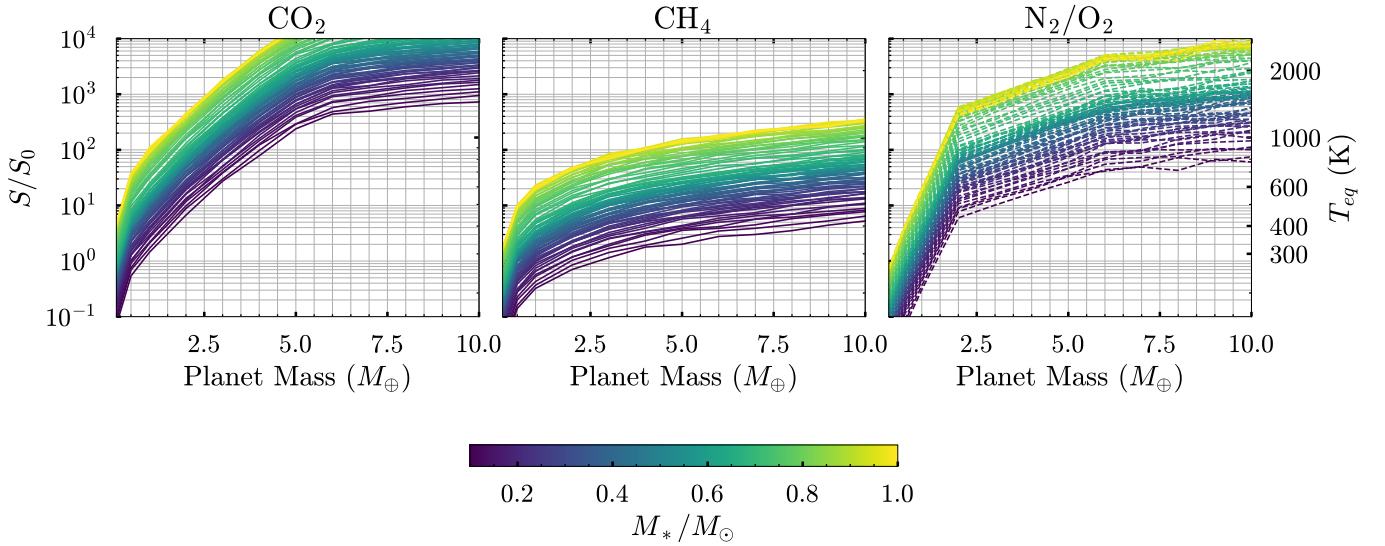


**Figure B9:** Caption

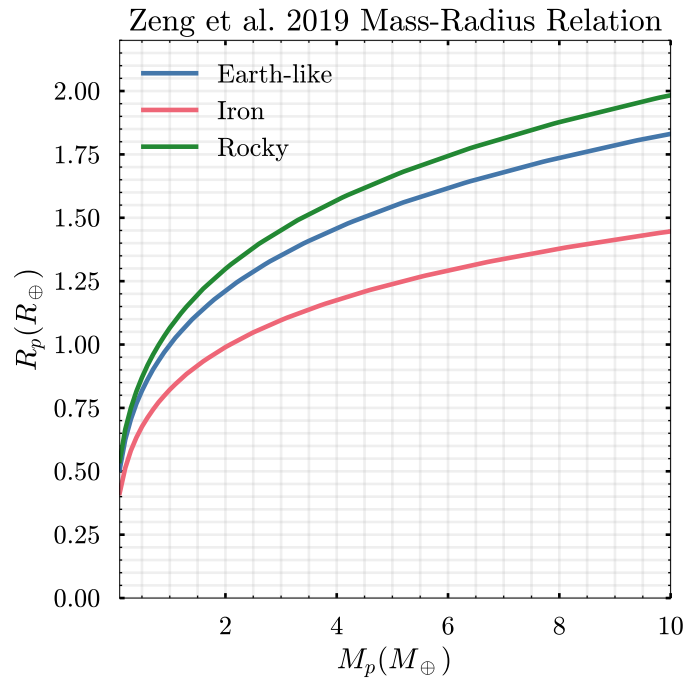


**Figure B10:** The mass-radius relationship for different planetary compositions: pure iron (100% Fe), Earth-like rocky (32.5% Fe + 67.5%  $\text{MgSiO}_3$ ), and pure rock (100%  $\text{MgSiO}_3$ ).

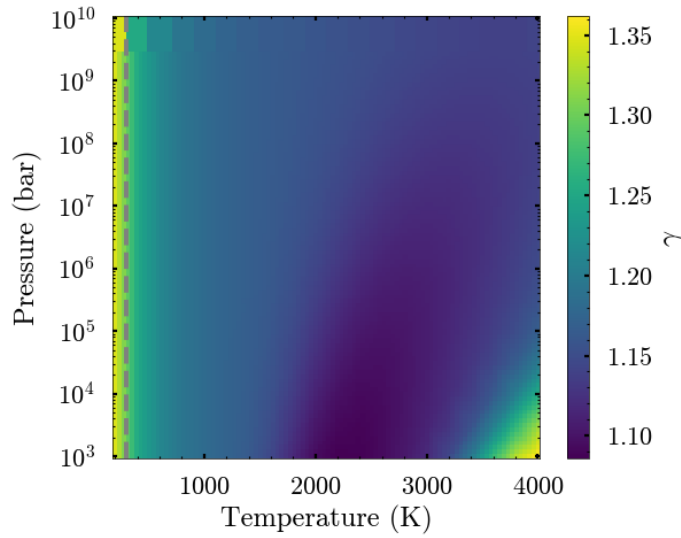


**Figure B11:** The heat capacity ratio ( $\gamma$ ) for  $\text{CO}_2$  as a function of temperature and pressure, obtained using NASA's Chemical Equilibrium with Applications (CEA) code (<https://cearun.grc.nasa.gov/>) (S. Gordon & B. J. McBride 1994), considering ionized species as possible products.

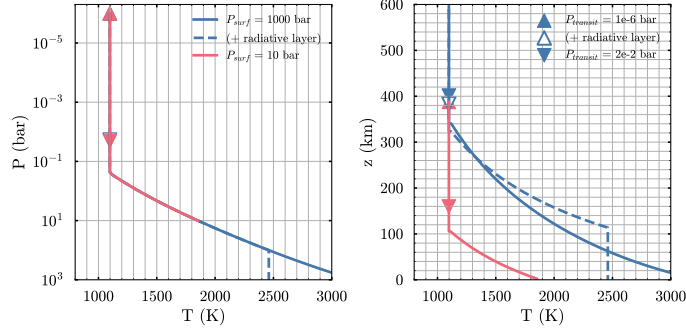


**Figure B12:** Left Panel: Temperature-Pressure profiles for atmospheres with surface pressures of 10 bar (pink) and 100 bar (blue). The solid lines correspond to the two-layer model (Scenario (a) in Fig. 5), where the atmosphere consists of a convective lower layer and an isothermal upper layer beyond the radiative-convective boundary (RCB). The dashed lines represent the three-layer model (Scenario (b) in Fig. 5), where an additional radiative layer forms near the surface. Right Panel: Altitude-temperature profiles for the same cases shown in the left panel. Triangular markers indicate the pressure level probed by the transit method, with filled symbols representing the two-layer model (Scenario (a)) and open symbols representing the three-layer model (Scenario (b)).

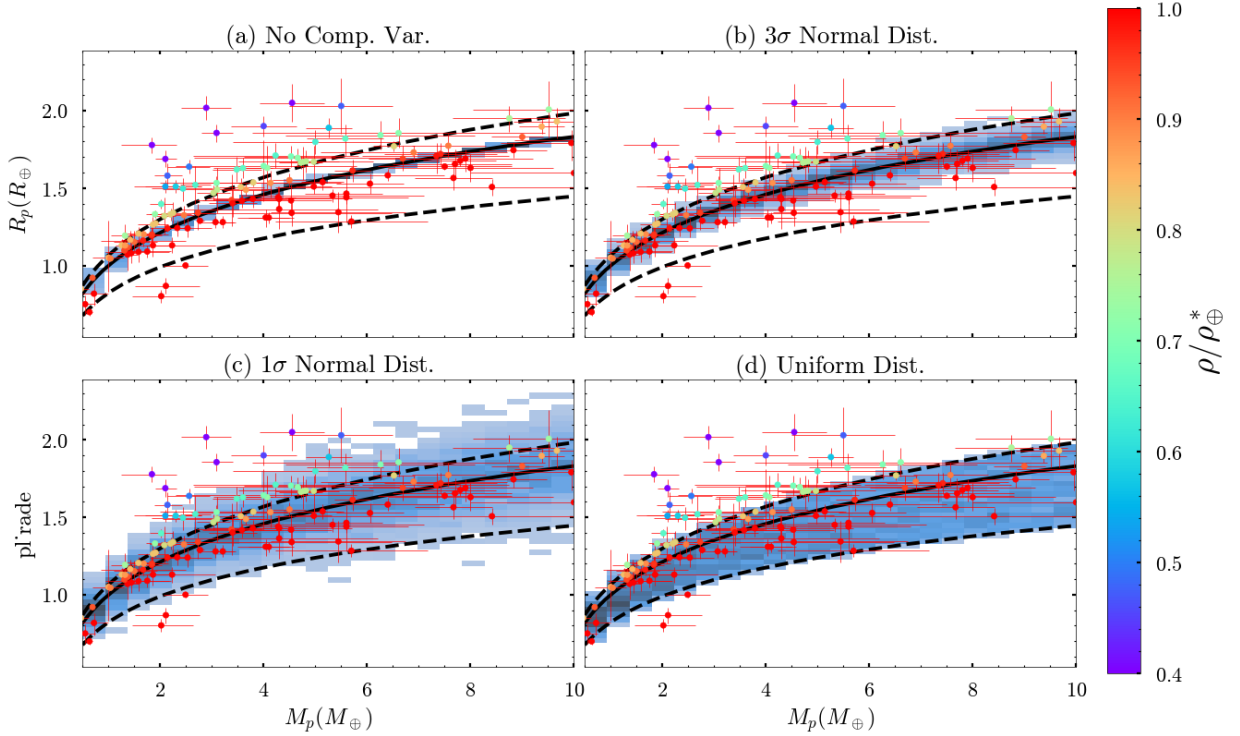


**Figure B13:** Mass-Radius Relationship for Solid-Body Planets Under Three Composition Assumptions: Given a planetary mass ( $M_p$ ), the radius is assigned based on different composition assumptions: (a) a fixed Earth-like composition ( $R_{\text{earth-like}}(M_p)$ ), (b) a normal distribution centered at  $R_{\text{earth-like}}(M_p)$  with a standard deviation equal to one-third of the difference between  $R_{\text{earth-like}}(M_p)$  and  $R_{\text{silicate}}(M_p)$ , (c) a normal distribution centered at  $R_{\text{earth-like}}(M_p)$  with a standard deviation equal the difference between  $R_{\text{earth-like}}(M_p)$  and  $R_{\text{silicate}}(M_p)$ , and (d) a uniform distribution spanning the range between  $R_{\text{silicate}}(M_p)$  (pure  $\text{MgSiO}_3$ ) and  $R_{\text{iron}}(M_p)$  (pure Fe). The shaded blue region represents a 2D histogram of our Monte Carlo samples, with darker colors indicating higher number density. The dots are observed rocky planet candidates from the NASA Exoplanet Archive, with error bars representing measurement uncertainties. The colors represent the measured density relative to Earth's composition.



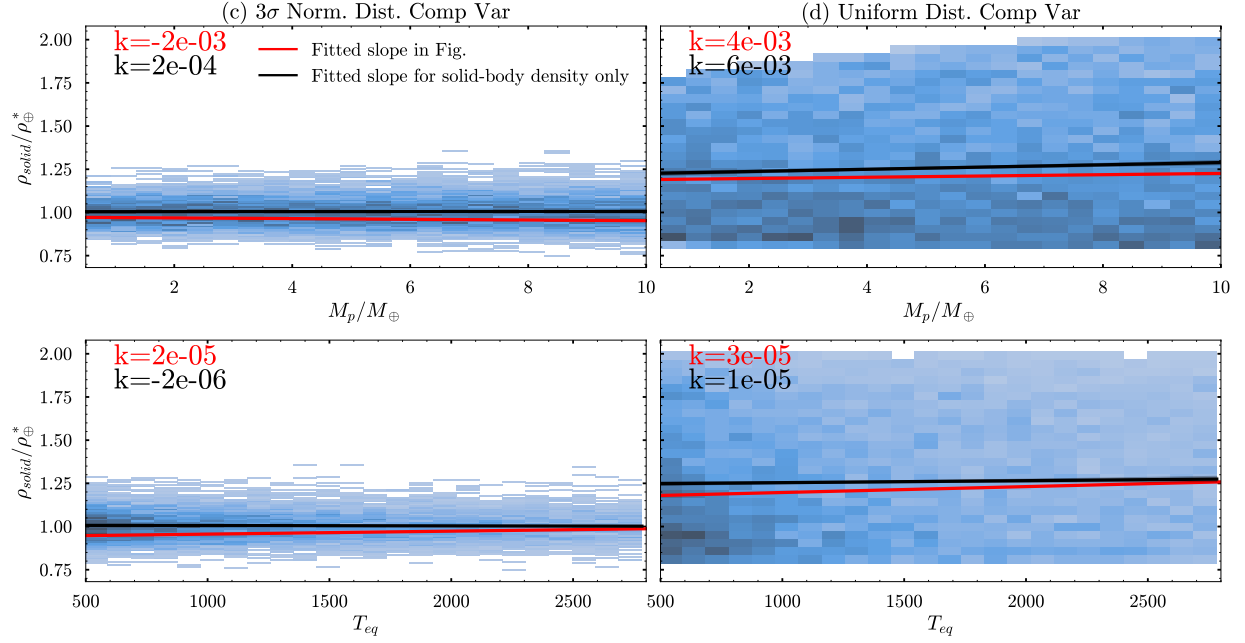


**Figure B14:** Trend of the Scaled Density of the Solid Body Only: The upper row shows 2D histograms of the scaled density of the solid body ( $\rho_{solid}/\rho_{\oplus}^*$ ) as a function of planetary mass ( $M_p$ ), while the lower row shows its relationship with equilibrium temperature ( $T_{eq}$ ). The left column (c) assumes that solid density variations follow a normal distribution, with a standard deviation equal to 1/3 of the difference between  $R_{\text{earth-like}}(M_p)$  and  $R_{\text{silicate}}(M_p)$ . The right column (d) corresponds to a uniform distribution spanning the range between  $R_{\text{silicate}}(M_p)$  (pure  $\text{MgSiO}_3$ ) and  $R_{\text{iron}}(M_p)$  (pure Fe). The black lines and black text indicate the results of linear regression for the solid-body scaled density, while the red ones represent the linear regression of the total density derived from the transit radius (see Fig. 7). In (c), the slope of the solid-body density trend is an order of magnitude lower than that of the final total density, suggesting an insignificant contribution from variations in the solid composition. However, in (d), the solid-body density trend significantly influences the overall density slope, even changes the sign for slope of  $\rho_{solid}/\rho_{\oplus}^* - M_p$ . We also tested uniformly sampling density instead of radius, but the trend caused by the solid portion alone persists.